To the Graduate School:

The members of the Committee approve the thesis of Bujidmaa Borkhuu presented on September 11, 2009.

Jefferson Snider, Committee Chair

Stephen Williams, Graduate Faculty Representative

Robert Kelly

Bart Geerts

APPROVED:

Alfred R. Rodi, Head, Department of Atmospheric Science

Ron Ettema, Dean, College of Engineering and Applied Sciences

Abstract

Borkhuu, Bujidmaa, Snowfall at a High-elevation Site: Comparisons of Six Measurement Techniques, MS, Department of Atmospheric Science, December 2009.

This work presents an analysis of data from six wintertime precipitation (snow) sensors operated at the windy and forested Glacier Lakes Ecosystem Experiments Site located in the Medicine Bow Mountains of southeastern Wyoming. There are two findings. First, a comparison of precipitation measurements from the tower-based Hotplate (a new type of precipitation sensor, operated on top of a 30 m tower) and the surface-based Vaisala precipitation sensor (VRG) showed that during cold-season conditions the VRG measurement is positively biased relative to the Hotplate. Second, one of the surface-based National Atmospheric Deposition Program (NADP) sensors, an Alter-shielded Belfort precipitation gauge, is also positively biased. In this comparison the NADP sensor reports an average precipitation rate which is a factor 1.6 larger than the Brooklyn Lake Snow Telemetry gauge. Both of these findings are attributed to the enhanced registration of wind-redistributed ice particles (blowing snow aliasing as snowfall) by the overestimating gauge.

SNOWFALL AT A HIGH-ELEVATION SITE: COMPARISONS OF SIX MEASUREMENT TECHNIQUES

by

Bujidmaa Borkhuu

A thesis submitted to the Department of Atmospheric Science and the University of Wyoming in partial fulfillment of the requirements for the degree of

MASTER OF SCIENCE

in

ATMOSPHERIC SCIENCE

Laramie, Wyoming

December, 2009

ACKNOWLEDGEMENTS

I thank Dr. Jefferson Snider for accepting me as his student for allowing me to work in such an interesting area. This work supported financially by Wyoming Water Development Committee. The U.S. Forest Service's GLEES site, NRCS SNOTEL site, and NCAR Vaisala Rain Gauge sensor, both in the Medicine Bow Mountains contributed valuable data.

I must recognize my committee for given precious time to evaluate and guide this thesis, Jefferson Snider, Robert Kelly, Stephen Williams and Bart Geerts. Thanks also to Matthew Burkhart and John Frank who provided assistance and were willing to provide suggestions. Also, I thank my mentors and friends at ESRL, NOAA, Dr. Russ Schnell and Carol Knight. I am blessed to have such strong and warm-hearted friends beside me. Many thanks to my fellow graduate students and friends at UW, especially Department of Atmospheric Science.

Finally, I thank to my parents, Borkhuu Damdintseren and Nina Dolgor, my family and my daughter, Khulan, for their emotional support, encouragement and love.

Table of Contents

List of Figures

List of Tables

Chapter I: Introduction

1.1 Introduction

It is widely recognized that precipitation measurements can be biased by wind-induced errors. Measurement of snow precipitation is especially confounded by wind, particularly at a forested measurement site. Negative bias occurs if the precipitation gauge is shadowed by trees, and positive bias occurs if wind-resuspended ice particles are transported to the precipitation sensor subsequent to their fallout from the atmosphere (Goodison, 1978; Hedstrom and Pomeroy, 1998; Yang et al., 2000). In addition, a negative wind-induced bias occurs because the downward vertical speed of a snow particle is decreased by the airflow distortion that occurs in the vicinity of a precipitation gauge (Groisman et al., 1996; Sugiura et al., 2006). Because the fall speed of a compact ice-phase particle (e.g., graupel), and a rain drop, is larger than that of a snow particle the flow distortion bias is largest for the snow particle. Fall speeds for these three particle types are about 0.5 m/s (snow), 2 m/s (graupel) and 10 m/s (drop) assuming a 4 milligram particle mass (water-equivalent particle diameter = 2 mm). By employing a novel experimental strategy, and through an intercomparison of data from six precipitation sensors operated at a windy and forested site, this work strives to improve confidence in high-elevation wintertime precipitation measurements.

1.2 Precipitation measurements

Data from six precipitation sensors operated at a field site located in the Medicine Bow Mountains of southeastern Wyoming are analyzed. The six devices are: 1) the Alter-shielded Belfort gauge located at the Brooklyn Lake National Atmospheric Deposition Program (NADP) site, 2) the unshielded sample volume sensor at the NADP site; 3) the unshielded Vaisala Rain Gauge (VRG) operated by the National Center for Atmospheric Research (NCAR) and located ~200 m northeast of the Brooklyn Lake NADP site; 4) the shielded gauge (Serreze et al., 1999) located at the Brooklyn Lake Snow Telemetry (SNOTEL) site, 1 km southeast of the NADP site, 5) the snow pillow located at the Brooklyn Lake SNOTEL site, and 6) the Yankee Ecosystem Systems model TPS-3100 Sensor, hereafter referred to as the "Hotplate."

Complete descriptions of these sensors are provided in Chapter II (Hotplate) and Chapter III (NADP-gauge, VRG-sample volume, VRG, SNOTEL-gauge and SNOTEL-pillow). Also, a more complete description of the measurement sites is provided in Chapter III. Data acquired during the winter and spring seasons of 2007 and 2008 are analyzed.

Two fundamental characteristics of the sensors are presented in Table 1.1. The quantity "time resolution" represents the time interval between precipitation data values. Wolfe (2007) shows that the effective time resolution of the Hotplate is 135 s and this is the value presented in third column of the table. Time resolutions vary

between 1 s (Hotplate) to 604800 s (NADP). The fourth column contains the smallest increment of accumulation which can be resolved.

With the exception of the Hotplate, each of these instruments is a precipitation accumulation system. For this reason the sensor intercomparisons are made in terms of snow water equivalent (SWE) accumulations. The accumulation (A) derived from the Hotplate's measurements of precipitation rate (P) are evaluated as

$$A(t) = \int_0^t P(t') \cdot dt' \approx \sum_0^t P \cdot \Delta t \qquad (1)$$

Here P is the Hotplate's precipitation rate measurement and Δt is the time interval between two measurements (1 s).

Table 1.1 Basic characteristics of the snow sensors used in this study

Sensor	Time Resolution, s	Response Time, s	Accumulation Resolution, mm
Hotplate	1	135	0.1
VRG	60 [a]	NA	0.1
SNOTEL-pillow	3600	NA	2.5
SNOTEL-gauge	3600	NA	2.5
NADP-gauge	604800	NA	0.13
NADP-sample-volume	604800	NA	0.13

[a] in 2007 the VRG time resolution was 300 s

NA ≡ not applicable

1.3 Overview

One of the data sources analyzed in this thesis is the precipitation measurements made at the National Atmospheric Deposition Program (NADP) sites. This program was initiated in 1984 to monitor precipitation composition and thus, indirectly, the ecosystem impact of primary pollutant emissions (e.g., sulfur dioxide). At an NADP site precipitation samples are collected weekly and transported to a laboratory where the aqueous concentration of several components is analyzed (acidity (H^+), sulfate (SO_4^{2-}), nitrate (NO_3^-), ammonium (NH_4^+), etc.). The week-integrated precipitation amounts and the concentrations are archived on the NADP web site (http://nadp.sws.uiuc.edu/sites/ntnmap.asp; 12 May 2009). The product of weekly precipitation amount and the analyte concentration is both dimensionally and conceptually the atmosphere-to-land flux of the specified component. This product is commonly referred to as "wet deposition". The basis for the following discussion is the weekly measurements of precipitation amount made at the Brooklyn Lake NADP site – one of the several monitoring systems at the Glacier Lakes Ecosystem Experiments Site (GLEES) in the Medicine Bow Mountains of southeastern Wyoming (Musselman et al., 1994, http://www.fs.fed.us/rm/pubs_rm/rm_gtr249.html; 12 May 2009).

The Brooklyn Lake NADP site is windy for several reasons: 1) its high elevation, 2) its location in the lee of the high ridge of the Snowy Range (elevation ~3400 m), and 3) its geographic setting ~20 km to the south of the Wyoming wind

corridor (Martner and Marwitz, 1982). Because of the wind intensity at the GLEES, and because of the location of the Glacier Lake NADP in an area affected by snow drifts, it is suspected that the precipitation measurement at the NADP site is affected by blowing snow. It is also suspected that the character and degree of this influence is different from that documented by Williams et al. (1998) at their treeless NADP site located in north central Colorado at an elevation of 3520 m. The post-depositional transport of snow discussed in the previous paragraph has been studied in a Canadian boreal forest. At this site the wind speed is not as great as in the subalpine forests of the Rocky Mountains of Wyoming and Colorado. An example of the Canadian research is the study of MacKay and Bartlett (2006) who investigated the post-depositional unloading of snow from conifer trees. They commented that wind gustiness may be a factor determining the fate of snow deposited on conifer branches (a process referred to as "unloading"), but they were unable to quantify that wind-induced unloading. Schmidt and Pomeroy (1990) noted that the elasticity of conifer branches, which is temperature dependent, can also be an important factor for the unloading process. The complexity of the interactions among snow, trees and wind has been recognized for over forty years (Hoover and Leaf, 1967).

1.4 Objectives

This work addresses four questions related to the overarching theme of snow precipitation measurement at a forested, and windy, field site:

1) What does the comparison of NADP-gauge and NADP-sample-volume measurements tell us about the reliability of wet deposition data from NADP/GLEES and from other NADP sites in Wyoming, Colorado, and Utah? This line of investigation has relevance to the central theme of the thesis, and also to the use of NADP deposition data in the formulation of ecosystem impact assessments.

2) At NADP/GLEES, and at the other Rocky Mountain sites, do NADP-gauge and NADP-sample-volume precipitation measurements vary between cold-season and warm-season conditions?

3) How do the two NADP/GLEES precipitation sensors compare to the other four sensors located at GLEES?

4) A central focus of this work is measurements made with the Hotplate sensor. This sensor was operated 30 m above the most adjacent surface-based sensor (the VRG), and also ~15 m above the top of the forest canopy. The Hotplate data set is unique, because the instrument is new - few comparative studies are reported (Hallett and Rasmussen, 2006; Landolt et al., 2008; Rasmussen et al., 1999; Rasmussen et al., 2005; Tryhane et al, 2005; and Wolfe, 2007) - and because of its placement relative to the other five sensors provides insight into the process of wind-induced redistribution of ice particles at a windy and forested measurement site.

1.5 Summary

This thesis conducts comparisons among several assessments of snow precipitation at the GLEES. Also analyzed is the 20-year record of precipitation monitoring conducted at NADP sites in the Rocky Mountains of Wyoming, Colorado and Utah. Four of the GLEES-based sensors are operated under the auspices of two nationally-funded monitoring networks: 1) the National Atmospheric Deposition Program (NADP), and 2) the National Resource Conservation Service Snow Telemetry Network (SNOTEL). Further, one of the sensors (VRG) is in use for assessing the efficacy of wintertime snow enhancement as part of the State of Wyoming Weather Modification Project. The final sensor (Hotplate) was calibrated and operated by the author of this thesis, with technical assistance from the staff of the Department of Atmospheric Science at the University of Wyoming.

The chapters of the thesis are arranged in the following manner. First, the Hotplate data analysis algorithm is described (Chapter II). Second, descriptions of the field measurement sites are introduced and the unintentional sampling of wind-redistributed ice is examined using the 20-year NADP data set (Chapter III). Furthermore, comparisons are made among the NADP/GLEES, VRG and the SNOTEL sensors (Chapter IV). This analysis exploits data collected in 2007, when the Hotplate data is limited. Third, comparisons of the six precipitation measurements are made using the 2008 field measurements including both cold-season and warm-season Hotplate data (Chapter IV). This comparison examines the

conjecture that the five surface-based sensors inadvertently register wind-resuspended ice particles as a snowfall. Chapter V summarizes and concludes the investigation.

Chapter II: Hotplate Calibration

2.1 Introduction

In this chapter a new type of precipitation gauge is introduced and its operation is described. The instrument is manufactured by Yankee Ecosystem Systems (YES) and is hereafter referred to as the "Hotplate".

The bulk of this chapter describes an algorithm developed for analyzing Hotplate data, including methods used to calibrate the Hotplate's response to wind and precipitation. The precipitation calibration, previously described by Wolfe (2007), is extended here to include consideration of the Hotplate's response to two different drop sizes. These calibrations are based on measurements made in a Laboratory at the University of Wyoming (Laboratory), at the Glacier Lakes Ecosystem Experiments Site (GLEES) and at the University of Wyoming Balloon Launch Facility (Hangar). Also, precipitation rates derived from the algorithm are contrasted with those produced by the proprietary YES Hotplate Algorithm.

Hereafter, the terminology "Wyoming Hotplate Algorithm" will refer to the precipitation rate derived via the algorithm and calibrations described in this chapter.

2.2 The Hotplate

The Hotplate is shown in Figure 2.1. It consists of two horizontally stacked 13 cm (diameter) circular plates mounted on a pedestal. One plate faces upwards, exposed to precipitation, and the other faces downwards. Resistive heating elements

maintain the top and bottom plates at ~75 ^{o}C (Rasmussen et al., 2005). Electrical power added to the Hotplate via the resistive heaters compensates for power dissipated via diffusive, convective (free and forced) and radiative heat transfer (top and bottom plates) and via water substance phase change (top plate only).

2.2.a Hotplate Data Files

The YES Hotplate Algorithm derives the precipitation rate from measurements of the electrical power supplied to the top and bottom plate heaters. These two power values are referred to as the "sensor plate power" and "reference plate power", respectively.

Two data files are generated by the Hotplate; one of these is proprietary (the "*f*1 file") and the other is accessible by standard users (the "*hp* file"). Via a legal agreement with the National Center for Atmospheric Research, our group obtained access to the proprietary *f*1 files. The contents of these files are presented in Table 2.1. Throughout this work, the time will be formatted as the Universal Coordinated Time (UTC) which is seven hours later than local time (Rocky Mountain Standard Time).

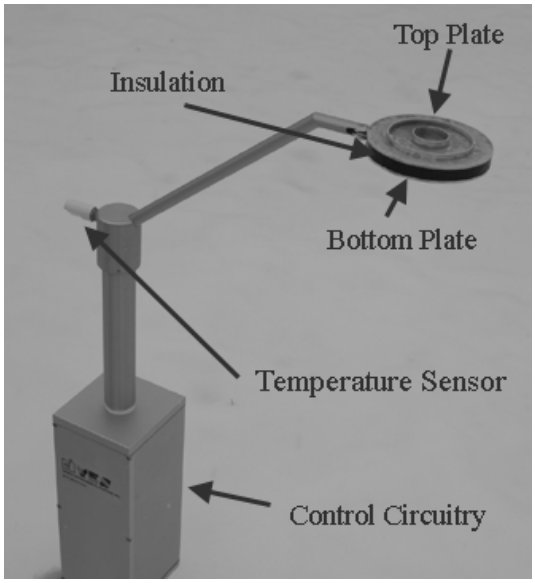

Figure 2.1 - The Hotplate consists of two stacked 13 cm (diameter) circular plates mounted on a pedestal. The control circuitry box controls the plate temperatures, applies the YES Hotplate Algorithm and outputs the two files discussed in the text.

Table 2.1 Hotplate data files

Variable	*f*1 file	*hp* file
Unix Time[1], s	X	X
Sensor Plate Power, W	X	
Reference Plate Power, W	X	
Delta Power, W	X	
Ambient Temperature, ^{o}C	X	X
Wind Speed, m/s	X	X
Catch Efficiency, %	X	
Power Offset, W	X	
Precipitation Rate, mm/hr	X	X

[1] Unix time is a system for describing points in time, defined as the number of seconds elapsed since midnight Coordinated Universal Time (UTC) of January 1, 1970, not counting leap seconds.

The precipitation rate reported in the $f1$ and hp files are symbolized as $pf1$ and php, respectively. For the following discussion a 300-second running average of the $pf1$, evaluated at the final second of the averaging interval, is symbolized as $pf1\_ave$. Also, the $pf1\_ave$ time series is used to generate a conditional precipitation rate symbolized as $cpf1$; this value will be compared to the archived value of $pf1$. The objective is to develop an understanding of the data processing that goes into the calculation of $pf1$ and its relationship to php. Three logical conditions, define the $cpf1$: 1) If the current value $pf1\_ave > 0.25$ mm/hr, and if the previous value of $cpf1$ is zero, then $cpf1 = pf1$; 2) If the previous value of $cpf1$ is greater than zero and if the current value of $pf1$ is also greater than zero, then $cpf1 = pf1$; 3) If the previous value of $cpf1$ is greater than zero and if the current value of $pf1$ is equal to or less than zero, then $cpf1 = 0$.

Two examples of time series data archived in the $f1$ and hp files are shown in Figures 2.2 and 2.3. In the top two panels are $pf1$ and $pf1\_ave$, and in the bottom two panels are php and $cpf1$. There is a good match between the latter two time series. The Figures 2.2 and 2.3 are not intended to demonstrate a complete understanding of the algorithm used to derive the php time series, only to indicate that a quantity approximating php can be derived from $pf1$ by applying the conditions discussed in the previous paragraph. This work will focus on the $pf1$

data, for the most part ignoring the *php* data, and will also contrast the *pf*1 with that derived via the Wyoming Hotplate Algorithm (Section 2.1).

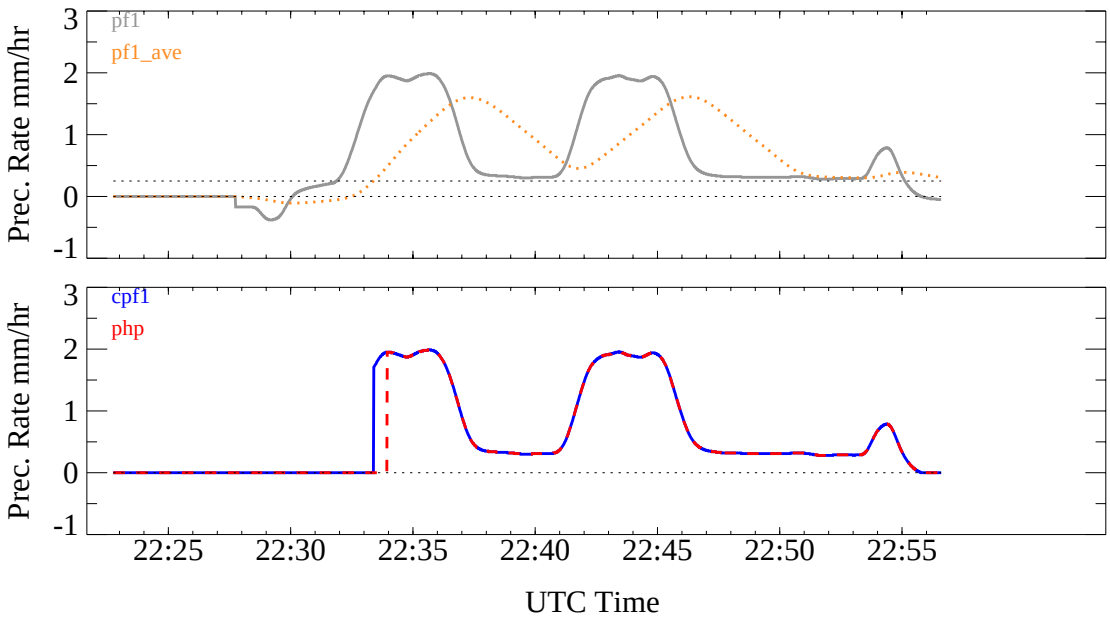

Figure 2.2 - Precipitation rates for two intervals with water dripped on the Hotplate during ventilation. The measurement was conducted in the Laboratory on 20070515. The *pf*1 and *pf*1_*ave* are plotted in the top panel and the bottom panel shows *php* plotted with *cpf*1.

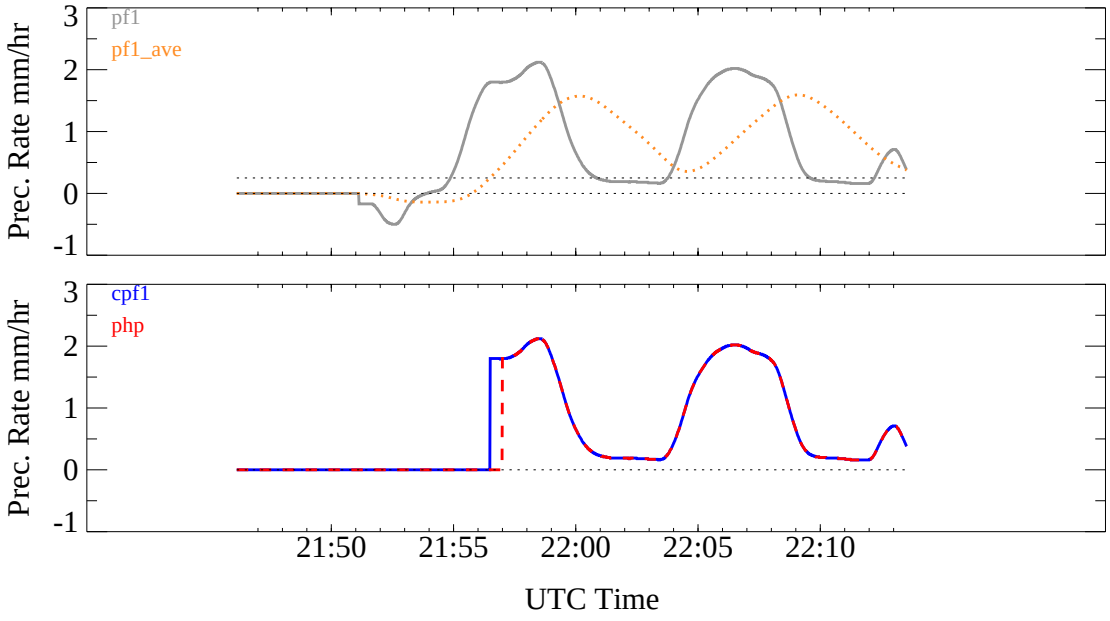

Figure 2.3 – As in Figure 2.2, but for the 20080124.

2.2.b Comparison of the *f*1 and *w*l Precipitation Rates

The *f*1 precipitation rate (*pf*1), and that derived via the Wyoming Hotplate Algorithm, symbolized " *pw*l ", are shown in Figures 2.4 and 2.5. In these two figures the *pf*1 values from Figures 2.2 and 2.3 are presented with the *pw*l and a reference precipitation rate (described in next section). It is evident that the *pf*1 calculation underestimates the reference, while the *pw*l calculation does a good job of replicating it, and that the *pf*1 overestimates the precipitation rate during a time interval when the precipitation reference was not being applied (between 22:37:40 and 22:40:40 in Figure 2.4, and between 22:00:40 and 22:03:40 in Figure 2.5). The next section discusses the Wyoming Hotplate Algorithm, and the Laboratory calibration data which is integral to that calculation.

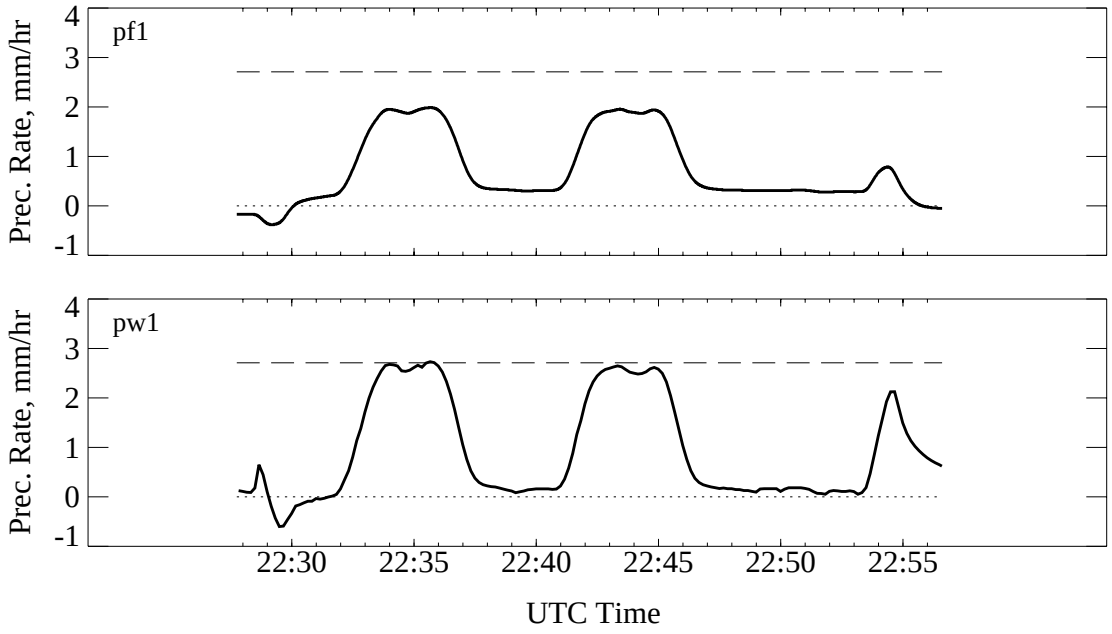

Figure 2.4 - Time series of $f1$ precipitation rate (top panel) and that defined by the Wyoming Hotplate Algorithm (bottom panel) for 20070515. The reference precipitation and zero precipitation rates are shown by dashed and dotted line, respectively.

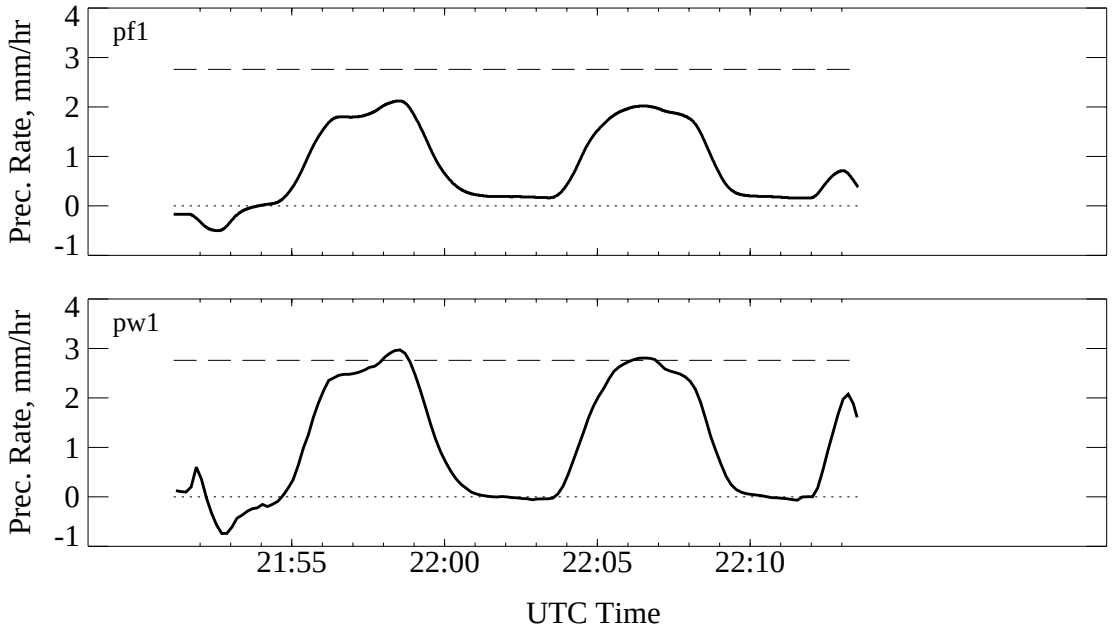

Figure 2.5 – As in Figure 2.4, but for the 20080124.

2.3 Laboratory and Hangar Setup

The reference precipitation rate shown as a horizontal dashed line in Figures 2.4 and 2.5, is produced by a constant volumetric liquid water pump (Ismatec Inc. Model 7618; Wolfe, 2007). The pump uses metal rollers to draw water through a plastic tube from a reservoir and produces drops of uniform size at a frequency which depends on the pump setting. The pump's volumetric output rate (symbolized as p_ref) was evaluated by timing the delivery of water into a graduated cylinder. The instrument setup is shown in Figure 2.6.

The average value, and standard deviation, of the water pump rates for three pump settings in both the Laboratory and in the Hangar are reported in Table 2.2. The water flow rate ($\dot{V}$, third column of Table 2.2), and the surface area of the Hotplate ($A = 0.0133$ m^2), are related to the reference precipitation rate as

$$p\_ref = K \cdot \frac{\dot{V}}{A} \qquad (2)$$

where K is a unit conversion factor.

The Laboratory and Hangar calibrations consisted of five intervals: 1) A Hotplate warm-up period (15 min), 2) water application to the Hotplate for 4 min, 3) a 5 min interval with no water application, 4) water application to the Hotplate for 4 min, and 5) no water application for at least 2 min before the stopping the data acquisition. Time intervals corresponding to either the absence, or occurrence of water delivery to the Hotplate, are defined as the inactivity and activity intervals, T_I

and T_A, respectively (Wolfe, 2007). During the activity interval, drops were distributed over the surface of the top plate. The inactivity (T_I) and activity (T_A) time intervals are illustrated in Figure 2.7.

During some of the experiments (Laboratory and Hangar) the Hotplate was ventilated with a blower. Typically, the air velocity was either 0 m/s (blower off), or 7.5 m/s (blower-to-Hotplate distance 0.76 m).

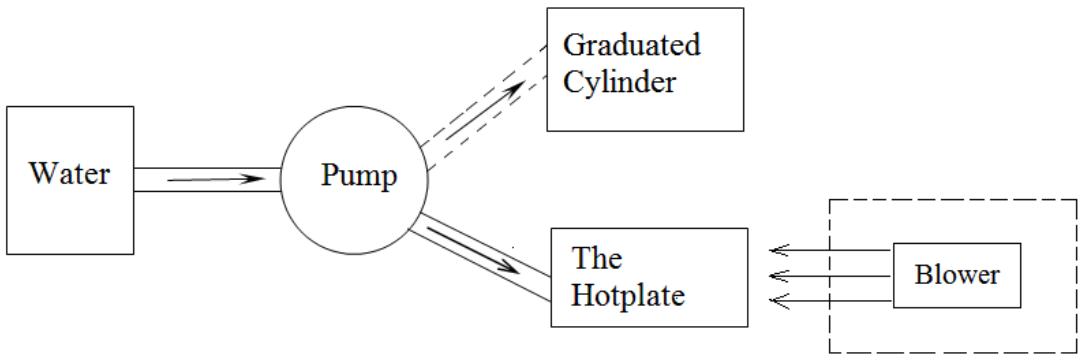

Figure 2.6 - Instrument setup used in the Laboratory and Hangar.

Table 2.2 Pump flow rates and reference precipitation rates

Number of measurement, N	Pump Setting	Water Flow Rate, cm^3/min	Standard Deviation of Water Flow Rate, cm^3/min	Reference Precipitation Rate, p_ref mm/hr
0.7 mm ID delivery tube (Laboratory)				
8	20	0.24	0.01	1.09
33	50	0.59	0.01	2.75
9	80	0.98	0.01	4.41
0.4 mm ID delivery tube (Laboratory)				
2	20	0.22	-	0.98
2	50	0.52	-	2.34
2	80	0.83	-	3.76
0.7 mm ID delivery tube (Hangar)				
2	20	0.17	-	1.07
3	50	0.59	-	2.64
1	80	0.83	-	3.74

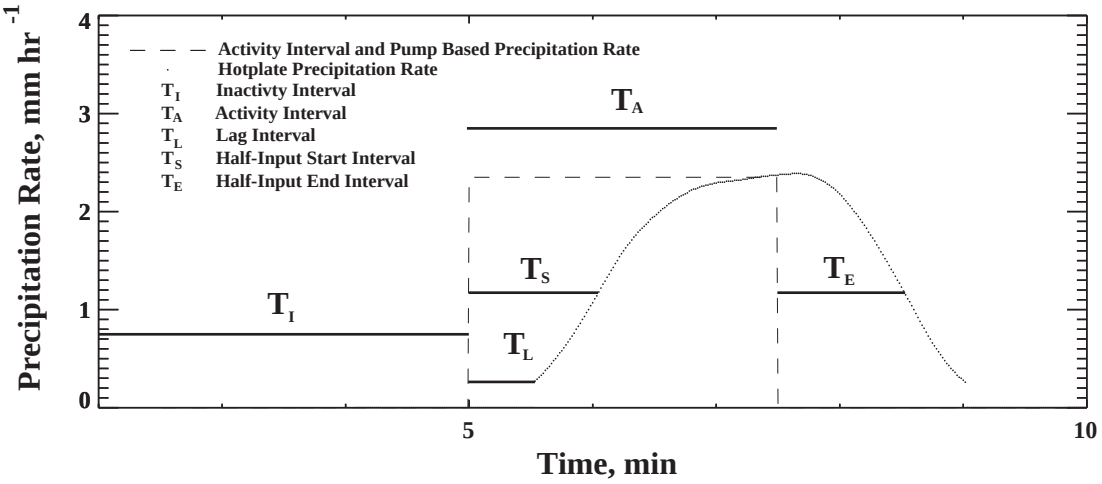

Figure 2.7 - Illustration of the inactivity interval (T_I), activity interval (T_A), half-input start interval (T_S), half-input end interval (T_E), and the lag interval (T_L) (Wolfe, 2007).

2.4 The Precipitation Algorithm

The YES Hotplate Algorithm derives the precipitation rate from the measured plate powers (reference and sensor plate power values) and the measured ambient temperature. Examples of the algorithm were presented in Figure 2.2 and 2.3. Because of the precipitation rate bias evident in those Figures, and the positive offset that occurred between the two water applications, a new algorithm was developed. As we shall see, this algorithm requires four calibration constants.

In this work the precipitation rate (pwl), derived via the Wyoming Hotplate Algorithm, was calculated as

$$pwl = C \cdot \alpha \cdot (\dot{Q}_{sens} - \dot{Q}_{der}) / E \qquad (3)$$

Here, $\dot{Q}_{sens}$ is the sensor plate power and $\dot{Q}_{der}$ is a heating rate derived from measurements of ambient wind speed and ambient temperature. Also, α is a temperature-dependent unit conversion factor, described in Section 2.9, C is one of the four calibration constants (Section 2.7), and E is the precipitation catch efficiency (Section 2.5).

Equation 3 differs from the YES Hotplate Algorithm in two fundamental ways: 1) the value of $\dot{Q}_{der}$ is derived, while in the YES Hotplate Algorithm it is evaluated using measurements of the reference plate power, and 2) the calculation of $\dot{Q}_{der}$ and C are based on the calibrations performed as part of this research.

Equation 4 shows the functional relationship used to describe $\dot{Q}_{der}$ in terms of the two temperatures (Hotplate temperature (T_{hp}) and ambient temperature (T_{∞})), the temperature-dependent thermal conductivity of air ($k(T_{\infty})$) and a wind speed-dependent parameter known as the Reynolds number (Re)

$$\dot{Q}_{der} = L \cdot k(T_{\infty}) \cdot (T_{hp} - T_{\infty}) \cdot (A_o \cdot \mathrm{Re}^{A_1} + A_2) \qquad (4)$$

In Equation 4 the Reynolds number is taken to be both temperature- and pressure-dependent via its dependence on the viscosity of air (υ) (see Equation 6 below). Constants in Equation 4 are L, the diameter of the Hotplate (L = 0.13 m), and T_{hp} = 348.15 K.

Equation 4 is formulated in the manner of the diffusive/convective heating equation applied to the airborne cloud water instrument developed by King et al. (1978). In neither King et al., nor here, is radiative heat transfer treated explicitly. On the right side of Equation 4, the term $A_o \cdot Re^{A1}$ describes the wind-speed dependent enhancement of the diffusive heating by air motion (wind). The form of the wind-enhancement is similar to that applied in the analysis of the King et al. instrument. The term A_2, also in Equation 4, describes the enhancement of the diffusive heating term by free convection. Values of the calibration constants A_o, A_1 and A_2 are presented in Sections 2.6, 2.8 and 2.10.

The calibration constants in Equation 4 (A_o, A_1 and A_2) were derived by fitting a relationship between two dimensionless quantities; the Nusselt number (Nu) and the Reynolds number (Re). In the curve fitting, the Nusselt number is expressed in terms of the measured values $\dot{Q}_{sens}$ and T_∞

$$Nu(\dot{Q}_{sens}, T_\infty) = \frac{\dot{Q}_{sens}}{L \cdot k(T_\infty) \cdot (T_{hp} - T_\infty)} \qquad (5)$$

and the Reynolds number is expressed in terms of the measured quantities U , T_∞ and ambient pressure (P).

$$Re(U, T_\infty, P) = \frac{L \cdot U}{\upsilon(T_\infty, P)} \qquad (6)$$

Here υ is the temperature- and pressure-dependent viscosity of air.

From Equation 5 it is evident that the Nusselt number is formulated using $\dot{Q}_{sens}$, the electrical power supplied to the top plate (Section 2.4). This approach would be biased if the $\dot{Q}_{sens}$ had a component due to precipitation. This bias was avoided by using a subset of the data record, those for which precipitation is very unlikely, to formulate the $Nu(\dot{Q}_{sens}, T_\infty)$ vs. $Re(U, T_\infty, P)$ parameterization. Criteria defining these "selected time intervals" are explained in Section 2.6.

2.5 The Catch Efficiency E

The precipitation catch efficiency (E) in Equation 3, is output in the $f1$ file. These values of E are used in the Wyoming Hotplate Algorithm. The value of E varies with ambient temperature (T_∞) and wind speed (U) in the following way: 1) if $T_\infty > 0$ °C, then $E = 1$ (for all wind speeds); 2) if $T_\infty < 0$ °C and $U < 9$ m/s, then E decreases linearly with wind speed as $E = 1.0 - 0.086 \cdot U$; and 3) if $T_\infty < 0$ °C and $U > 9$ m/s, then $E = 0.2$. The E/U relationship was derived by comparing the Hotplate to a reference gauge (Rasmussen et al., 2005). In these comparisons the reference gauge is operated inside two rings of fences, so the reference gauge is said to be "double fenced" (Yang et al., 2000; Rasmussen et al., 2005). Inefficient catch of snow by the Hotplate, relative to the double-fenced reference, occurs because a fraction of the snow particles striking the Hotplate are blown off prior to their evaporation. This fraction increases with increasing wind speed.

2.6 The Calibration Constants A_o, A_1 and A_2

Table 2.3 reports the dates, times and locations of experiments that were used to derive the calibration constants A_o, A_1 and A_2. The data come from the three locations described in Section 2.1 (Laboratory, Hangar and GLEES). Important differences between these locations are the temperature and pressure of the Laboratory (21 °C and 780 hPa), of the Hangar (-5 °C and 780 hPa), and of the field

measurements (variable temperature and 670 hPa). For brevity, these measurements will be referred by the case numbers shown in the first column of Table 2.3. Calibration constants, derived for each case, are shown in fifth, sixth and seventh columns of Table 2.3. The GLEES data in Table 2.3 came from the time intervals selected to be free of precipitation. The selection criteria are, 1) no precipitation detected by the Hotplate ($pf1$ time series), 2) relative humidity less than 40%, and 3) clear sky weather conditions reported both at the Rawlins, WY and Laramie, WY airports (i.e., no clouds). Since the relative humidity at night is often larger than 40%, and the $pf1$ time series is often positively biased during nighttime, these criteria eliminated nighttime intervals for those selected to be free of precipitation. The values of A_o, A_1 and A_2 used in the Wyoming Algorithm are selected in Section 2.10.

Table 2.3 Measurement intervals when the Hotplate was not exposed to precipitation (field data) or to water from the pump (Laboratory and Hangar)

Case	Date	Start Time and Stop Time, UTC	Place of Measurement	Best-fit Calibration Constants		
				A_0	A_1	A_2
0	20070410	192300 - 192445 194330 - 194430	Laboratory [a]	0.057	0.782	59.503
1	20070515	222800 - 222830 224750 - 224900	Laboratory [a]	0.057	0.783	62.010
2	20070515	225820 - 225845 232623 - 232710	Laboratory [a]	0.059	0.778	70.781
3	20070516	230525 - 230555 230840 - 230950 231730 - 231845	Laboratory [a]	0.058	0.780	64.897
4	20070516	221300 - 221600 221938 - 222051 222834 - 222951	Laboratory [a]	0.061	0.777	59.040
5	20080208	223200 - 223500 224030 - 224130 225130 - 225230 230230 - 230330	Hangar [b]	0.056	0.773	65.869
6	20080222	235400 - 225530 235910 - 240010 001000 - 001100 002100 - 002200 002630 - 002730	Hangar [b]	0.052	0.780	65.360
7	20070413	150000 - 170000	Field [c]	0.065	0.769	51.599
8	20070415	181500 - 200000	Field [c]	0.050	0.791	64.276
9	20070418	181230 - 183755	Field [c]	0.059	0.762	78.637
10	20070524	210000 - 214500	Field [c]	0.056	0.779	65.686
11	20070525	170000 - 192000	Field [c]	0.058	0.770	68.045
12	20070527	210000 - 233000	Field [c]	0.062	0.770	66.644
13	20070602	160000 - 190000	Field [c]	0.059	0.780	60.069
14	20070606	140000 - 160000	Field [c]	0.061	0.767	75.786
15	20070613	170000 - 190000	Field [c]	0.049	0.793	69.885

[a] Experiment done in the Laboratory [b] Experiment done at the Hangar

[c] Field data measured at GLEES.

Figure 2.8 shows the Nu / Re values derived at two blower settings (0 m/s and ~7.5 m/s), in the Laboratory (left column of panels) and in the Hangar (right column of panels), respectively. The top panels show all of the data, the middle panels zoom in on values obtained at 0 m/s (unventilated), and the bottom panels zoom in on values acquired at 7.5 m/s (ventilated). Also plotted is the best-fit line corresponding to the fitted coefficients A_o, A_1 and A_2.

In all six panels, and particularly in the middle two panels and in the two bottom panels, it is apparent that the data values plot in discrete clumps. This results from the format of the $f1$ file which reports the temperature with 0.1 ^{o}C resolution, the wind speed with 0.1 m/s resolution and the sensor power with 0.1 W resolution.

In the middle two panels of Figure 2.8 it can be seen that Nu exceeds unity even when the wind speed is 0 m/s. This departure from $Nu = 1$ at $Re = 0$ suggests that free convection or radiation, are substantial relative to heat diffusion. Also, it appears that the combination of diffusion, free convection and radiation produce a heat dissipation rate which is about one sixth of the rate for a Hotplate ventilated at $U = 7.5$ m/s. This apportionment of the heat budget is discussed further in Section 2.8.

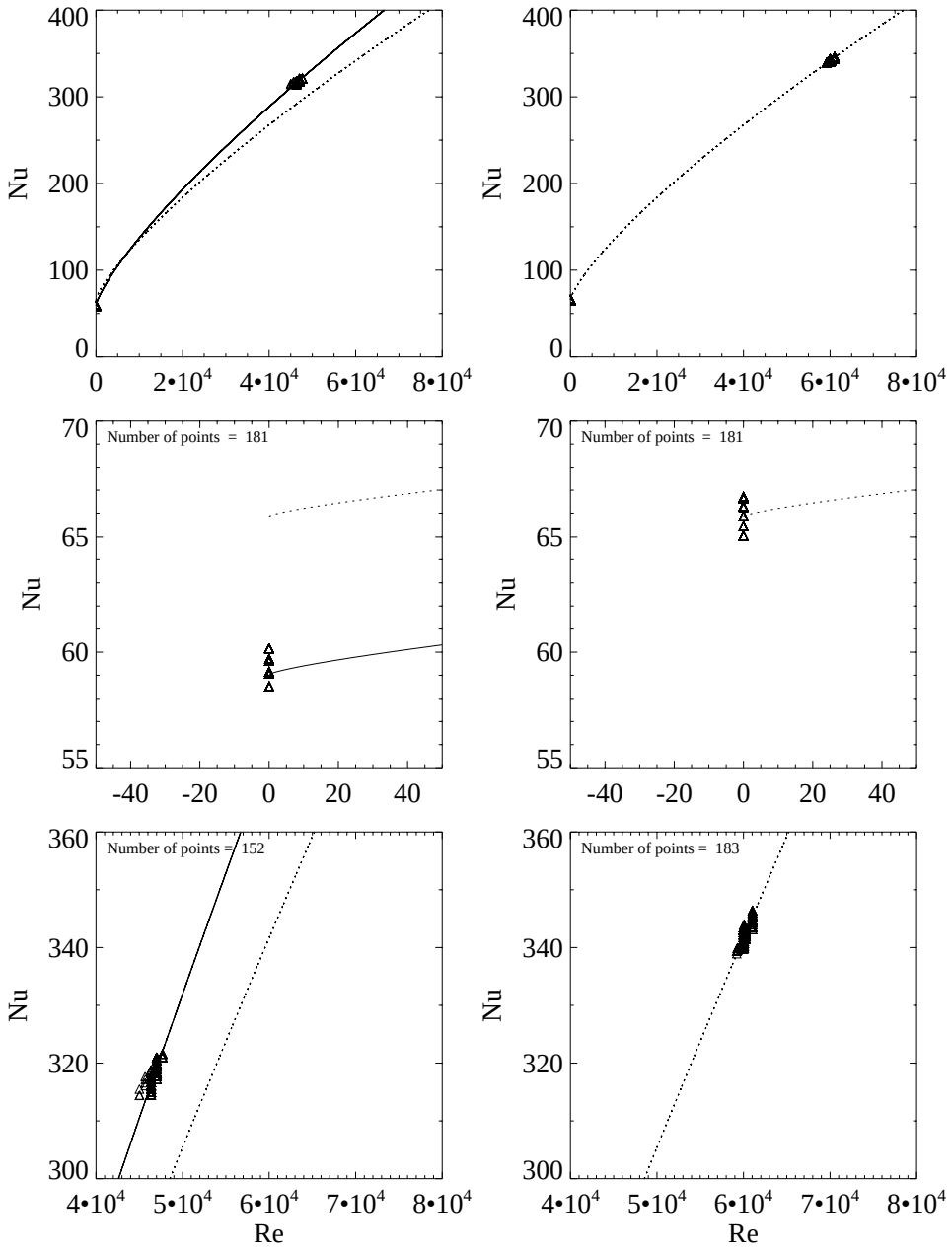

Figure 2.8 - Nusselt versus Reynolds number and the fitted relationship. Shown in the left and right columns are results from Cases #4 (Laboratory) and #5 (Hangar), respectively. Top panels) both unventilated and ventilated experiments; middle panels) unventilated experiments; and bottom panels) ventilated experiments. The Case #4 (Laboratory) and Case #5 (Hangar) fit lines are shown in solid and dashed lines, respectively.

2.7 The Calibration Constant C

In this section, the calibration constant symbolized as "C" is evaluated (Equation 3). Figure 2.9 shows the experimental data that enter into the determination of C. Before going into the detail of how these points were evaluated, a definition of C is necessary. The C is a scaling factor which, on average, makes reference precipitation rate (Equation 2) equal to the derived precipitation rate (Equation 3). In practice, C is evaluated as the slope of a line passing through points with Y coordinate the reference precipitation rate and X coordinate from Equation 3 with C=1. The fitted values are time averaged over the central portion (2 min) of the four minute water delivery interval (Section 2.3). In Figures 2.9, 2.10 and 2.11 the lines are the best-fits, the triangles are measurements from ventilated experiments, and the circles are measurements from unventilated experiments.

Figure 2.9 shows all points plotting above the one-to-one line, indicating a significant bias in the manufacturer's calibration. Also, data points from the ventilated experiments plot above those from the unventilated experiments. The best-fit line slopes are 1.75 and 1.38, respectively. The fact that the slope for the ventilated experiments is larger than for the unventilated experiments suggests that less energy, derived from the sensor plate (i.e., the top plate), is needed to evaporate ventilated drops. This effect is attributed to the fact that ventilation narrows the boundary layer over the drop surface and thus enhances air-to-drop energy transfer relative to the situation without ventilation.

The hypothesis stated in the previous paragraph was tested by stratifying the data into big drop experiments (left panel, Figure 2.10) and small drop experiments (right panel, Figure 2.10). The big and small drop sizes were produced using delivery tubes with inner diameters (ID) of 0.7 mm and 0.4 mm, respectively. The drop diameters are approximately 3.8 mm (big drop) and 2.8 mm (small drop). The average value and standard deviation of water flow rates during these experiments are in Table 2.2. Figure 2.10 demonstrates that the slopes are smaller for the experiments with small drops. This finding is consistent with speculation presented in the previous paragraph, i.e., compared to large drops, the small drops are not as strongly coupled to the wind and thus get a larger fraction of their evaporation energy from the Hotplate.

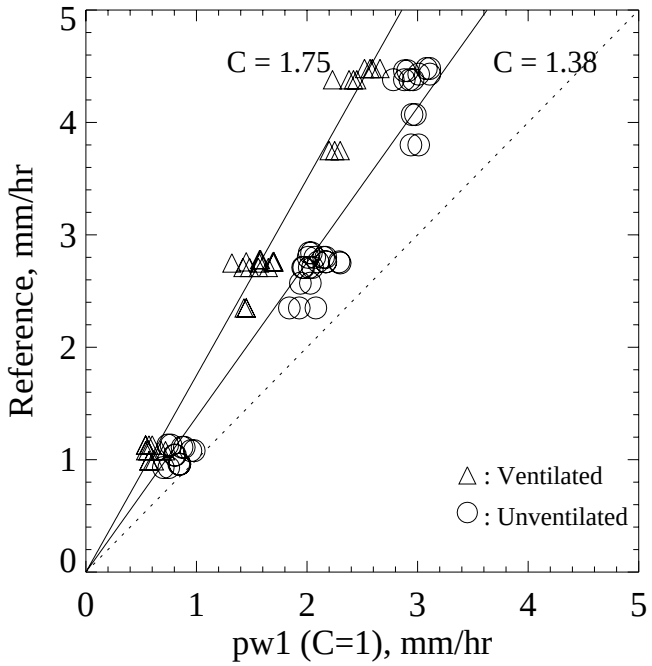

Figure 2.9 - Calibration of C in the Laboratory under ventilated and unventilated conditions. Included are all of the small drop experiments and all of the big drop experiments.

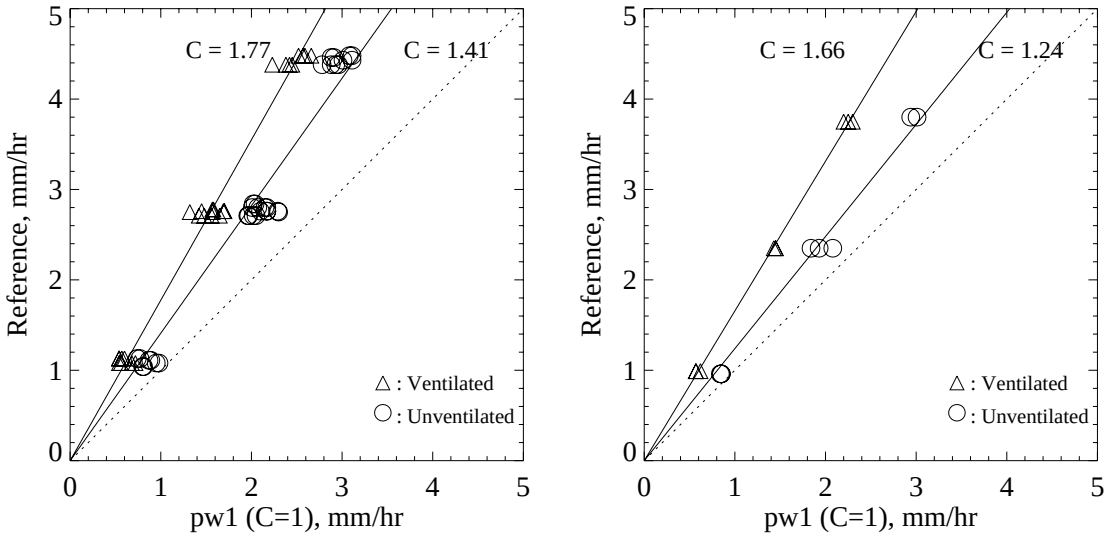

Figure 2.10 – As in Figure 2.9, but for left panel) experiments with big drops and right panel) experiments with small drops.

2.8 Measurements at the University of Wyoming Balloon Hangar

The previous two sections discussed how values of A_o, A_1, A_2 and C are evaluated. These assessments were based on measurements made in the relatively warm Laboratory (A_o, A_1, A_2 and C) and at the colder GLEES site (A_o, A_1 and A_2). Now the focus turns to calibrations (A_o, A_1, A_2 and C) conducted in a cold, indoor setting. The venue for these experiments is the Hangar described in Section 2.1. The Hangar has a high ceiling (~10 m), the space is heated to maintain the Hangar at approximately 0 ^{o}C and the hanger floor is concrete. The Hangar measurements were conducted to see if there was a noticeable shift between the Laboratory and GLEES calibrations (Table 2.3).

The Nu / Re fits derived using data collected in the Laboratory and Hangar are presented in Figure 2.8. Most telling is the comparison shown in the middle-left panel which has the Laboratory data, and its fit curve (solid line), plotted with the fit curve corresponding to the Hangar data (dashed line). These results are for no ventilation.

Because of the way the Nu is formulated (Equation 5), as a ratio of the electrical heating rate divided by the diffusive heating rate, it might be expected that Nu should be comparable to unity during unventilated experiments. The fact that this is not the case (Nu ~63) is an evidence for the importance of radiative and free-convective heat transfer for the unventilated Hotplate. With the exception of Case #2 (Table 2.3), this speculation about radiation and free-convection is consistent with the observation that A_2 is larger for the Hangar experiments, presumably because the

radiation environment in the Hangar is characterized by a radiative temperature (0 ^{o}C) which is smaller than in the Laboratory (21 ^{o}C). A colder environment implies less infrared radiation received by the Hotplate to compensate for infrared radiation it emits. It is also true that the intensity of visible light was larger in the Laboratory experiments, and that this radiative difference could explain the fact that A_2 is generally larger for the Hangar experiments. Since no attempt was made to quantify these radiative effects the contrast evident from Table 2.3, for the Laboratory and Hangar experiments, must be taken to be speculative.

Another contrast is apparent in the result shown in the bottom-left panel of Figure 2.8, where at large Reynolds number the Hangar best-fit line is seen plotting to the right of the Laboratory data. A plausible explanation for this result is that the colder Hangar floor is biasing the Hotplate wind speed (positively), and thus enhancing the Hangar values of U and Re relative to the Laboratory values of U and Re. This result is disconcerting because it suggests that the wind speed output by the Hotplate can vary depending on the radiation environment it is placed in. Equation 4 shows that the fit parameter A_2 accounts for this radiative effect but not using an a priori description of radiative heat transfer. Similarly, the Equation 4 does not explicitly model the effects of solar radiation or artificial lighting.

The Hangar assessments of C are shown in Figure 2.11. Because of the wind bias discussed in the previous paragraph the values of $pw1$, on the x axis, are calculated using the coefficients (A_o, $A_1 and\ A_2$) from the Case #5 (Hangar). If the

Case #4 calibration is applied to the ventilated Hangar assessments of C, then the Nu number is too large and the value of $pw1$ is biased negatively. In the Figure 2.11 the slopes are $C = 1.80$ (ventilated) and $C = 1.41$ (unventilated).

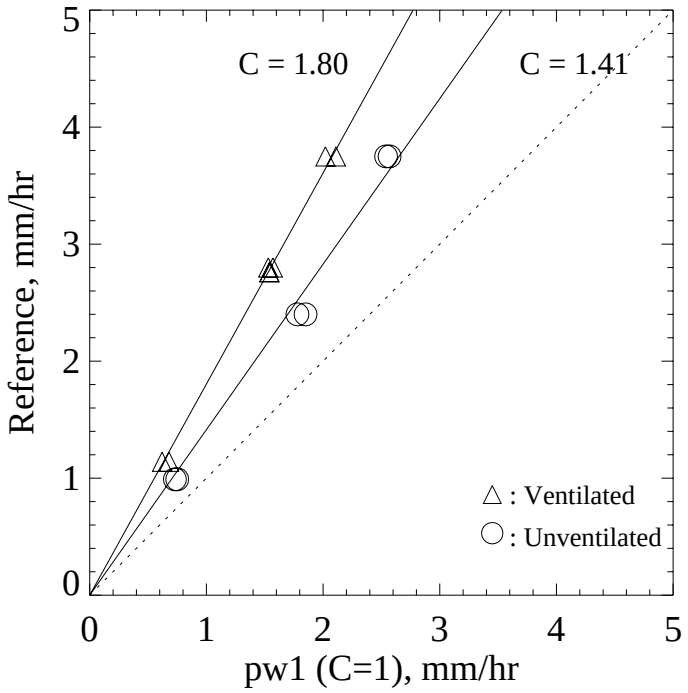

Figure 2.11 - Calibration of C at Hangar under ventilated and unventilated conditions. Coefficients (A_o, $A_1 and\ A_2$) from the Case #5 and α = 2.853·10^{-8} m/J (Section 2.9) are applied in the data processing.

2.9 The temperature-dependent unit conversion factor - α

In Equation 3 (Section 2.4), the term $\left(\dot{Q}_{sens} - \dot{Q}_{der}\right)$ is the sensor plate power attributable to precipitation. The factor α in Equation 3 converts the measured power to a liquid-equivalent precipitation rate. The value of α can be related to the area of the Hotplate, the density of liquid water (ρ_w) and to a thermodynamic factor (β)

$$\alpha = \frac{1}{A \cdot \rho_w \cdot \beta} \qquad (7)$$

The β is the energy required to vaporize a unit mass of precipitation and is dependent on the phase (liquid or solid) of the precipitation and the ambient temperature. For ice-phase precipitation (snow) β has contributions from four terms: 1) the energy required to warm the ice to 0 ^{o}C, 2) the energy required to melt the ice, 3) the energy required to warm the liquid to the temperature of the Hotplate, and 4) the energy required to vaporize the liquid at the Hotplate temperature.

$$\Delta E_1 + \Delta E_2 + \Delta E_3 + \Delta E_4 = \beta \qquad (8)$$

In Equation 8, ΔE_1 is an energy required to bring ice from the ambient temperature ($T_\infty < 0$ ^{o}C) to melting temperature ($T_o = 0$ ^{o}C); ΔE_2 is an energy required to melt the ice at T_o; ΔE_3 is an energy required to bring the liquid from T_o to the Hotplate

temperature (T_{hp}); and ΔE_4 is the energy required to evaporate water substances at T_{hp}. These energy terms are related to temperature via the following equations:

$$\Delta E_1 = c_i \cdot (T_\infty - T_o) \quad (9)$$

$$\Delta E_2 = l_f (T_o) \quad (10)$$

$$\Delta E_3 = c_w \cdot (T_{hp} - T_o) \quad (11)$$

$$\Delta E_4 = l_v (T_{hp}) \quad (12)$$

Here c_i is specific heat capacity of ice, l_f is the latent heat of fusion, c_w is the specific heat capacity of liquid water and l_v is the latent heat of vaporization.

Figure 2.12 shows the three states of the water substance and the temperature at which each of the four energy terms were evaluated. Table 2.4 presents the quantity of energy required for each process and their contribution to β, expressed as a percentage.

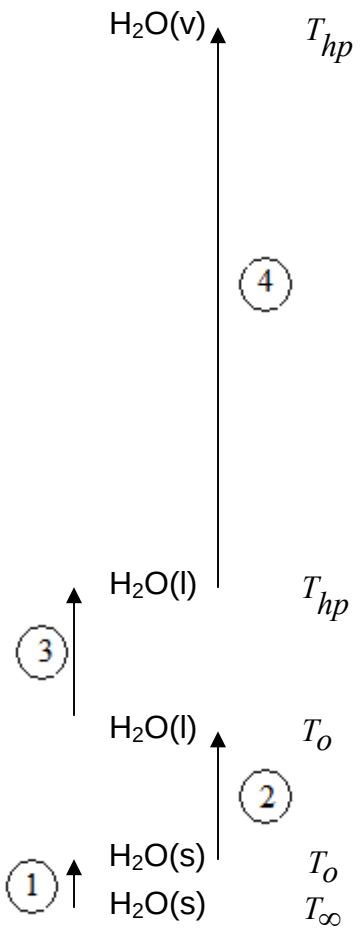

Figure 2.12 – States (solid = s, liquid = l, vapor = v) of the water substance during the sequence of steps leading to evaporation. Also shown are the four steps, discussed in the text and the temperatures defining each of the states.

Table 2.4 - Energy required melting, heat and evaporating the water substance at 75 ^{o}C. Four scenarios for the initial state are considered, ice at -10 ^{o}C, ice at 0 ^{o}C, liquid at 0 ^{o}C and liquid at 10 ^{o}C. The final column has the temperature-dependent unit conversion factor (α) defined by Equation 7.

Initial phase	T_∞, ^{o}C	ΔE_1 J/kg	ΔE_2 J/kg	ΔE_3 J/kg	ΔE_4 J/kg	β J/kg	α m/J
Liquid	+10	NA	NA	274170 **(10.5)***	2324655 **(89.5)***	2598825 **(100)***	$2.899 \cdot 10^{-8}$
Liquid	0	NA	NA	316350 **(12.0)***	2324655 **(88.0)***	2641005 **(100)***	$2.853 \cdot 10^{-8}$
Solid	0	0 **(0.0)***	333700 **(11.2)***	316350 **(10.6)***	2324655 **(78.2)***	2974705 **(100)***	$2.533 \cdot 10^{-8}$
Solid	-10	21060 **(0.7)***	333700 **(11.1)***	316350 **(10.6)***	2324655 **(77.6)***	2995765 **(100)***	$2.515 \cdot 10^{-8}$

* Contribution to β expressed as a percentage

2.10 Overall Comparison of the A_o, A_1 and A_2 Calibrations

In Sections 2.6 and 2.8 a significant shift was detected between the Laboratory and Hangar calibration coefficients A_o, A_1 and A_2. Because these coefficients establish a baseline for the precipitation rate (Equations 2 and 3) it is important to quantify how variability in the coefficients (Table 2.3) injects uncertainty into the precipitation rate. This was accomplished by applying the 16 sets of coefficients (Table 2.3) to each of the 16 selected time series (Section 2.6). The 16 plots are presented in Appendix A.

An example is shown in Figure 2.13 where the set of calibration coefficients from Case #4, a Laboratory experiment, is applied to each of the selected time intervals. In the top panel is the time-average of $C \cdot \alpha \cdot (\dot{Q}_{sens} - \dot{Q}_{der})$ and in the bottom panel is the time-average of the precipitation rate. Error limits (both panels) represent the average plus and minus one standard deviation. Since the coefficients A_o, A_1 and A_2 from Case #4 are applied, the Case #4 average plots exactly at zero in both the top and bottom panels. It is also evident that the two cases from the Hangar (#5 and #6) plot below the zero line. This is expected from the upper-left panel of Figure 2.8 which shows the fit lines for the Case #4 (Laboratory, solid line) and Case #5 (Hangar, dotted line). Since the Case #4 line lies above the Case #5 line ($Re > 10^4$), the application of the Case #4 fit to Case #5 produces a positive bias

in $\dot{Q}_{der}$ for Case #5 and thus a negative bias in the precipitation rate for Case #5. This logic is made evident by viewing Equation 3.

Figure 2.13 shows that the precipitation rate average ($\langle pwl \rangle$) is negligible, relative to zero, for several of the field cases (#8, #10, #12, #13 and #14). These small departures can be contrasted with the larger departures documented in the Appendix A. In fact, it was just that type of comparison which led to the choice of the Case #4 fit for analyzing both the Laboratory and Field Hotplate data. Notable exceptions to the occurrence of negligible $\langle pwl \rangle$ departure are three Cases from the GLEES: #7, #11 and #15. All of the three cases occurred close to local noon (Table 2.3), and were associated with clear sky conditions and thus strong solar input to the Hotplate (~1000 W/m^2, see Section 2.11). It is expected that the solar radiative input was substantially larger than the input from artificial lighting in the laboratory. Hence, it is expected that all three cases should depart negatively in Figure 2.13. Since Case #15 departs positively, this was investigated further. An examination of the *Nu/Re* fit line for Case #15 revealed that it plots above the fit line for Case #4; just the opposite was found for Cases #7 and #11. This comparison demonstrates that a relatively small shift in the fitted *Nu/Re* relationship - detected by plotting the calibration data in the manner of Figure 2.8 - can drive the Wyoming Hotplate Algorithm from indicating the occurrence of significant precipitation at the GLEES site ($\langle pwl \rangle > 0.4$ mm/hr) to indicating a precipitation rate less than zero.

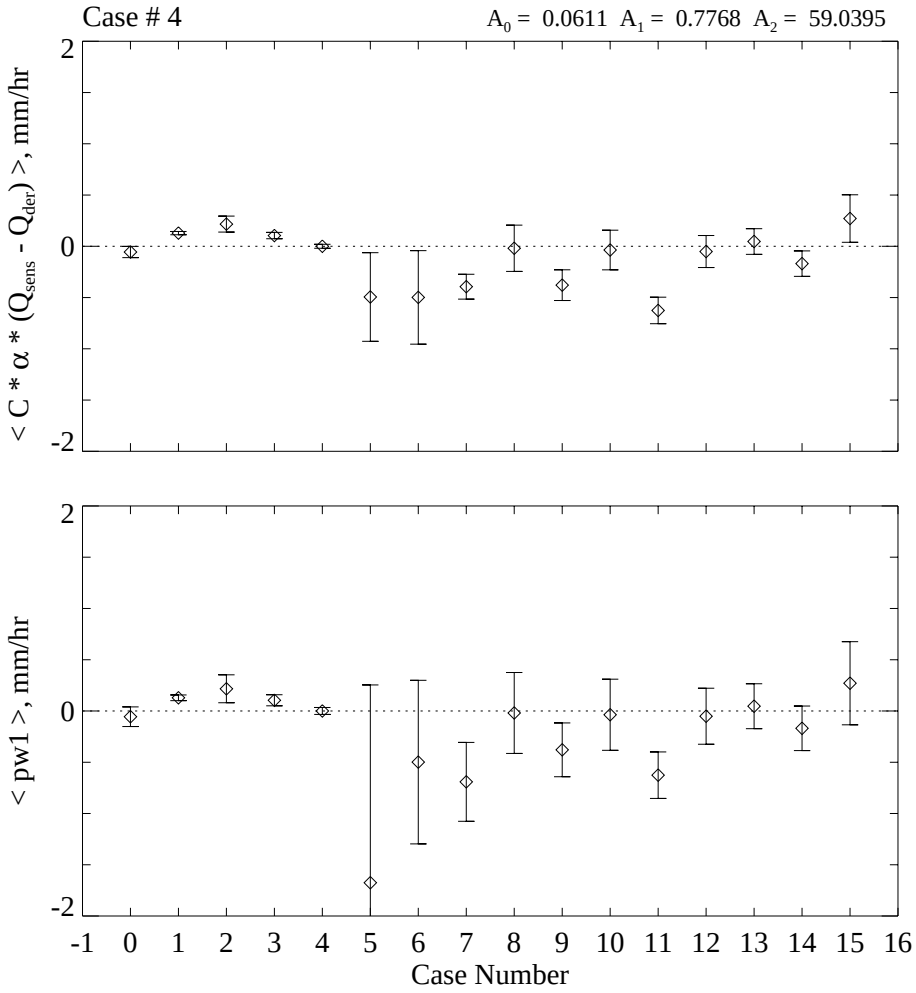

Figure 2.13 – Examination of the averages and variability from the selected time intervals. Top) Time-average of $C \cdot \alpha \cdot (\dot{Q}_{sens} - \dot{Q}_{der})$; Bottom) Time-average of the precipitation rate (Equation 3). Error limits are represented by the average plus and minus one standard deviation.

In addition, an examination of data from all of the selected cases from GLEES reveals departures of $\langle pwl \rangle$ from zero for averaging intervals as short as 26 min (Case #9, Table 2.3) to as long as 180 min (Case #13, Table 2.3).

In summary, the bottom panel of Figure 2.13 shows that the fit coefficients from Case #4 produces a precipitation rate which is within ±0.8 mm/hr of zero for all cases except the Case #5. The values of A_o, A_1 and A_2 chosen for the Wyoming Algorithm are from Case #4: A_0=0.061, A_1=0.777 and A_2=59.

2.11 The Threshold Precipitation Rate

This section explains the threshold that was applied to the values of precipitation rate derived via Equation 3. The threshold is needed for reasons discussed in Section 2.2.b where it is demonstrated that the Hotplate reports a residual precipitation rate ($pf1>0$) even when it is not being stimulated with water from the calibration pump. Evidence for the residual is also seen in Figure 2.13 where it is seen that averages of $pw1$ derived for most of the selected time intervals are non-zero. Both figures demonstrate that a significance bias can result from time integration of the precipitation rate; for example, a residual value of $pw1$ equal to 0.4 mm/hr integrated over 24 hour produces an accumulation bias equal to ~10 mm.

Figure 2.14 suggests that radiative terms in the Hotplate's heat budget are significant drivers of the occurrence of a non-zero precipitation rate when the instrument is not exposed to precipitation. Shown here are data from the Hotplate (panels a, b, e and f) combined with measurements from co-located radiation sensors (panels c and d). The radiation measurements are every 30 min reported values of upward and downward propagating radiation intensity, both long wavelength (LW) and short wavelength (SW), acquired from AmeriFlux radiation sensors operated on the same tower as the Hotplate (Section 3.3; Chapter III). The time interval is from 1800 UTC on 20070412 to 1800 UTC on 20070413 - start and stop times correspond to local noon – and encompass the selected time interval for the Case #7. The start

and stop times for the Case #7 are 1500 UTC and 1700 UTC on 20070413, respectively.

Ideally the value of pwl (panel " a ") should be zero for every second of the time series. Departures from this expectation (residuals) occur both positively and negatively and the integrated effect is shown in panel " b " with a positive bias occurring during the night and a negative bias occurring during the daytime of 20070413. The sign of these biases are consistent with the following explanation. During the daytime, the SW input to the Hotplate is large, maximizing at 1000 W/m^2. Hence, less (more) electrical power is required to maintain the Hotplate at a constant temperature (T_{hp}) during the daytime (nighttime), compared to that anticipated by the wind- and temperature-dependence of the $\dot{Q}_{der}$ (Equation 4). The effect of the SW heating is evident between 1400 and 1800 UTC on 20070413 where the values of pwl are negative. In addition there is a modulation of the radiation input to the Hotplate by clouds. Evidence for this is seen at ~1900 UTC on 20070412 where the SW intensity is reduced to ~600 W/m^2 in association with an increase of the average of pwl relative to the situation near solar noon on 20070413.

Figure 2.14 and Figure 2.15 demonstrate the effect of radiation on the precipitation rate predicted by Equation 3 that varies diurnally, and with clouds. These phenomena are difficult to account for quantitatively, and because of these complexities, a simplistic condition was applied to precipitation rates derived from Equation 3. A value of +0.8 mm/hr was taken to be a threshold which Equation 3

must exceed for non-zero values of the precipitation rate to be outputted from the Wyoming Hotplate Algorithm. Specifically, there are two threshold conditions applied in Wyoming Hotplate Algorithm: 1) if $pwl < 0.8$ mm/hr then the value of pwl is set to zero, and 2) if $pwl \geq 0.8$ mm/hr then the value of pwl is accepted as valid.

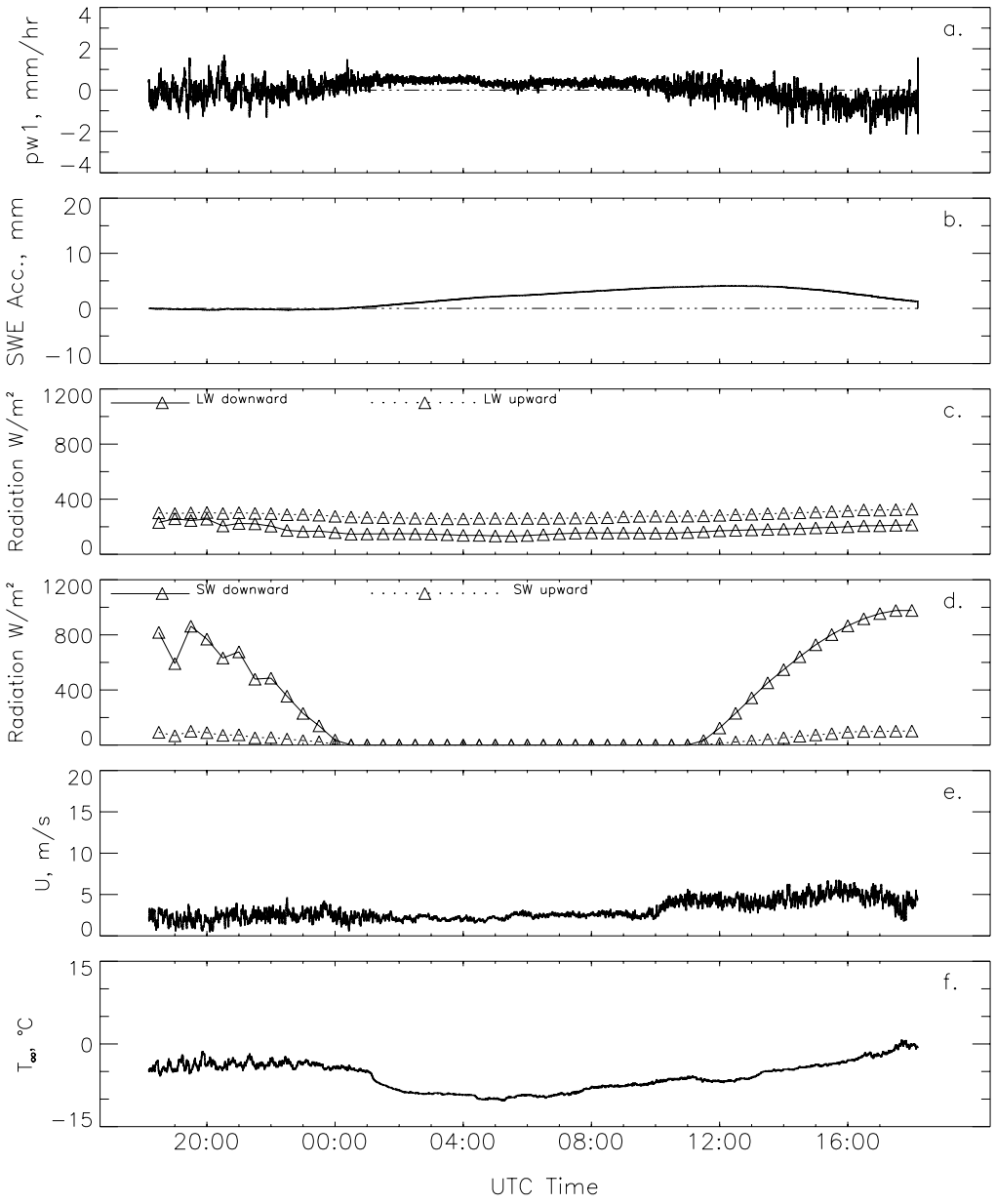

Figure 2.14 - Time series of Wyoming Hotplate Algorithm (panel " a ") and its accumulation (panel " b "). The lower panels are time series of AmeriFlux measurements of radiation fluxes and Hotplate measurements of wind speed (derived) and ambient temperature. Time series starts 1800UTC on 20070412.

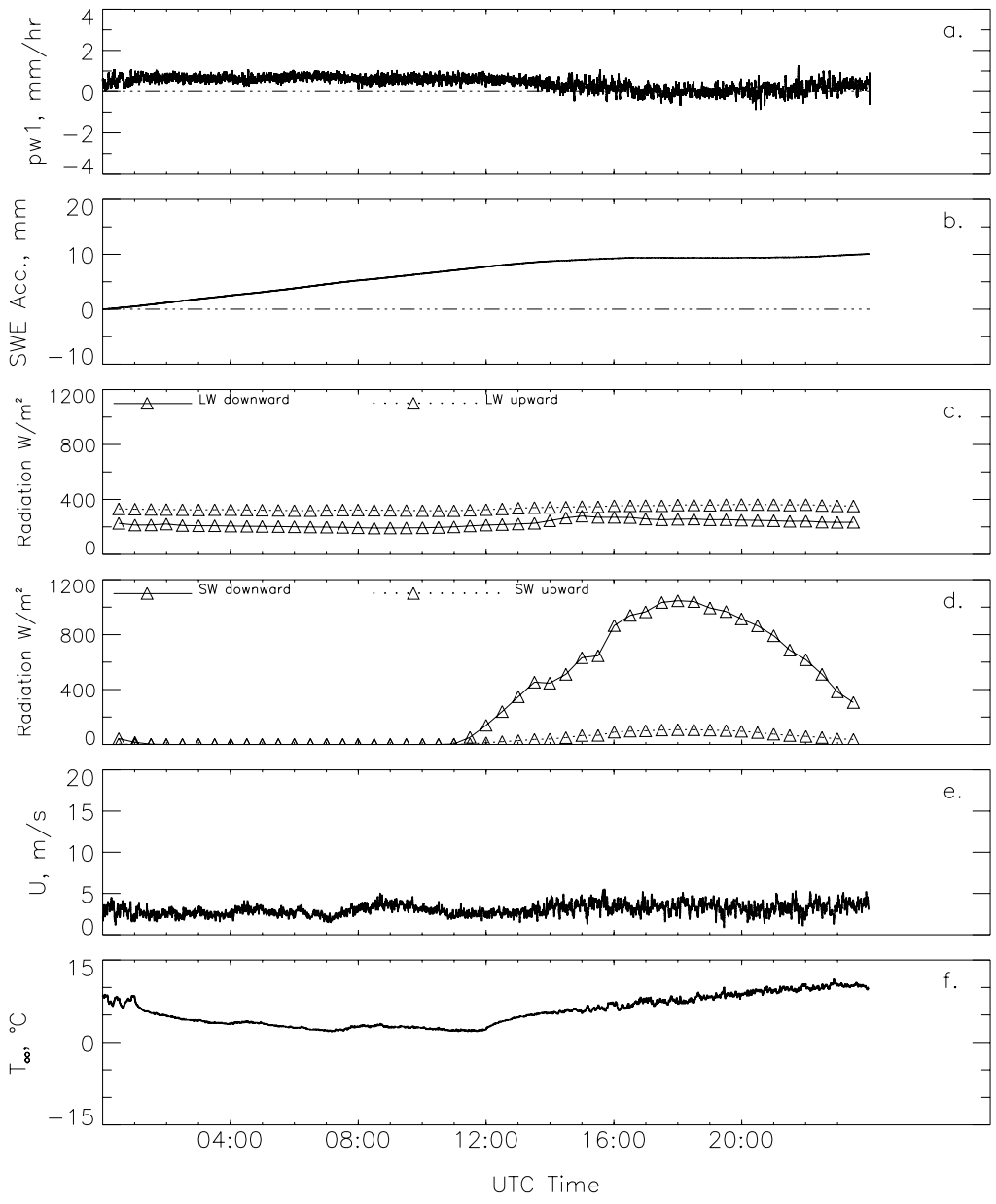

Figure 2.15 – As in Figure 2.14, but for 20080517.

2.12 Summary

In this chapter, a data processing algorithm (called Wyoming Hotplate Algorithm), is described. The algorithm is applied to data acquired using the YES Hotplate operated by the University of Wyoming Department of Atmospheric Science between April 2007 and June 2008. The algorithm is summarized in Table 2.5.

Table 2.5 Summary of the Wyoming Hotplate Algorithm

Parameter	**Parameterization**	**Where Described**
Catch efficiency, E	$1.0 - 0.086 \cdot U$	Section 2.5
A_0, A_1 and A_2	$A_0 \cdot Re^{A_1} + A_2$ $0.061 \cdot Re^{0.777} + 59.$	Section 2.6
C	1.75	Section 2.7
α	$2.5 \cdot 10^{-8}$ m/J to $2.9 \cdot 10^{-8}$ m/J	Section 2.9
Threshold	+0.8 mm/hr	Section 2.11

Chapter III: Measurements

3.1 Introduction

In Chapter II, a new type of precipitation gauge, the Hotplate, is introduced. This chapter describes the field measurement site and the five other snow measurement sensors which are compared to the Hotplate. Field measurements were conducted the Glacier Lakes Ecosystem Experiments Site (GLEES) located in the Medicine Bow Mountains of southeastern Wyoming at an elevation of approximately 3300 m. The five supplementary sensors are: 1) the Alter-shielded Belfort gauge located at the Brooklyn Lake National Atmospheric Deposition Program (NADP) site, 2) the unshielded sample volume sensor at the NADP site, 3) the unshielded Vaisala Rain Gauge (VRG), 4) the Alter-shielded gauge located at the Brooklyn Lake Snow Telemetry (SNOTEL) site, located 1 km southeast of the NADP site, and 5) a snow pillow located at the Brooklyn Lake SNOTEL site.

3.2 Site Description

The locations of the sensors are illustrated in Figure 3.1. Four of these (NADP-gauge, NADP-sample-volume, VRG and the Hotplate) are located within 200 m horizontal distance and other two (SNOTEL-gauge and SNOTEL-pillow) are located within approximately one km of the other four. The five surface-based precipitation sensors (NADP-gauge, NADP-sample-volume, VRG, SNOTEL-gauge and SNOTEL-pillow) were in close proximity to groves of Engleman spruce (Picea

englemanii) and Subalpine fir (Abies lasiocarpa) trees that have a maximum height of 15 m. As will be seen these trees are important for the comparison of precipitation data from the tower-based sensor (Hotplate) with the five surface-based sensors.

Figure 3.2 is an aerial photo of a portion of the GLEES site. The Brooklyn Lake NADP site (gauge and sample volume) is located at the western end of a 200 m wide clearing, and the VRG sensor is located in a smaller clearing (width approximately 50 m). At the GLEES site the prevailing wind direction is from the west; this is made evident by the two snow drifts seen north of the NADP and extending out of the grove of trees extending from southwest to northeast. The one of these drifts was probed in May 2008; results are presented in Figure 3.3. The depth of the drift increases by ~1 m over a 3 m horizontal distance. This observation provides evidence that the precipitation measurements made at the NADP may be overestimated because of the unintentional sampling of wind-resuspended ice particles. This is discussed further in Section 3.9.

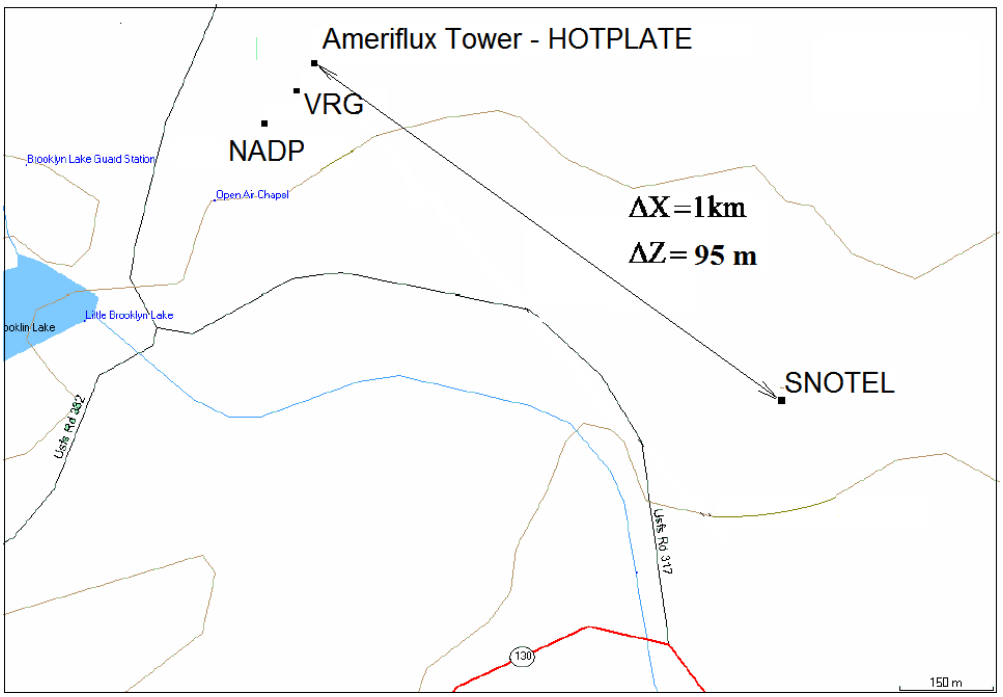

Figure 3.1 - Location of the six precipitation sensors in the Medicine Bow Mountains of southeastern Wyoming. In the map, the sites selected for this thesis are indicated by names. The horizontal and vertical distances separating the AmeriFlux and SNOTEL sites are indicated. The difference in vertical distance (ΔZ) corresponds to the height change between the top of AmeriFlux tower (where the Hotplate sensor was located) and the altitude of the Brooklyn Lake SNOTEL site.

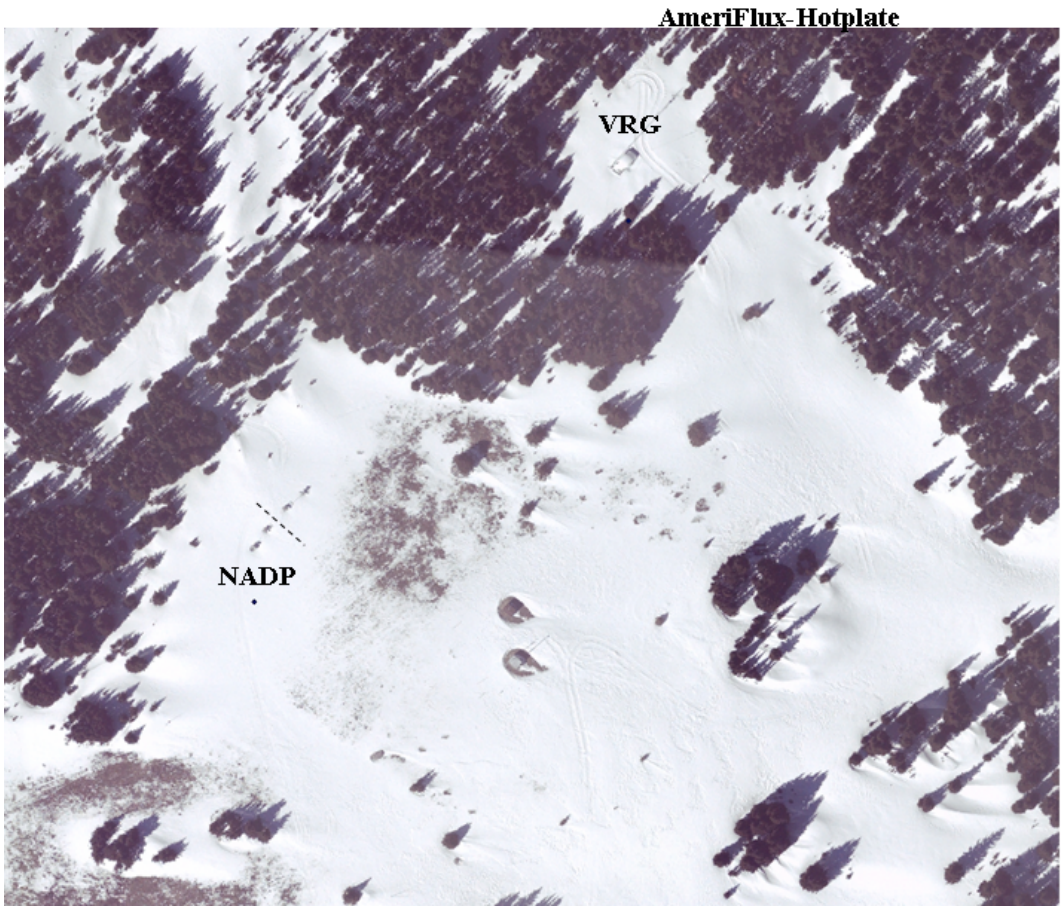

Figure 3.2 – The location of the Brooklyn Lake NADP site at the GLEES. The NADP operates two precipitation monitors (gauge and sample volume) in a meadow downwind of an evergreen grove. The elevation of the Brooklyn Lake NADP site is 3181m. The picture is courtesy of Chris Hiemstra; Colorado State University.

Figure 3.3 – Snow depth measurements made near the NADP-gauge at the GLEES. Picture is taken on 20080519. At left is the Alter-shielded NADP-gauge. To the right there are two probes inserted to the soil surface indicating the snow depth increases ~1 m in a horizontal distance of ~3 m. The probes were positioned along the dashed line shown in Figure 3.2.

The precipitation climatology at GLEES, based on measurements made between 1976 and 1988, is presented by Sommerfeld (2004). He shows that 70 to 80% of the annual precipitation occurs as snowfall; that the winter season snowpack accumulates from October to April, and persists until June or July; and that the monthly-averaged precipitation for November, December, January, February, March and April is 126, 116, 87, 93, 132, and 93 mm, respectively.

3.3 Hotplate

The Hotplate was located on the top of the 30 m AmeriFlux tower, approximately 15 m above tree tops. Figure 3.4 shows the Hotplate installed in the northwest corner of the tower. In Figure 3.1 it is seen that the AmeriFlux tower is located 70 m northeast of the VRG. AmeriFlux data used in this thesis were obtained online at http://public.ornl.gov/ameriflux/data-access-select.shtml (28 June 2009).

The Hotplate requires 600 W of electrical power; this was obtained from the line power available at the AmeriFlux site. The Hotplate's data recording computer was operated in the instrument hut at the base of the tower; data acquisition was via a wireless connection, in 2008, and via a wired connection during 2007. Approximately twice a month the AmeriFlux hut was visited, so that data could be retrieved from the Hotplate computer, and so that the Hotplate could be reinitialized if a power outage had occurred.

The first Hotplate deployment was in December 2006, but an examination of the data revealed a significant negative offset in the values of *php* (precipitation rates

were underestimated by approximately 5 mm/hr). Because of the offset the Hotplate was sent to NCAR in February 2007 and during February and March some of the calibration constants in the YES Hotplate Algorithm were adjusted. On March 16, 2007 the University of Wyoming signed a nondisclosure agreement which allowed us to have access to the $f1$ file described in Section 2.2.a. The Hotplate was redeployed at the GLEES on April 12 and collected data until June 22, 2007. The Hotplate was deployed again on March 23, 2008 and was operated until June 14, 2008. Power outages during both the 2007 field season, and to a lesser degree during the 2008 field season, limited the amount of data that was acquired.

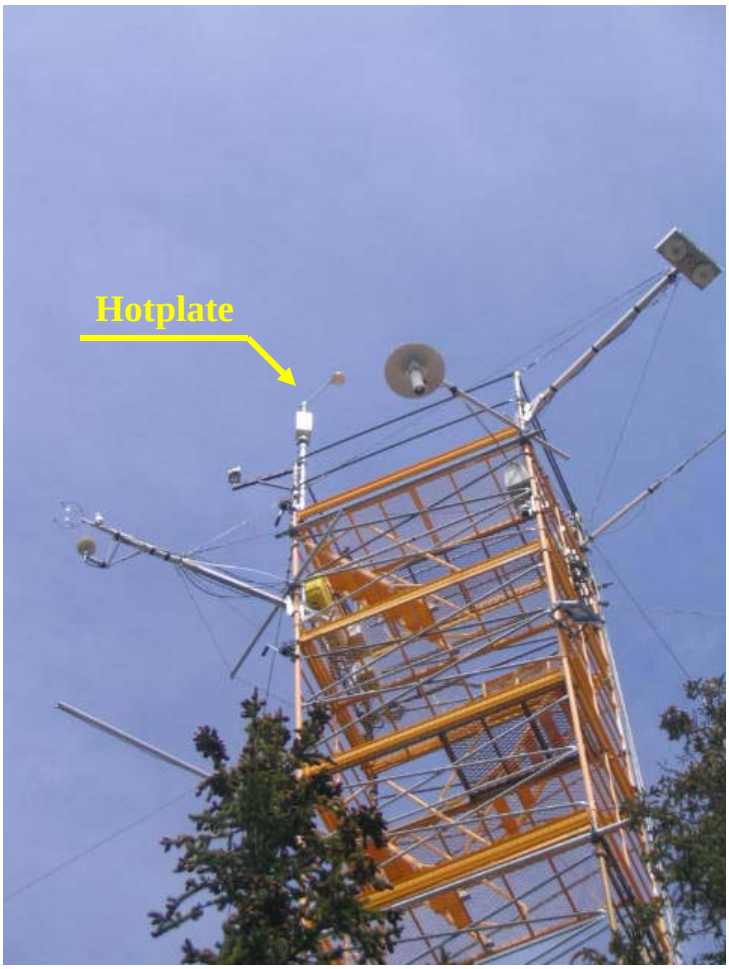

Figure 3.4 – 30 m AmeriFlux tower at GLEES, Wyoming. The Hotplate is seen is the left corner of the top of the tower.

3.4 National Atmospheric Deposition Program

At the NADP site precipitation is sampled by the NADP-sample-volume sensor and is accumulated by the NADP-gauge sensor; the duration of the sampling is one week. The site is visited weekly by a technician, who removes the sample volume and installs a new one into the apparatus. The chemical composition of the precipitation sample is measured at a central laboratory. The data set archived by the NADP includes the volume of water recovered from the sample volume, the chemical composition of the sample and the time-integrated precipitation reported by the gauge. The accumulation resolution of the NADP-gauge is 0.13 mm (Table 1.1; Chapter I); weekly samples having precipitation amounts less than this are eliminated from the analysis conducted here.

The two NADP measurement sensors are shown in Figure 3.5; on the left is the sample volume sensor and on the right is Alter-shielded Belfort gauge. At the same height as the gauge orifice is the Alter shield. The shield slows the air, and the snow particles it carries, and also minimizes the upward deflection of the particles over the gauge opening. The latter process is known to cause underestimation of the precipitation rate, a phenomenon commonly called “gauge undercatch”. In spite of the Alter shield, the precipitation catch efficiency is known to be a decreasing function of wind speed with a 50% catch efficiency occurring at a wind speed of approximately 5 m/s (Goodison, 1978). This bias is not accounted by NADP.

Figure 3.5 also shows the sample volume and its moisture sensor. The sensor faces upwards and is heated by electrical power supplied by a solar-charged power system. When precipitation impinges on the moisture sensor, an "open" signal causes the cover on the sample volume to open. Conversely, if the moisture sensor is not exposed to precipitation a "close" signal is sent to the cover of the sample volume, causing it to close.

3.5 National Resource Conservation Service – SNOTEL

The measurement sensor at SNOTEL site is shown in Figure 3.6. Included are the snow pillow with an area of two square meters and an Alter-shielded precipitation gauge. Two transducers (one for the pillow and one for the gauge) monitor the pressure of fluid (antifreeze) contained in the sensor. This pressure is used to evaluate the mass of the snow that overlays the pillow (Serreze et al., 1999) and the amount of precipitation that has fallen into the SNOTEL gauge. For the SNOTEL sensors operated at the Brooklyn Lake site the time resolution is 3600 s and the precipitation resolution is 2.5 mm (Table 1.1; Chapter I). The SNOTEL precipitation gauge is 5-m tall and its diameter 30 cm as seen in Figure 3.6. The accumulated mass of the snowpack, evaluated on April 1 and reported as a snow water equivalent (SWE) depth, is used to forecast the amount of water available for summertime streamflow (Schaefer and Paetzold, 2000).

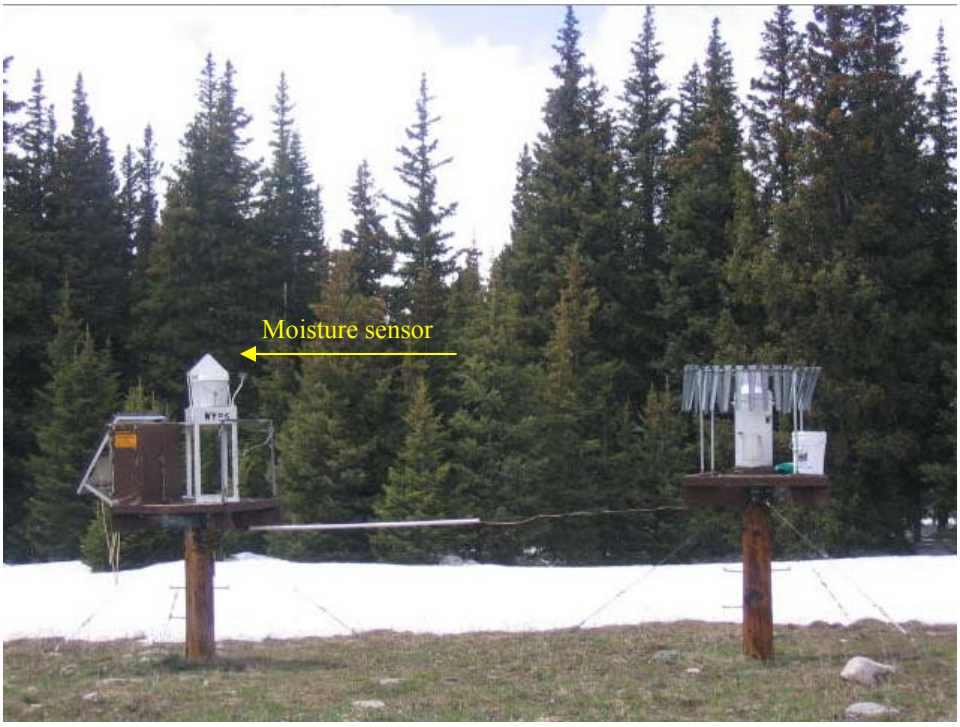

Figure 3.5 – Brooklyn Lake NADP site located at the Glacier Lake Ecosystem Experiments Site (GLEES) in the Medicine Bow Mountains of southeastern Wyoming. On the left is the sample volume sensor and on the right the Alter-shielded Belfort precipitation gauge. (Picture is taken 20070521)

Figure 3.6 - Snow pillow and the Alter-shielded gauge sensors at SNOTEL. The pillow measures the snow water equivalent of the wintertime snowpack.

3.6 Vaisala Rain Gauge

The Vaisala Rain Gauge (VRG101, hereafter referred to as the VRG) at the GLEES site is operated by the National Center for Atmospheric Science (NCAR). Figure 3.7 shows the gauge and its 2 m support tower. The gauge orifice is heated with an electrical resistance heater which was connected to line power when the temperature was less than 2 ^{o}C (Dan Breed, National Center for Atmospheric Science, private communication). The orifice heating system was not available for the 2007 field season but was installed prior to the 2008 field season. The VRG has a deep design which minimizes wind-induced loss of sample mass due to either evaporation or wind-resuspension. The time resolution of the VRG is 300 s (in 2008 it was 60 s) and the accumulation resolution is 0.1 mm/hr (Table 1.1, Chapter I).

Figure 3.7 - Vaisala Rain Gauge (right) operated by NCAR at the GLEES site during 2007 and 2008.

3.7 Vaisala Weather Transmitter - WXT510

The Vaisala Weather transmitter WXT510 is shown in Figure 3.8 (hereafter it is referred to as the Vaisala). The Vaisala provides measurements of wind speed and direction, temperature, relative humidity and pressure. The Vaisala wind sensor is an ultrasonic anemometer; it derives the wind speed and direction by measuring the delay between ultrasound transmission and detection. The Vaisala was operated on top of the AmeriFlux tower, about 1 m from the Hotplate.

3.7.a Wind Speed Comparison

The Hotplate wind speed is derived in the YES Hotplate Algorithm, which is proprietary (Section 2.4). Figure 3.9 is a scatterplot of Hotplate reference plate power versus Hotplate-derived wind speed. The figure shows two selected time intervals, Case #7, which is relatively cold, and Case #14, which is warmer. Both of these cases are described in greater detail in Table 2.3. Figure 3.9 demonstrates that the Hotplate wind speed does vary with reference plate power, as was suspected in Section 2.4; however, the Figure also suggests that the relationship between reference plate power and wind speed is temperature dependent. The temperature-dependence is consistent with the discussion in Hallett et al. (2006).

Figure 3.10 shows the Hotplate and Vaisala wind speeds, for the same time intervals presented in Figure 3.9. The Hotplate points are values sampled every 120 s and the Vaisala points are averages. The averaging interval for a Vaisala point has a

duration equal to 120 s and ends at the time the Hotplate data is sampled. The 120 s used for the sampling, and the averaging, is an estimate of the time response of the Hotplate. Wolfe (2007) shows that the time required for the Hotplate to reach 50% of its steady-state response, symbolized as T_s in Figure 2.7 and reported as a response time in Table 1.1 (Chapter I), varies between 62 and 132 s depending on the duration of the proceeding inactivity interval. That result is for the output signal known as *php* , the precipitation rate reported by the YES Hotplate Algorithm. On the assumption that the averaging of the Hotplate's wind speed is the same as for *php* , a reasonable estimate for the averaging/sampling time is the 120 s applied in Figure 3.10.

A one-to-one comparison (Figure 3.10) shows Vaisala and Hotplate wind speeds scatter close to the one-to-one line for the Case #7 (wind speed ~5 m/s), and above the one-to-one line for the Case #14 (wind speed ~7 m/s). During the Case #14 time interval the averaged Vaisala wind speed exceeded the Hotplate values by ~2 m/s.

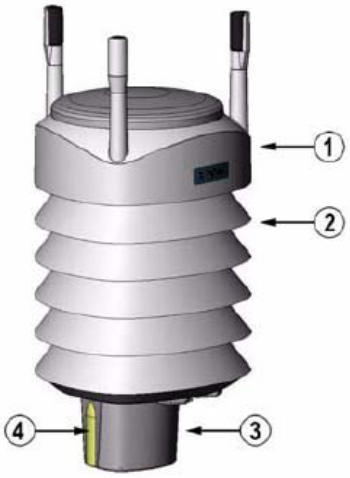

Figure 3.8 - Vaisala Weather Transmitter WXT510. 1 – Top of the transmitter, 2– Radiation shield, 3 – bottom of the transmitter, 4 – screw cover. It includes the following sensors: ultrasonic wind sensor (wind speed and direction), pressure, temperature and relative humidity.

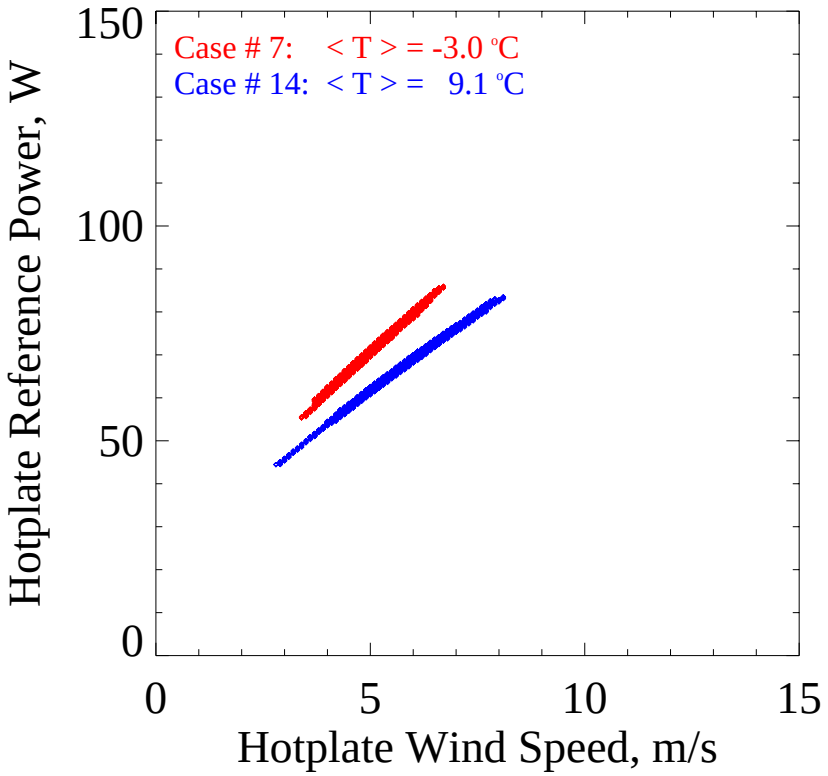

Figure 3.9 - The Hotplate reference plate power versus the Hotplate derived wind speed for the Cases #7 (20070413) and #14 (20070606).

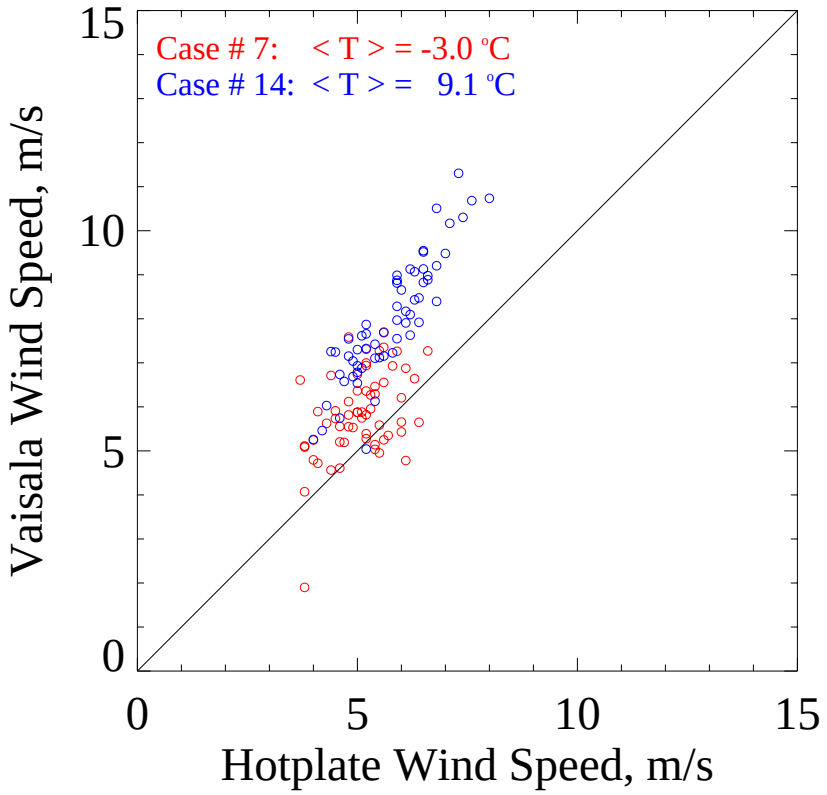

Figure 3.10 - Measurement of wind speed, reported by the Hotplate and Vaisala. Plotted are one-to-one comparison for Case #7 (20070413) and from Case #14 (20070606). The solid line is the one-to-one line.

3.8 NADP Precipitation Measurements

In this section, data from ten NADP sites are analyzed. Included in this group are the Brooklyn Lake NADP site, located at the GLEES, and the Nash Fork NADP site. The latter was abandoned in 1992 after six years of operation in the Medicine Bow Mountains. Other sites are located near Pinedale (Wyoming), Logan (Utah), at two different elevations in the Rocky Mountain National Park (Lock Vale and Beaver Meadows), and at two other pairs of high-low elevation sites in Colorado (the Niwot Saddle and Sugarloaf pair and the Sunlight Peak and Four Mile Park pair). A map of all NADP sites in the Rocky Mountain Region is shown in Figure 3.11. In the map, NADP sites discussed in this section are denoted by both their names and their elevations. In the following two sections, precipitation measurements made at the ten sites are compared. Those comparisons provide a motivation for the comparison of the GLEES precipitation measurements reported in Chapter IV.

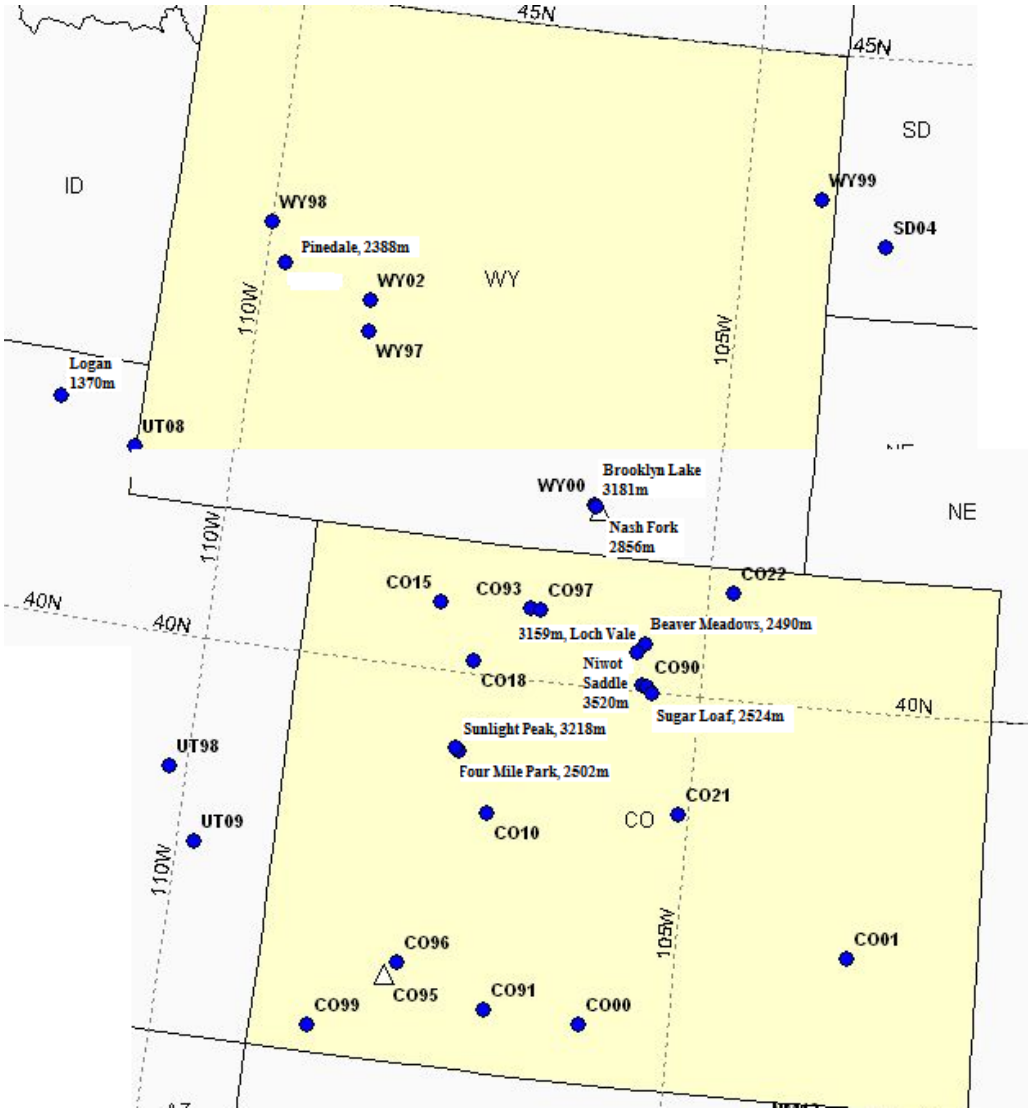

Figure 3.11 - A map of the NADP sites in Rocky Mountain Region. The sites selected for this thesis are indicated with the site name and its elevation. With the exception of Logan, UT, the sites are located above 2300 m.

3.8.a NADP Summertime Precipitation Measurements

This section compares summertime precipitation measurements made with the NADP systems (NADP-gauge and NADP-sample-volume). Examples of these weekly precipitation values are presented as a scatterplot for a low-elevation site (Logan), and for a high-elevation site (Brooklyn Lake), in Figure 3.12 and Figure 3.13, respectively. The data values are for the three summer months (June, July and August) and it is likely that the samples were collected as rain at Logan (occasionally as hail), while at Brooklyn Lake some of the samples may have been collected as snow. Not shown are data values with weekly precipitation less than 0.1 mm/week (Section 3.4). Since these plots were constructed using approximately 110 data points, out of a total of greater than 200 weeks (15 years of summertime weekly data at Brooklyn Lake and 23 years at Logan), it is apparent that a large number of the values had precipitation amounts less than 0.1 mm/week.

It is apparent that for Logan (Figure 3.12), and to a lesser degree for Brooklyn Lake (Figure 3.13), that the gauge and sample volume values are in good agreement. The next section will examine why a fraction of the Brooklyn Lake points lie above the one-to-one line.

The best-fit lines seen in Figures 3.12 and 3.13 have a slope which is very close to unity. These values are presented in Table 3.1 (see JJA slopes) with their statistical error. With the exception of four sites, all located at elevations greater than 2900 m, these slopes are statistically indistinguishable from unity. It is concluded that

for summertime precipitation measurements made at the sites lower than 2900 m, and for one site higher than 2900 m (Sunlight Peak), the NADP measurements are in good agreement. It is thought that that a factor contributing to JJA slopes slightly greater than unity is the occurrence of summertime snow at the high-elevation sites. This conjecture is discussed below.

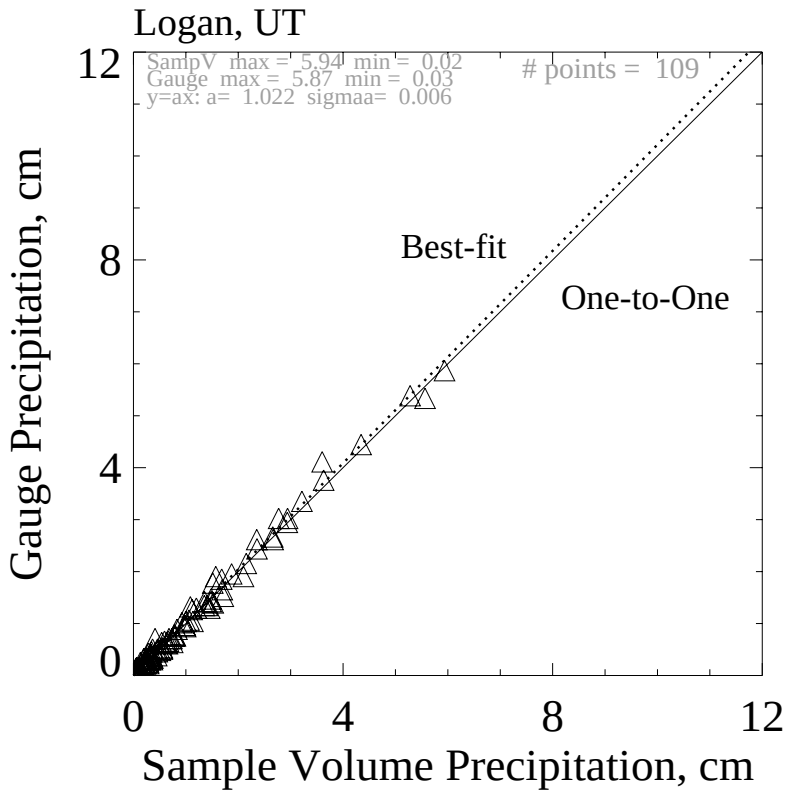

Figure 3.12 - Comparison of weekly precipitation from two sensors (gauge and sample volume) operated at Logan NADP site. The number of weeks that precipitation detected is shown in the right upper corner of each plot.

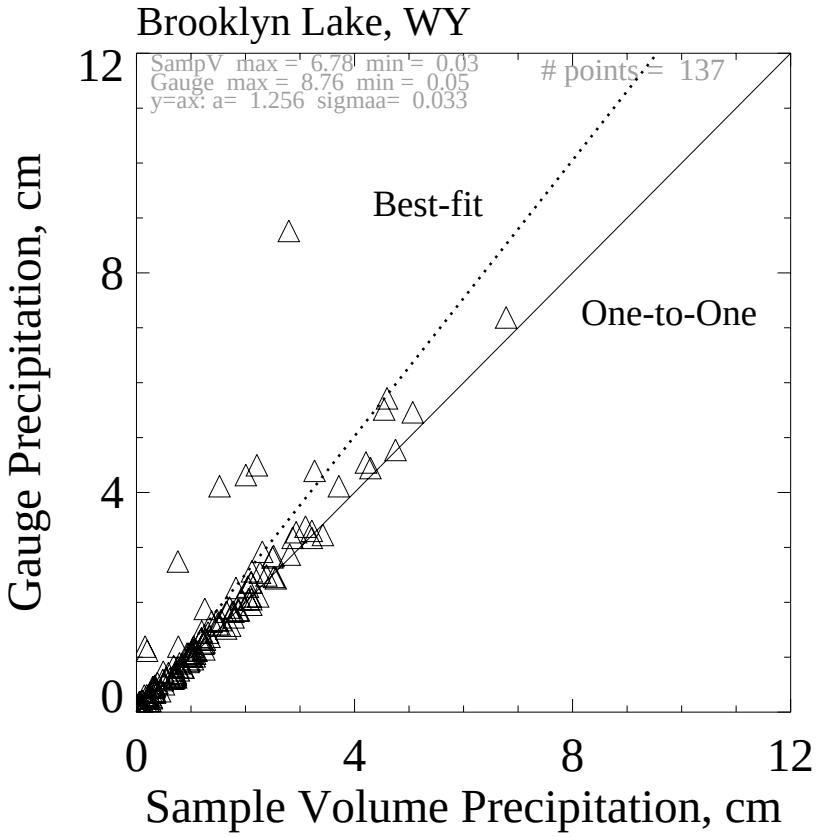

Figure 3.13 – As in Figure 3.12, but for Brooklyn Lake NADP site.

Table 3.1 Comparisons between NADP-gauge and the NADP-sample-volume sensors at ten sites at Rocky Mountain Region, 1980-2006

NADP Site Name	State	Elevation, m	JJA[1] slope	DJF[2] slope
Logan	UT	1370	1.0 ± 0.0	1.1 ± 0.0
Pinedale	WY	2388	1.0 ± 0.0	2.1 ± 0.1
Beaver Meadows	CO	2490	1.0 ± 0.0	1.2 ± 0.0
Four Mile Park	CO	2502	1.0 ± 0.0	1.4 ± 0.0
Sugarloaf	CO	2524	1.0 ± 0.0	1.3 ± 0.0
Nash Fork[3]	WY	2856	1.2 ± 0.0	3.1 ± 0.3
Loch Vale	CO	3159	1.2 ± 0.0	6.3 ± 0.6
Brooklyn Lake[4]	WY	3181	1.2 ± 0.0	7.2 ± 0.4
Sunlight Peak	CO	3218	1.0 ± 0.0	1.7 ± 0.0
Niwot Saddle	CO	3520	1.4 ± 0.0	12.1 ± 1.0

[1] – Slopes computed with data selected from the months June July and August, and the statistical error of the slope (following the "±")

[2] - Slopes computed with data selected from the months December, January and February, and the statistical error of the slope (following the "±")

[3] – Site abandoned in 1992

[4] – Operation started in 1992

3.8.b NADP Wintertime Precipitation Measurements

In this section the wintertime (December, January and February) precipitation measurements made at the ten selected NADP sites are presented and discussed. Figure 3.14 shows a scatterplot of gauge and sample volume precipitation measurements made during wintertime at the Logan site. Qualitatively, the scatter plot is similar to that for the summer months (Figure 3.12), but with a few points departing above the one-to-one line. These departures are reflected in the slope of the best-fit line (1.1) which is larger than the slope during summertime (1.0) (Table 3.1). As was suspected for Brooklyn Lake during summertime, the occurrence of snow may be a factor causing the DJF slope at Logan to be larger than unity.

The DJF slopes for the ten NADP sites are presented in Table 3.1 with their statistical error. For sites located below 2600 m the DJF slopes range from 1.1 to 2.1; however, for the high-elevation sites, the slopes range from 1.7 to 12.1. Wintertime data from two sites at altitudes > 2600 m are shown in Figures 3.15 and 3.16; these are the Niwot Saddle and Brooklyn Lake NADP sites, respectively. An obvious shift to larger values reported by the NADP-gauge is seen in both Figures.

Williams et al. (1998) analyzed data from the NADP-gauge at the Niwot Saddle NADP site, time integrated from October to May, and made a comparison to a reference gauge located two kilometers away. Their analysis showed that the measurements from the reference gauge, located in a small clearing, were a factor of two smaller than measurements made by the NADP-gauge which was located at the

top of the treeless ridge. The difference between the NADP-gauge and the reference gauge was also corroborated by a conditional sampling of the NADP-gauge measurements. Williams et al. (1998) accumulated NADP-gauge values over time intervals when the NADP-sample-volume was open and concluded that the conditionally-sampled accumulation was consistent with the reference. In other words, it appears that the NADP-gauge registers wind-resuspended ice particles that are not sampled by the reference gauge or by the NADP-sample-volume.

The result presented in Figure 3.15 is qualitatively consistent with the conclusion of Williams et al. (1998), i.e., during wintertime the Niwot Saddle NADP-gauge sensor reports much larger weekly precipitation amounts than the co-located NADP-sample-volume sensor. A similar result is seen for the Brooklyn Lake NADP system in Figure 3.16. Tentatively, it is concluded that the results presented in Figures 3.15 and 3.16 are influenced by four phenomena: 1)The NADP-gauge is open so it registers wind-resuspended ice particles whenever the conditions are favorable (wind, prior snowfall, etc.); 2) The moisture sensor does not signal the NADP-sample-volume to open during light snowfall, or during wind-resuspension events, especially if the wind speed is large enough to keep the snow particles (or resuspended ice particles) from adhering to an melting on the moisture sensor; 3) The NADP-sample-volume sensor is unshielded (Section 3.4) so it collects snow or wind-resuspended ice particles less efficiently than the Alter-shielded NADP-gauge; and 4) The sample collected in the NADP-sample-volume is lost via wind-resuspension.

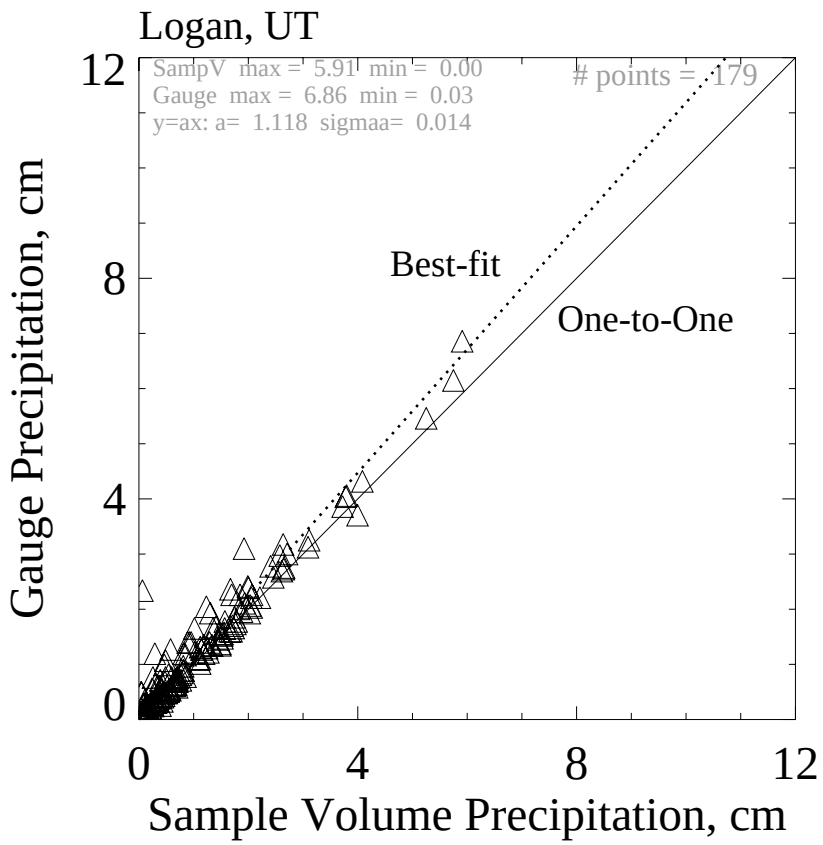

Figure 3.14 - Weekly precipitation from two sensors operated at the Logan NADP site (December, January and February). The number of weeks that precipitation was detected is shown in the upper-right corner of the plot.

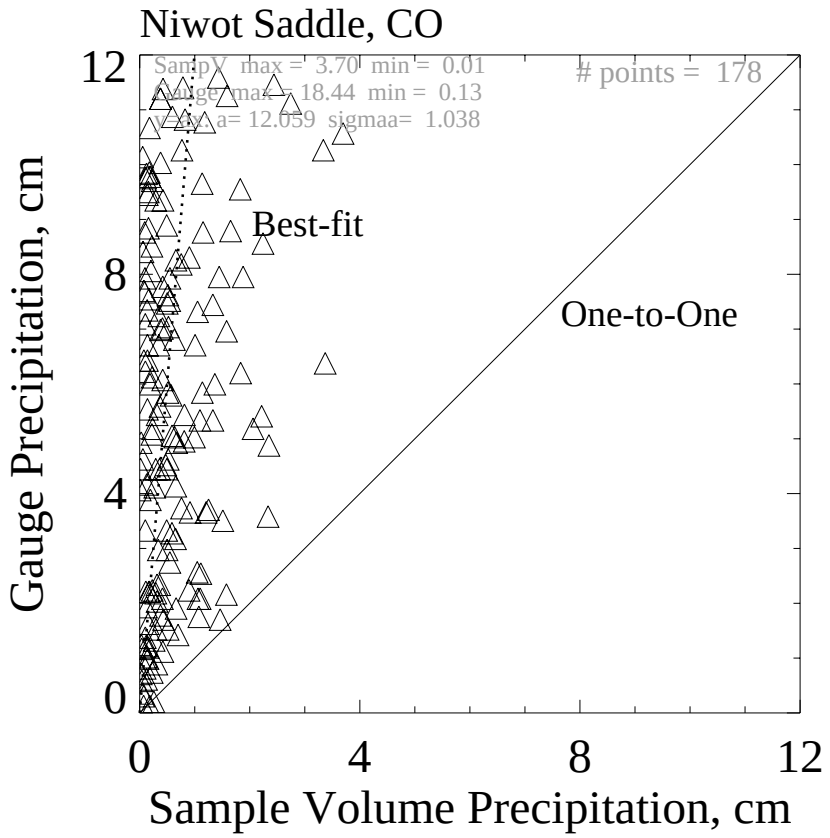

Figure 3.15 – As in Figure 3.14, but for Niwot Saddle NADP site.

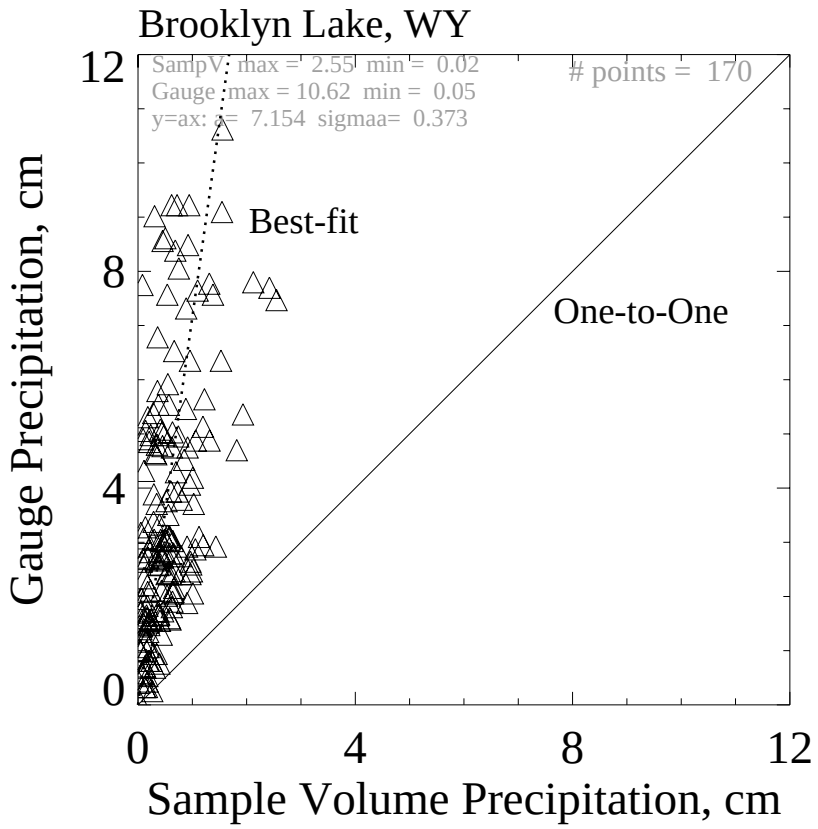

Figure 3.16 – As in Figure 3.14, but for Brooklyn Lake NADP site.

3.9 Summary

Precipitation measurements from ten NADP sites located in the Rocky Mountain Region of the western USA are analyzed. Four of the sites were located above 2600 m where temperatures are expected to be colder than at the relatively low elevation sites. Also, higher wind speeds are expected for the sites higher than 2600 m, compared to the low elevation sites. Data from two NADP precipitation sensors, the NADP-gauge and NADP-sample-volume, are compared. Overall the gauge measurements are larger than the sample volume measurements, with this difference is most evident during the wintertime when the gauge-to-sample-volume ratio is as large as 12. Likely causes for disparity bias are discussed. It is suspected that a dominating effect is the collection of wind-resuspended ice particles by the NADP-gauge. The wind-resuspended ice particles are thought to source from snow which fell locally, for example on the trees seen to the west of the NADP site in Figure 3.3. This conclusion is tentative because the moisture sensor used to signal the NADP-sample-volume, opening it during snowfall events, may not work optimally when wind prohibits the accumulation of snow (or wind-suspended ice particles) on the sensor surface. The latter phenomenon, the absence of an Alter shield on the NADP-sample-volume and the loss of material from the NADP-sample-volume are all thought to lead to precipitation underestimation by that sensor. Registration of wind-resuspended ice particles by the NADP-gauge is consistent with the work of Williams et al. (1998) who examined data from one of the ten sites reported on here. Data from

two high-elevation sites, Brooklyn Lake and Niwot Saddle, show that the gauge-to-sample volume ratio is largest for the Niwot Saddle site examined by Williams et al. This contrast is evident in the slopes of the lines plotted in Figures 3.15 and 3.16.

The conclusions discussed in this summary are tentative because of the coarse time-resolution of the NADP system and because the NADP data set does not include temperature or wind data. Measurements discussed in the following chapter do include precipitation, radiation and meteorology (temperature, wind speed and relative humidity). Because of this, and since the time-resolution of the other five precipitation sensors is much better than that of the NADP system, a more complete analysis of the inadvertent collection of wind-resuspended ice particles can be conducted.

CHAPTER IV: Comparisons of Six Measurement Techniques

4.1 Introduction

Chapter III provided an analysis of data from two of the six precipitation measurement sensors operated at the GLEES site. A large difference, as large as a factor of twelve during wintertime at the Niwot Saddle NADP site, is documented for the two NADP sensors. In Chapter III it is concluded that both NADP sensors are biased, and that the bias is positive for the NADP-gauge and negative for the NADP-sample-volume. Processes responsible for the bias are not adequately understood, in part because overestimation due to the inadvertent sampling of wind-resuspended ice particles can compensate wind-induced precipitation underestimation (Williams et al., 1996; Groisman et al., 1996; Williams et al., 1998; Yang et al., 2000; Sugiura et al., 2006). This work is the first to maintain a calibrated snow measurement system on a tower above a high-elevation forest canopy so that the suspected positive bias in surface-based snow measurement systems (other than the NADP-sample-volume) can be explored. This Chapter analyses precipitation data from six snow measurement sensors; results from two field seasons are discussed.

4.2 Measurement Availability

This section discusses measurement availability at the GLEES site during the winter and spring months of 2007 and 2008. Measurements from the two Brooklyn

Lake NADP systems and the Brooklyn Lake SNOTEL-gauge sensor are available for whole time period. Because it is influenced by snowpack melting, the Brooklyn Lake SNOTEL-pillow data is unreliable during the springtime. The dates of VRG and Hotplate measurement availability are presented in Table 4.1, where it is seen that the VRG was available for the winter and part of the spring of 2007. VRG availability was longer in 2008, but the VRG was not available during the early part of the winter 2008 season. The Hotplate availability dates are provided in fourth and fifth rows of Table 4.1.

Because of the late deployment of the Hotplate in 2007, the cold-season comparisons for that year (24-hour-averaged temperature < 1 ^{o}C) do not include the Hotplate measurements (Table 4.1). Also, a Hotplate/VRG warm-season comparison (24-hour-averaged temperature > 1 ^{o}C) is not possible for 2007. In spite of these limitations, the 2007 comparisons are useful because they bring together measurements from the NADP, SNOTEL and the VRG. The 2008 comparisons involve all six sensors, starting on 20080323 and encompassing both cold-season and warm-season conditions. The 24-hour-averaged temperatures at GLEES were derived using data archived by the AmeriFlux network (Section 3.3).

4.3 Cold-season and Warm-season Conditions

Time series of the snow water equivalent (SWE) accumulations are presented in Figures 4.1, 4.2 and 4.3. Figure 4.1 has measurements from five sensors (20061222 to 20070613), Figure 4.2 has measurements from five sensors (20080201

to 20080617) and Figure 4.3 has measurements from six sensors starting on the date the Hotplate became available in 2008 (20080323 to 20080603). These Figures are divided into intervals of cold-season and warm-season conditions separated by the first day the 24-hour-averaged temperature exceeded 1 ^{o}C (Table 4.1).

The intercomparisons were extended over both cold- and warm-season conditions so that temperature-dependent differences could be investigated. For example, Chapter III shows that the Brooklyn Lake NADP measurements are in agreement during June, July and August (mostly rain and temperatures generally greater than 0 ^{o}C) and that they strongly diverge for measurements made during December, January and February (mostly snow and temperatures generally less than 0 ^{o}C) (Figure 3.8). Those findings are extended here, and in addition, comparisons are made between the surface-based VRG and the tower-based Hotplate sensors.

Table 4.1 Dates for the 2007 and 2008 comparisons

Date	**2007**	**2008**
VRG available	December 22, 2006	February 01,2008
VRG unavailable	April 12	June 03
Hotplate available	April 12	March 23
Hotplate unavailable	June 22	June 14
First day the 24-hour-averaged temperature > 1 ^{o}C	March 12	April 15

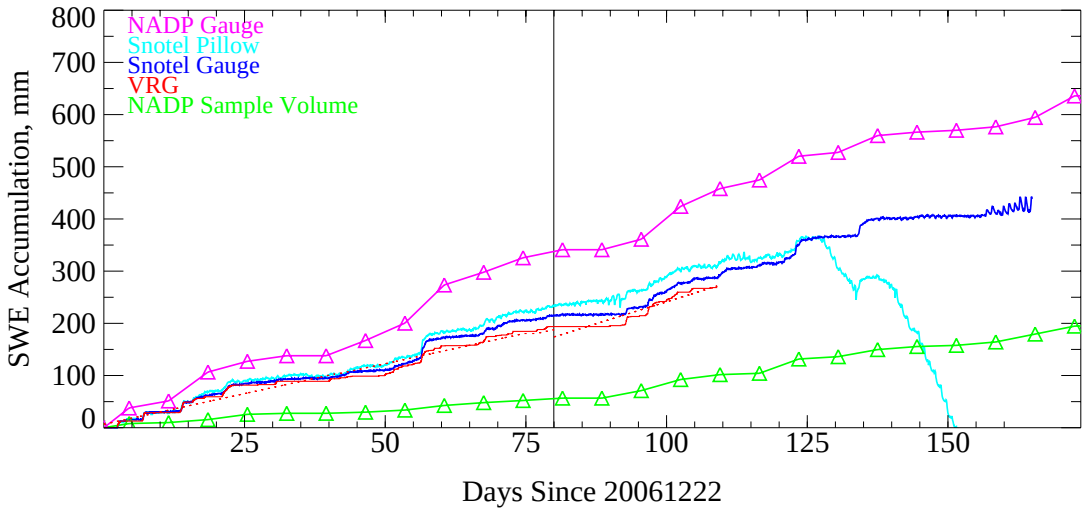

Figure 4.1 - Precipitation measurements at the GLEES site (five sensors, the Hotplate was unavailable) for winter and spring 2006/2007. The decrease in SNOTEL-pillow accumulation at day =125 is due to snowpack melting. The vertical line indicates the transition from cold- to warm-season conditions discussed in the text.

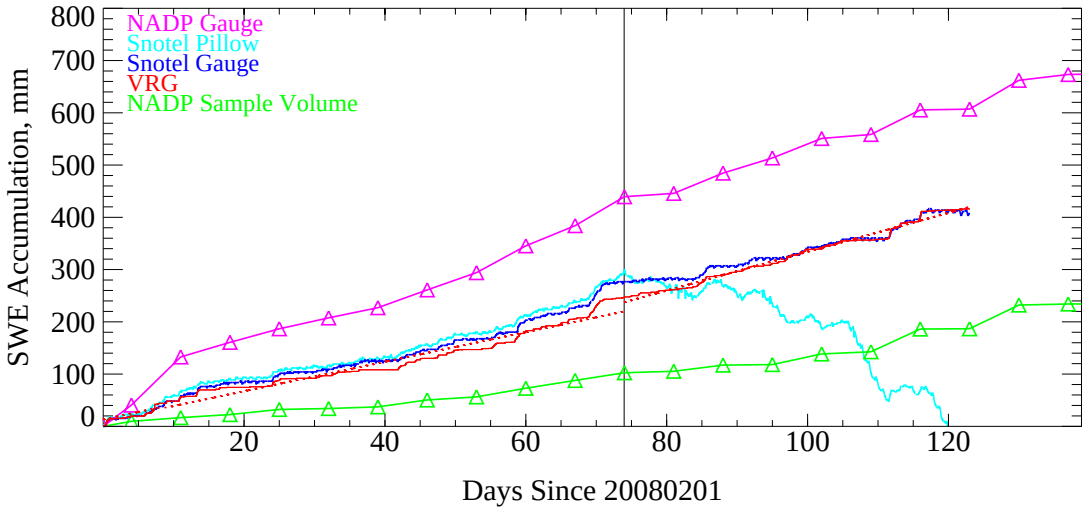

Figure 4.2 – Precipitation measurements at the GLEES site (five sensors, the Hotplate was unavailable) for winter and spring 2008. The decrease in SNOTEL-pillow accumulation at day =74 is due to snowpack melting. The vertical line indicates the transition from cold- to warm-season conditions discussed in the text.

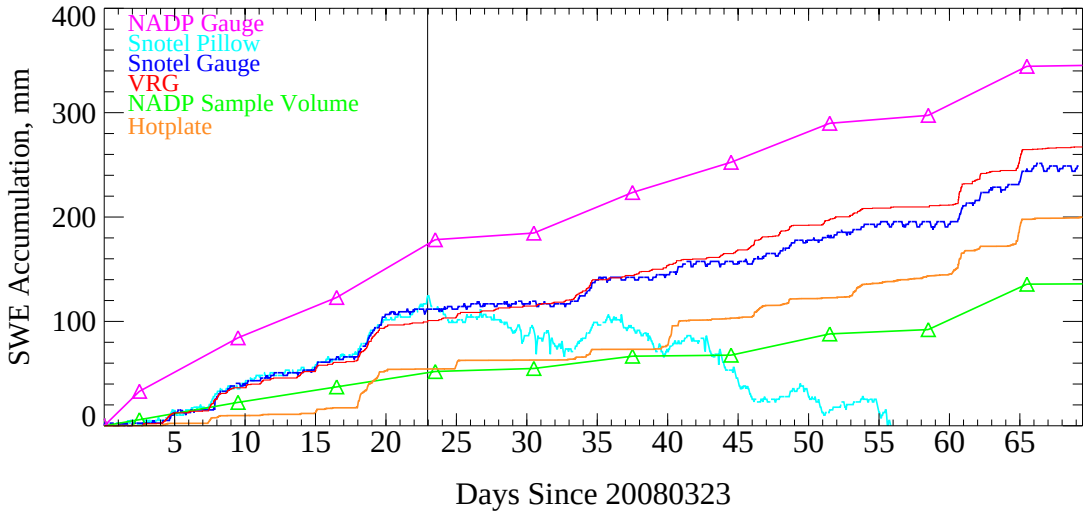

Figure 4.3 – Precipitation measurements at the GLEES site for subset of 2008 data that includes the Hotplate. The decrease in SNOTEL-pillow accumulation at day= 23 is due to snowpack melting. The vertical line indicates the transition from cold- to warm-season conditions discussed in the text.

4.4 Comparison Method

Table 1.1 (Chapter I) shows that the time resolution of the six sensors ranges between 1 s (Hotplate) and 604800 s (1 week; NADP). One way to intercompare the data set is to accumulate (Equation 1) measurements from the high-resolution sensors over the one-week integration period of the NADP sensors, and make the comparison in terms of these week-averaged values. Another is to average the measurements over the cold- and warm-season intervals, via a method described below. The latter approach was chosen for this work. Guiding this choice is the fact that interval-averaging incorporates a larger number of precipitation events than does week-averaging. Also, a practical advantage of interval-averaging is that the comparison is made between measurements separated into two objectively defined categories. In spite of the practicality, and the data smoothing provided by the selected approach, it can be criticized because the temperature criterion used to distinguish between cold- and warm-season conditions does not cleanly separate between precipitation events with snow (cold-season particles) and those with graupel and rain (warm-season particles). A clear distinction between precipitation particle phase (ice or liquid), and also between precipitation particle density (low density snow particles versus higher density graupel particles and high density rain particles) is desired because both factors (phase and particle density) are thought to influence what a particular precipitation sensor reports. These influences include particle catch efficiency

(Goodison 1978, Groisman et al., 1996), wind-resuspension of surface-deposited ice particles (Williams et al., 1998), redistribution of snow from the tree canopy to adjacent openings (Hoover and Leaf, 1967), and the opening of the NADP-sample-volume (Section 3.4).

For the interval-average comparisons an average precipitation rate was derived by fitting the time-integrated precipitation rate (i.e., the SWE accumulation) to a linear equation of the form

$$A = \langle PR \rangle \cdot t + b \qquad (13)$$

Here "A" is the SWE accumulation, "t" is time, "b" (the fitted intercept) is the accumulation at the start of the interval and $\langle PR \rangle$ (the fitted slope) is an interval-averaged precipitation rate.

Figure 4.4 shows Hotplate and VRG accumulations selected from Figure 4.3 (solid lines) and fit lines for the cold-season and warm-season conditions (dashed lines). Plotted on the abscissa is the number of days since the start of the cold-season comparison. When fitting the warm-season data the value of "b" (Equation 13) represents the accumulation, predicted by the fit model, at the start of the warm-season interval (day=23).

Values of the cold- and warm-season interval-averaged precipitation rates ($\langle PR \rangle$ in Equation 13) are presented in Table 4.2. It is apparent that the 2008 warm-season rates are in good agreement (25.4 and 26.0 mm/week, for the Hotplate and VRG, respectively) and that the cold-season rates are significantly larger for the

VRG. Further discussion of the Hotplate/VRG comparison, and the other comparisons, is provided in the following sections of this Chapter. A basis for those comparisons is the relative departure of the average precipitation rate. This is symbolized as RD_i and formulated as

$$RD_i = \frac{\langle PR_i \rangle - \langle PR_o \rangle}{\langle PR_o \rangle} \times 100\% \qquad (14)$$

Here, $\langle PR_i \rangle$ is an average precipitation rate and $\langle PR_o \rangle$ is the average precipitation rate from the SNOTEL-gauge, which was taken to be a reference. Table 4.3 presents the departures.

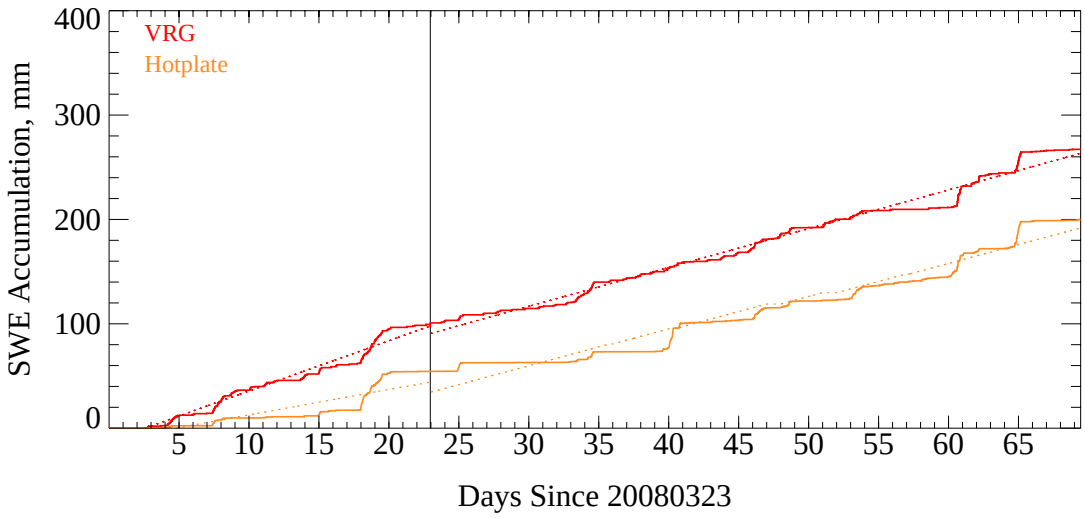

Figure 4.4 – SWE accumulations from the VRG and Hotplate in 2008. The vertical line at day=23 (20080415) indicates first occurrence of the 24-hour-averaged-temperature >1 ^{o}C. The dotted lines are cold-season and warm-season fits of the accumulation (Equation 13).

Table 4.2 Interval-averaged precipitation rates (fitted slopes in Equation 13) for precipitation sensors at GLEES during the cold seasons, and warm seasons, of 2007 and 2008.

Sensor	2007		2008		2008[1]	
	Cold (20061222-20070312) (7-week) mm/week	Warm (20070312-20070410) (4-week) mm/week	Cold (20080201-20080415) (11-week) mm/week	Warm (20080415-20080603) (7-week) mm/week	Cold (20080323-20080415) (3-week) mm/week	Warm (20080415-20080603) (7-week) mm/week
Hotplate	NA	NA	NA	-	17.2	25.4
VRG	16.4	23.5	19.8	26.0	32.7	26.0
SNOTEL - pillow	19.8	22.7	22.8	NA	36.4	NA
SNOTEL - gauge	18.2	22.0	22.2	21.6	36.8	21.6
NADP - gauge	28.2	31.7	33.3	28.2	45.0	28.2
NADP-sample-volume	4.3	12.6	8.0	12.4	15.7	12.4

[1] subset of the 2008 data which includes the Hotplate

NA ≡ not available

Table 4.3 As in Table 4.2, but expressed as a departure from the SNOTEL-gauge sensor (Equation 14)

Sensor	2007		2008		2008[1]	
	Cold (20061222-20070312) (7-week) mm/week	Warm (20070312-20070410) (4-week) mm/week	Cold (20080201-20080415) (11-week) mm/week	Warm (20080415-20080603) (7-week) mm/week	Cold (20080323-20080415) (3-week) mm/week	Warm (20080415-20080603) (7-week) mm/week
Hotplate	NA	NA	NA	-	-53	+18
VRG	-10	+7	-11	+20	-11	+20
SNOTEL - pillow	+9	+3	+3	NA	-1	NA
SNOTEL - gauge	-	-	-	-	-	-
NADP – gauge	+55	+44	+49	+30	+22	+30
NADP-sample-volume	-76	-43	-64	-42	-57	-42

[1] subset of the 2008 data which includes the Hotplate

NA ≡ not available

4.5 Comparisons of Six Measurement Techniques

4.5.a The Cold-Season

The reference sensor (SNOTEL-gauge) measured 18.2 mm/week and 22.2 mm/week for the cold-seasons of 2007 and 2008, respectively. These values were used to derive cold-season departures for the two NADP sensors, the SNOTEL-pillow and the VRG (Table 4.3). A discussion of the Hotplate departures is provided in Section 4.6.

Table 4.3 shows that the departures range from -76% to +55% in the two cold-seasons and that these extremes come from the NADP system with the NADP-gauge consistently overestimating ($49\% \leq RD_i \leq 55\%$) and the NADP-sample-volume consistently underestimating ($-76\% \leq RD_i \leq -64\%$). The signs of these departures are consistent with results presented in Section 3.8. Furthermore, Table 4.2 shows that the ratios of the cold-season interval-averaged precipitation rates (NADP-gauge to NADP-sample-volume) are 6.6 and 4.2 in 2007 and 2008, respectively. With caveats, these ratios can be compared to the analysis of 15 years of Brooklyn Lake NADP data presented in Section 3.8.b. That analysis showed that the gauge-to-sample volume ratio is 7.2 for measurements made during the months of December, January and February (Table 3.1). It is important to recall that the cold-season definition used here (Table 4.1) encompasses the month of March (in 2007) and the months of March and April (in 2008). Therefore, the gauge/sample-volume ratios

from Table 4.2 may be shifted toward smaller values by the occurrence of warm-season precipitation particles (rain and graupel) averaged together with the occurrence of cold-season particles, i.e., snow.

Compared to NADP the magnitude of the cold-season departure is smaller for the SNOTEL-pillow and the VRG (Table 4.3). Also, these sensors depart in opposite directions with the SNOTEL-pillow positive, and the VRG negative. The positive departures for the SNOTEL-pillow ($3\% \leq RD_i \leq 9\%$) may be indicative of the pillow sensor, located on the surface, registering more of the wind-resuspended ice-particles compared to the SNOTEL-gauge which has an orifice located 5 m higher (Section 3.3; Chapter III). The negative departures for the VRG are between -10 and -11%. The sign of this departure may be due to the fact that the VRG is unshielded and thus prone to undercatch relative to the Alter-shielded SNOTEL-gauge (Section 3.5).

Summarizing, the good agreement among SNOTEL-pillow, SNOTEL-gauge and VRG, with departure magnitudes less than 12%, suggests that the NADP-gauge data is biased by as much as +55% during the cold-seasons of 2007 and 2008. In addition, it appears that the NADP-sample-volume sensor is biased negative by as much as -76%.

4.5.b The Warm-Season

Values of the interval-averaged precipitation rates, and their departures, for warm-season measurements are shown in third and fifth column of Tables 4.2 and

4.3. As expected from the analysis of 15 years of NADP data in Section 3.8.b, the warm-season intercomparisons are more consistent than the cold-season intercomparisons. Generally better agreement among the warm-season NADP data set (NADP-gauge and NADP-sample-volume) is attributed to the larger density of the particles in the warm season (graupel and rain) compared to particle density during the cold season (snow). Larger particle density means that the particle trajectory is less affected by the wind (Strangeways, 2007; Sevruk, 1996), and because there is greater cohesion among the snow particles at 0 ^{o}C compared to colder temperatures (Schmidt, 1980). The latter process is thought to limit wind-resuspension of deposited snow particles as their temperature approaches the melting point. Another expectation for warm-season conditions is that the particles depositing on the NADP moisture sensor are more likely to be retained on the sensor surface, where they can melt and thus cause the moisture sensor to signal the NADP-sample-volume to open.

The ratio of precipitation rates from the NADP-gauge and the NADP-sample-volume is approximately 2.5 for the warm-season results presented in Table 4.2. This ratio is higher than the summertime NADP-gauge to NADP-sample-volume ratios discussed in Section 3.8.a, but it must be remembered that the Chapter III analysis considered measurements from June, July and August while the present analysis is for March, April, May and June. Both this analysis, and that in Chapter III, are consistent with the observation of snow at GLEES in late spring and early summer , and with the fact that snow is more mobile (compared to graupel or rain) and thus more prone to wind resuspension subsequent to a precipitation event. Table 4.3 also

demonstrates that the VRG departure changed sign between the cold season (RD_i ~-10%) and the warm season (RD_i ~+10%).

4.6 Comparison of Surface-based and Tower-based Measurements

This section compares the Hotplate and VRG measurements. It is recalled that these sensors were separated by 70 m, in the horizontal and 30 m in the vertical (Section 3.3). Also, the Hotplate was operated on the top of the AmeriFlux tower, approximately 15 m above the top of the forest canopy. Values of $\langle PR \rangle$ and RD_i, derived for the Hotplate, are presented in second rows of the Tables 4.2 and 4.3, respectively. The interval-averaged precipitation rates from the VRG and Hotplate are in good agreement during the warm-season, but, differ by a factor of two during the cold-season. This result is also evident in Figure 4.4. The next section investigates these findings, in particular, the sensitivity of the Hotplate $\langle PR \rangle$ to a parameter known as the "threshold". Determination of the default threshold, 0.8 mm/hr, is discussed in Section 2.11.

4.6.a Correction for Threshold

The Hotplate results in Table 4.2 were derived using the default threshold (0.8 mm/hr; Section 2.11). Section 2.11 discusses the threshold value in the context of the Wyoming Hotplate Algorithm and emphasizes that precipitation rates less than the threshold do not contribute to the Hotplate accumulation. In other words, instantaneous precipitation rates between 0.0 mm/hr and 0.8 mm/hr are set to 0.0 mm/hr. Hence, the values of the Hotplate $\langle PR \rangle$ reported in Table 4.2 are underestimated (negatively biased). The magnitude of this bias depends on the frequency of occurrence of precipitation values greater than 0.0 mm/hr and less than the threshold.

The Hotplate underestimation, resulting from the threshold, was investigated by applying a threshold of 0.0 mm/hr in the Wyoming Hotplate Algorithm. Justification for a lower threshold comes from an examination of all of the Wyoming Algorithm precipitation rate time series from the 2008 field season. While the threshold reduction is contrary to the recommendation of Chapter II it should be recalled that a decrease of the threshold is consistent with the fact that most of the data points in Figure 2.13 plot below the $\langle pw1 \rangle$=0 line.

The interval-averaged precipitation rates evaluated with the 0.0 mm/hr threshold are presented in second row of Table 4.4. As expected, the value of $\langle PR \rangle$ increased, from 17.2 mm/week (threshold = 0.8 mm/hr; Table 4.2) to 25.0 mm/week

(threshold = 0.0 mm/hr; Table 4.4) during the cold-season. Significant accumulation increases were documented for day = 4 (20080327), day=8 (20080331), day=11 (20080403), day=15 (20080407), day=16 (20080408) and day=17 (20080409). All of these days were associated with high relative humidities, ~80%, and the presence of clouds (indicated by the AmeriFlux radiation measurements). Hence, the increase of Hotplate $\langle PR \rangle$, seen in the comparison between Tables 4.2 and 4.4, is consistent with the prevailing meteorology.

Changing the threshold from 0.8 mm/hr to 0.0 mm/hr also increased the Hotplate $\langle PR \rangle$ during the warm-season. The increase is from 25.4 mm/week (threshold = 0.8 mm/hr; Table 4.2) to 51.2 mm/week (threshold = 0.0 mm/hr; Table 4.4). However, an examination of Hotplate time series data reveals that the increase of the warm-season $\langle PR \rangle$ is primarily due to a positive measurement bias. In Section 2.11 (Chapter II) there is discussion of why clear-sky nighttime conditions contribute a positive bias to the precipitation rate. This is evident from panels " a " and "b" of Figure 2.15 where a positive precipitation bias is evident between 0000 and 1400 UTC (Note: for the construction of Figure 2.15 no threshold condition was applied, so positive values of pwl accumulate positively and vice versa). The 10 mm accumulation bias evident in panel " b " of Figure 2.15 (day=56, 20080517) repeated over the next three days (through day=59, 20080520) and the time-integrated bias is ~60 mm. Comparable Hotplate accumulation biases, also attributable to having the

threshold set to 0.0 mm/hr, were documented for other multiday subsets of the warm-season interval.

The analyses presented in this section demonstrate that the value of the Hotplate interval-averaged precipitation rate is sensitive to the value used for the threshold. The default value of the threshold led to an underestimation of the Hotplate $\langle PR \rangle$ during the 2008 cold season. It is concluded that the threshold 0.0 mm/hr is more appropriate for 2008 cold-season conditions. This result is contrary to the recommendation of Chapter II, where the Wyoming Hotplate Algorithm is described in detail, but is justified by an examination of the 2008 time series data. It is also demonstrated that the 0.0 mm/hr threshold leads to a positive precipitation bias at nighttime during the 2008 warm season.

Table 4.4 As in Table 4.2, but with the Hotplate interval-averaged precipitation rate derived using a 0.0 mm/hr threshold.

Sensor	2008	
	Cold-season (20080323- 20080415) (3-week) mm/week	Warm-season (20080415- 20080603) (7-week) mm/week
Hotplate	25.0	51.2
VRG	32.7	26.0

4.6.b Snow Wind-Resuspension

Throughout the thesis there has been speculation that data from some surface-based snow measurement sensors (e.g., the NADP-gauge) are positively biased by the inadvertent sampling of wind-resuspended ice particles. Here the focus shifts to the surface-based VRG measurements made at GLEES during the 2008 cold-season, and to the possibility that those measurements are biased by the collection of wind-resuspended ice particles. The primary evidence for this phenomenon is that the VRG cold-season interval-averaged precipitation is larger than that from the Hotplate (Table 4.2). Furthermore, the previous section shows that the VRG's cold-season averaged precipitation rate remains larger than the Hotplate's even after correcting for a suspected overestimation of the precipitation rate threshold (cf., Tables 4.2 and 4.4).

This investigation started with an examination of time series data from all 23 of the cold-season days, including VRG precipitation, radiation and relative humidity measurements from AmeriFlux, and wind speed and temperature measurements from the Hotplate. Day=12 (20080404), day=22 (20080413) and day=23 (20080414) of cold season had conditions thought indicative of ice particle resuspension. Figures 4.5 and 4.6 show the latter two examples, both exhibiting clear-sky conditions throughout most of the 24-hour interval (panels "c" and "d"), relative humidity generally less than 60%, temperature between -7 and 7 ^{o}C, and increased wind speed or increased wind speed variability associated with the detection of "precipitation" by the VRG. The day=22 was preceded by a two-day snowstorm, which ended at 0400

UTC on day=21 and contributed 36 mm of SWE at the VRG. The 24-hour accumulation reported by the VRG was ~2 mm for both of these cases, and for the day=12 case it was less than 1 mm.

During the snowstorm that ended on day=21 the temperature was constant at -10 ^{o}C. The days 22 and 23, shown in Figures 4.5 and 4.6, were characterized by clear sky conditions, and by temperatures varying diurnally between -7 and +7 ^{o}C. Schmidt and Pomeroy (1990) show that the elasticity of a conifer branch increases with increasing temperatures, up to 0 ^{o}C, and that this elasticity increase can cause a tree branch to unload snowfall carried on its upper side. It is suspected that this temperature-dependent unloading process, and the wind documented on days 22 and 23, were both important for the ice particle resuspension thought to have occurred on those two days.

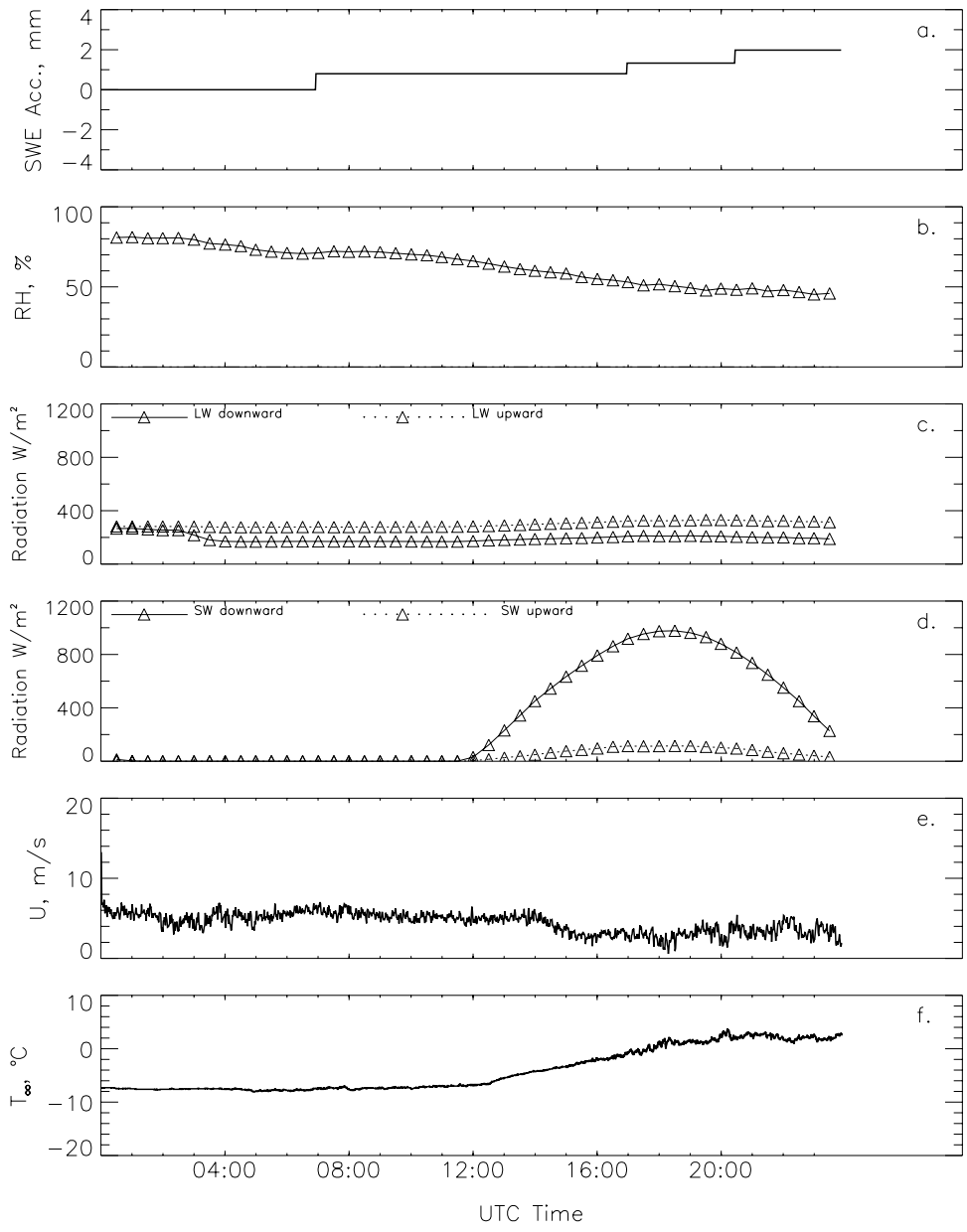

Figure 4.5 – Time series of VRG accumulation (panel “a”). The lower panels are time series of AmeriFlux measurements of radiation fluxes and Hotplate measurements of wind speed (derived) and ambient temperature. The time series starts on 0000UTC on 20080413.

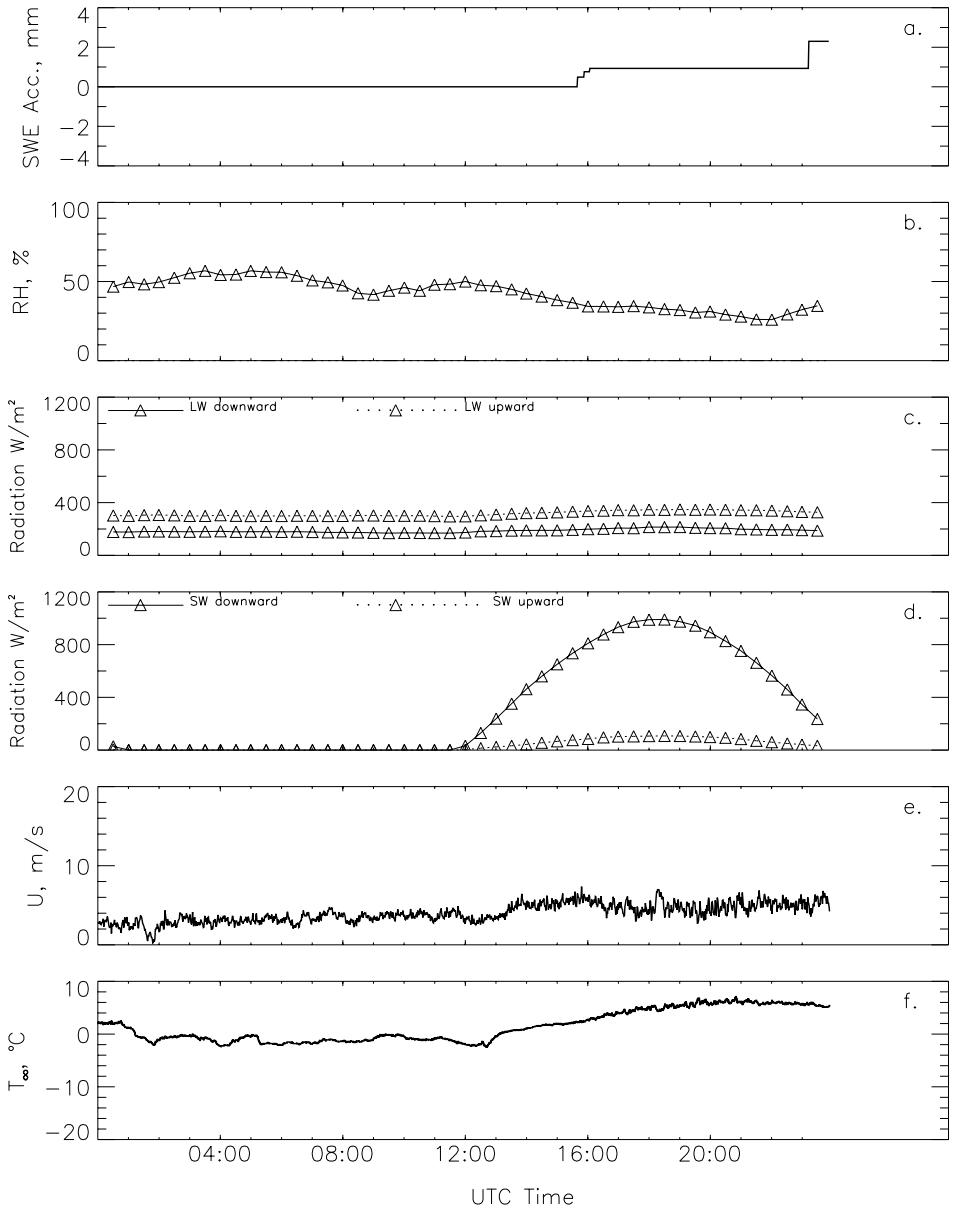

Figure 4.6 – As in Figure 4.5, but for 20080414.

4.7 Summary

Motivated by results from Chapter III, measurements from the six precipitation sensors were compared over the winters and springs of 2007 and 2008. Measurements were made within a forested site located in the Rocky Mountains of southeastern Wyoming. The study demonstrates that cold-season measurements made by a NADP-gauge are positively biased. The magnitude of the bias ranges between +49 and +55% when expressed relative to measurements made by the SNOTEL-gauge. Furthermore, cold-season snowfall measurements made with the Hotplate, operated on a 30 m tower, are smaller than measurements reported by four surface-based sensors (SNOTEL-gauge, SNOTEL-pillow, NADP-gauge and VRG). Because the Hotplate measurement was made above the forest canopy it is concluded that the surface-based sensors were biased by their inadvertent registration of wind-resuspended ice particles. This cold-season bias, for the surface-based sensors, may be as large as a factor of two.

CHAPTER V: Conclusions

5.1 Introduction

Data from six precipitation sensors operated at a high-elevation, forested site located in the Medicine Bow Mountains of southeastern Wyoming were presented and analyzed. A new sensor (Hotplate) was introduced and calibrated by the author of this thesis (Chapter II). The Hotplate was operated at GLEES with technical assistance from the staff of the Department of Atmospheric Science at the University of Wyoming.

5.2 Implications of this Research

The Wyoming Hotplate Algorithm, developed in this thesis, provides an accurate estimate of the precipitation rate. Chapter II describes calibrations which make improvements relative to the YES Hotplate Algorithm (i.e., Figures 2.4 and 2.5) and Chapter IV describes a comparison with the VRG sensor during warm-season conditions (i.e., Figure 4.4). Table 4.3 shows that the VRG and Hotplate agree within 2% for warm-season conditions during 2008.

Problems associated with the Hotplate are also documented. In Chapter II (Section 2.8) it is speculated that the Hotplate's radiation environment shifts both the calibration of $\dot{Q}_{der}$ and the wind speed (U). Radiation environment may also be a determinant of the of the residual precipitation rate documented for non-precipitating conditions. This is discussed in Sections 2.10 and 4.6.a, and the latter demonstrates

the sensitivity of the precipitation rate to the value of the threshold applied in Wyoming Algorithm. Ideally, a threshold should not be needed, but practically it is needed because the Equation 3 does not report $pwl=0$ for all possible wind, temperature and radiation conditions (Figure 2.13). While it is pleasing that lab-derived values for the three calibration constants (A_0, A_1 *and* A_2) does a reasonable job of describing the non-precipitating heat load of the Hotplate (Case #4, Section 2.10), there is clearly need for more frequent evaluation of those calibration constants and for improvement of the calibration procedure. For example, calibration of the non-precipitating heat load in a wind tunnel should improve on the two-point calibrations of this work. Also, there is need for a incorporating the effects of both longwave and shortwave radiation into Equation 4. Finally, it is demonstrated that the value of the calibration coefficient '*C*' depends on the degree of ventilation and on particle size. Neither of these results was expected but both appears to be consistent with the conjecture that the amount of energy, provided by the Hotplate and going into phase change, is smaller in the case of the larger ventilated drops (Section 2.7). The latter effect is attributed to an increased coupling between the large drops and the airflow (relative to small drops).

In addition to reporting on the calibration and processing of Hotplate data, this study has examined field measurements. Consistent with past work (Williams et al., 1998), it is shown that there is a disparity between precipitation measurements reported by a reference precipitation gauge and the NADP-gauge. At the Brooklyn

Lake NADP site the NADP-gauge had a departure that is between 49 and 55% larger than the reference. The departure documented here is smaller than that at the Niwot Saddle NADP site (+110%; Williams et al., 1998) but there are plenty of reasons to expect a difference. For example, the Niwot Saddle is treeless ridge, it is located 400 m higher than the Brooklyn Lake NADP, and the reference system used in this study is different from that used in Williams et al. It may be that the different departure at Brooklyn Lake and at the Niwot Saddle NADP sites can be explained in terms landscape, elevation or exposure to wind. This should be investigated because there is need for improved accuracy, of both precipitation and chemical deposition, in the Rocky Mountain Region.

NADP system data are widely used by ecologist to analyze precipitation chemistry in the Rocky Mountain Region (Baron and Denning, 1993; Burns, 2003; Nanus et al., 2003; Ramundo and Seastedt, 1990, Williams et al., 1996; and Williams et al., 1998). NADP sites at the highest elevation are relatively few in number, are difficult to maintain, and may not be representative the region-wide deposition. For example, at a windy high-elevation site the snow distribution pattern is sensitive to vegetation (Hiemstra, 1999) and at a high-latitude site topography is shown to be an important determinant of deposition (Pomeroy et al., 1995). These sensitivities depend on the spatial scale of the land-atmosphere interaction. It is unlikely that one factor will account for a deposition bias that results from the inadvertent sampling of wind-resuspended ice particles at the high-elevation NADP sites.

The most compelling implication of this work, but the least substantiated, is the evidence for positive bias in surface-based snow measurements due to wind-resuspension of ice particles. In a comparison of the cold-season data from 2008 the Hotplate measurements, which were tower-based, are smaller than measurements reported by four surface-based sensors (SNOTEL-gauge, SNOTEL-pillow, NADP-gauge and VRG). Because the Hotplate measurement was made above the forest canopy it is concluded that the surface-based sensors were biased by their inadvertent registration of wind-resuspended ice particles. This cold-season bias, for the surface-based sensors, may be as large as a factor of two. It should be emphasized that this was a preliminary study, yet the experimental design seems promising for future investigations.

5.3 Future research

For the future studies, it is recommended that the design be expanded to three Hotplate systems; one deployed on the AmeriFlux tower; a second surface-based in the center of the clearing, and the third surface-based at the edge of the clearing. The third Hotplate could be used to investigate snow unloading from conifer branches. It is speculated in Section 4.6.b that unloading does occur at the GLEES, in a manner consistent with the temperature-dependence of branch elasticity presented by Schmidt and Pomeroy (1990), and that the unloading process may augment the amount of ice available for resuspension by the wind. Finally, this proposed study should recognize that wintertime field work is demanding both on equipment and

personnel, and should place as much emphasis on instrument calibration as was the case in this study.

References

Baron, J. and A. S. Denning, 1993: The influence of Mountain meteorology on precipitation chemistry at low and high elevations of the Colorado Front Range. Atmospheric Environment, **27a** (15), 2337-2349.

Burns, D. A., 2003: Atmospheric nitrogen deposition in the Rocky Mountains of Colorado and southern Wyoming- a review and new analysis of past study results. Atmospheric Environment **37** (7), 921-932.

Goodison, B. E., 1978: Accuracy of Canadian snow gauge measurements. Journal of Applied Meteorology, **17**, 1542-1548.

Gordan, J. D., 1999: External quality-assurance results for the National Atmospheric Deposition Program/ National Trends network 1995-1996. US Geological Survey Water Resources Investigations Report 99-4072. pp69

Groisman, P. Y., D. R. Easterling, R. G. Quayle, V. S. Colubev, A. N. Krenke and A. Y. Mikailov, 1996: Reducing biases in estimates of precipitation over the United States: Phase 3 adjustments. Journal of Geophysical Research, **101** (D3), 7185-7195.

Hardy, J. P., R. E. Davis, R. Jordan, W. Ni, and C. E. Woodcock, 1998: Snow ablation modeling in a mature aspen stand of the boreal forest. Hydrological Processes, **12**, 1763-1778.

Hallett, J. and R.M. Rasmussen, 2006: Characterization of changing precipitation regimes. In: Preprints 18th Conference on Climate Variability and Change.

Hendsrom, N. R. and J. W. Pomeroy, 1998: Measurements and modeling of snow interception in the boreal forest. Hydrological Processes, **12**, 1611-1625.

Hiemstra C. A., 1999: Wind distribution of snow at tree-line, Medicine Bow Mountains, Wyoming. MS. Thesis, Department of Botany, University of Wyoming.

Hoover, M. D. and C. F. Leaf, 1967: Process and significance of interception in Colorado subalpine forest. Forest Hydrology, 213-224.

King, W. D., D. A. Parkin and R. J. Handsworth, 1978: A Hot-wire liquid water device having fully calculable response characteristics, Journal of Applied Meteorology, **17,** 1809-1813.

Landolt, S. D., S. M. Rasmussen, L. B. Jennifer, A. W. Tripp, 2008 : Snow gauge performance during the Denver blizzards of December, 2006. In: Preprint of 13th conference on aviation, range and Aerospace meteorology.

Legates, D. R. and DeLiberty, 1993: Precipitation measurement biases in the United States. Water Resources Bullettin, **29**, 855-861.

MacKay, M. D. and P. A. Bartlett, 2006: Estimating canopy snow unloading timescales from daily observations of albedo and precipitation. Geographical Research Letters, **33,** L19405.

Martner, B. E., and J. D. Marwitz, 1982: Wind characteristics in Southern Wyoming. Journal of Applied Meteorology, **21**, 1815-1827.

Mote, P. A., M. Clark and D. Lettenmaier, 2005: Declaining Mountain snowpack in Western North America. Bulletin American Meteorological Society, **86**, 39-49.

Musselman, R. C. 1994: The Glacier Lakes Ecosystem Experiments Site. Gen. Tech. Rep. RM-249. Fort Collins, CO: U.S. Department of Agriculture, Forest Service, Rocky Mountain Forest and Range Experiment Station, pp 94.

http://www.fs.fed.us/rm/pubs_rm/rm_gtr249.html

Nanus, L., D. H. Gampbell, G. P. Ingersoll, D. W. Clow and M. A. Mast, 2003: Atmospheric deposition maps for Rocky Mountains. Atmospheric Environment, **37**, 4881-4892.

Pomeroy, J. W., P. Marsh, H. G. Jones and T. D. Davies, 1995: Spatial distribution of snow chemical load at tundra-taiga transition. In: Preprints Biogeochemistry of Seasonally Snow-Covered Catchments, Boulder Symposium, IANS Publ. no. 228, 191-203.

Ramundo, R. A., and T. R. Seastedt, 1990: Site-specific underestimation of wetfall NH_4^+ using NADP data. Atmospheric Environment, **24a,** 3093-3095.

Rasmussen, R. M., J. Hallett, M. L. Tryhane, S. D. Landolt, R. Purcell, M. C. Beaubien, W. Q. Jeffries, F. Hage and J. Cole, 2005: The Hotplate Snowgauge. In: Preprints 15th Conference on Applied Climatology/13th Symposium on Meteorological Observations and Instrumentation, Savannah GA, 19-23, American Meteorological Society.

Rasmussen, R. M., J. Hallett, J. Cole, B. Myers, C. Masters, 1999, The estimation of snowfall rate using visibility. Journal of Applied Meteorology, **38**, 1542-1563.

Serreze, M. C., M. P Clark, and R. L. Armstrong, D. A. MacGinnis and R. S. Pulwarty, 1999: Characteristics of the western Untied States snowpack from snowpack telemetry (SNOTEL) data. Water Resources Research, **35 (7)**, 2145-2160.

Sevruk, B., 1996: Adjustment of tipping-bucket precipitation gauge measurements, Amospheric Research, **42,** 237-246.

Sugiura, K. D., T. Ohata, and D. Yang, 2006: Catch characteristics of precipitation gauges in high-latitude regions with high winds, Journal of Hydrometeorology, **7**, 984-994.

Schmidt, R. A. and J. W. Pomeroy, 1990: Bending of a conifer branch at subfreezing temperatures: Implications for snow interception. Canadian Journal of Forest Research, **20**, 1250-1253.

Schmidt, R. A., 1980: Threshold wind-speeds and elastic impact in snow transport. Journal of Glaciology, **26**(94), 453-467.

Schaefer, G. L. and R. F. Paetzold, 2000: SNOTEL (snowpack Telemetry) and SCAN (Soil Climate Analysis Network). In: Preprints "Automated Weather Stations for Applications in Agriculture and Water Resources Management: Current Use and Future Perspectives", Lincoln, NB.

Sommerfeld, R. A., 2004: Snow, Chapter 10, The Glacier Lakes Ecosystem Experiments Site, RM-GTR-249, 57-58.

http://www.fs.fed.us/rm/pubs_rm/rm_gtr249.html

Strangeways, I., 2007: Precipitation: Theory, measurement and distribution, Cambridge University press, pp 290.

Tryhane, M. L, S. D. Landolt, R. M. Rasmussen, 2005, Applications of the hotplate snow gauge. In: Preprints 15th Conference on Applied Climatology/13th

Symposium on Meteorological Observations and Instrumentation, Savannah GA, 19-23, American Meteorological Society.

Williams, M. W., J. S. Baron, N. Caine, R. A. Sommerfeld and R. Sanford JR., 1996: Nitrogen Saturation in the Rocky Mountains. Ecosystem Science Technology, **30,** 640-646

Williams, M. W., T. Bardsley and M. Rikkers, 1998: Overestimation of snow depth and inorganic nitrogen wetfall using NADP data, Niwot ridge, Colorado. Atmospheric Environment, **32** (22), 3827-3833.

Wolfe, J. P., 2007: Radar-estimated Upslope Snowfall Rates in Southeastern Wyoming. MS. Thesis, Department of Atmospheric Science, University of Wyoming.

Yang, D., D. L. Kane, L. D. Hinzman, B. E. Goodison, J. R. Metcalfe, Paul Y. T. Louie, G. H. Leavesley, D. G. Emerson and C. L. Hanson, 2000: An evaluation of the Wyoming gauge system for snowfall measurement. Water Resources Research, **36** (9), 2665-2677.

Appendix A

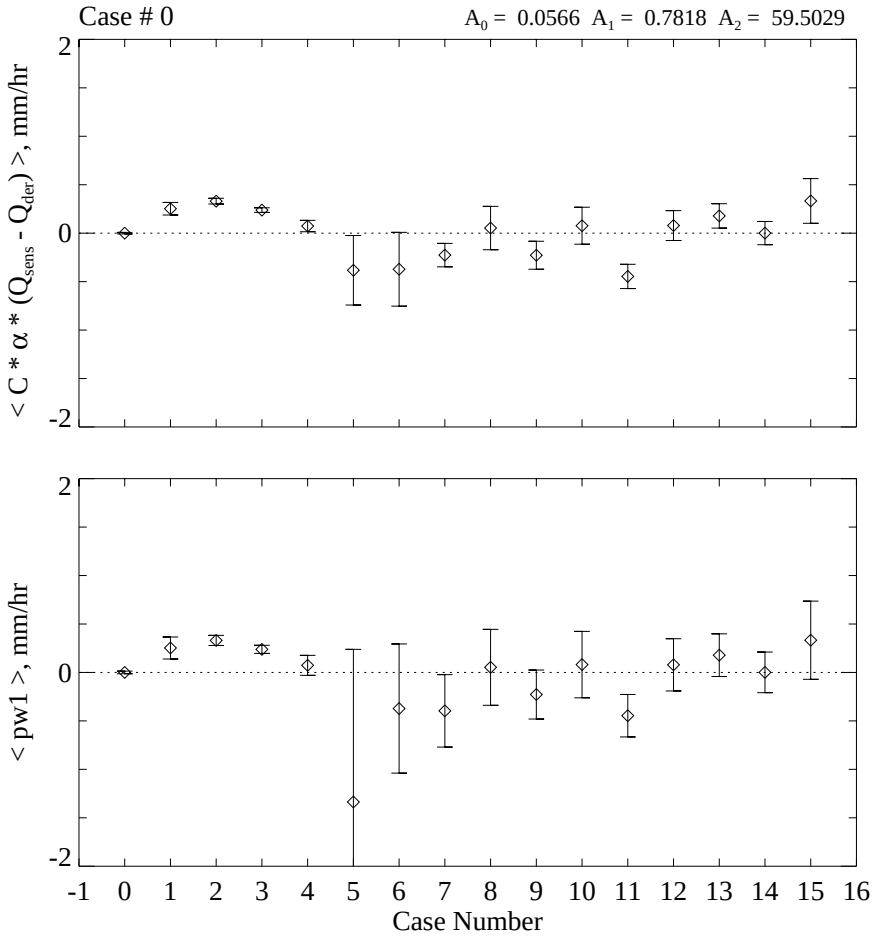

Figure 1 - Examination of the averages and variability from the selected time intervals. The calibration coefficient from Case #0 is applied to the selected time intervals. Top) Time average of $C \cdot \alpha \cdot (\dot{Q}_{sens} - \dot{Q}_{der})$. Bottom) Time average of the precipitation rate (Equation 3). Error limits represented by the average plus and minus one standard deviation.

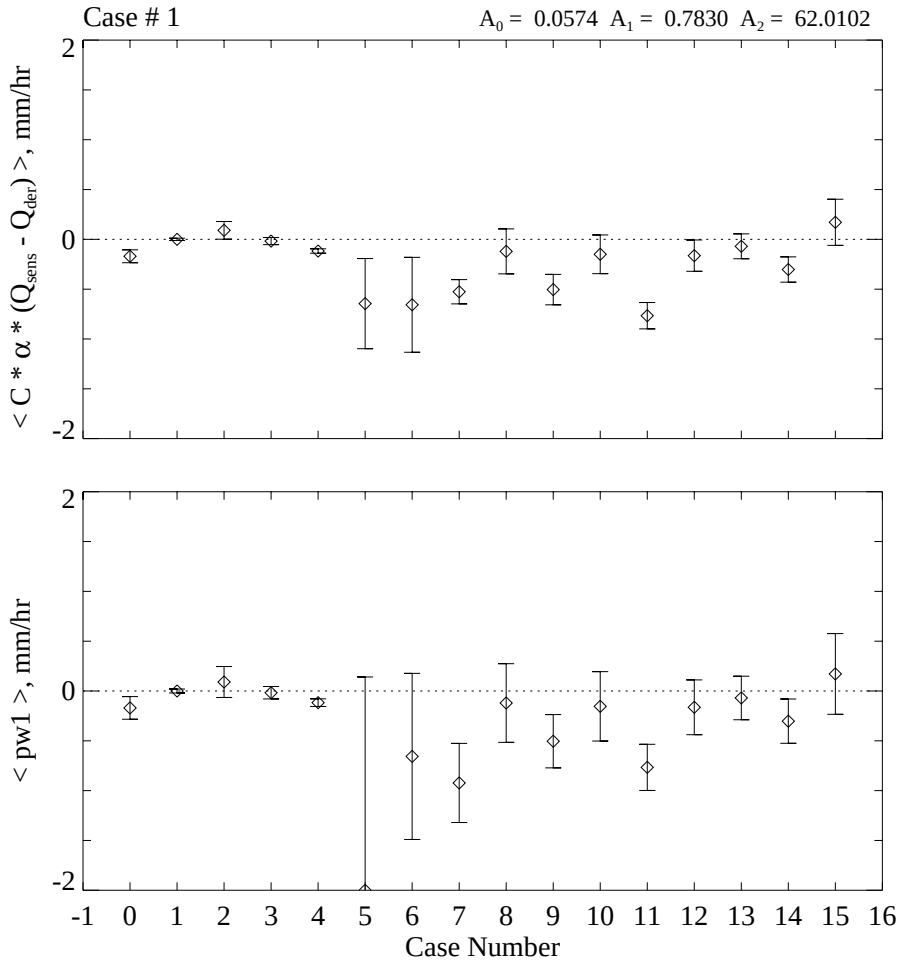

Figure 2 – As in Figure 1, but for the Case #1.

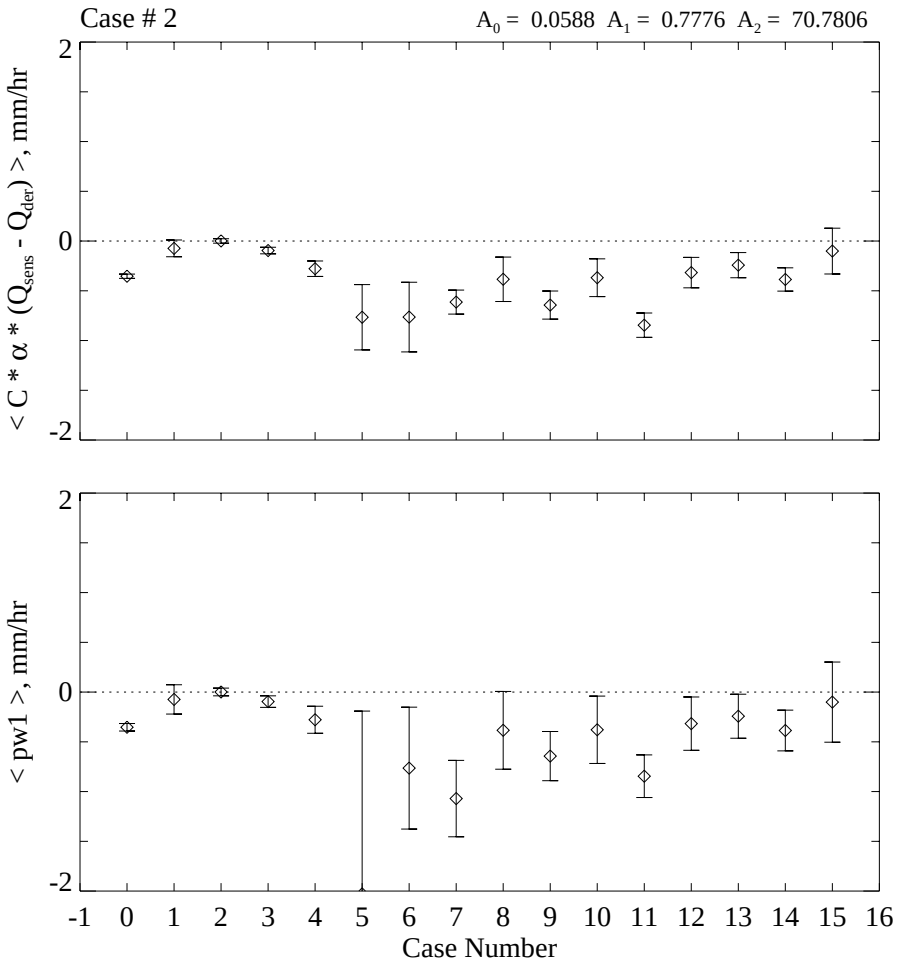

Figure 3 – As in Figure 1, but for the Case #2.

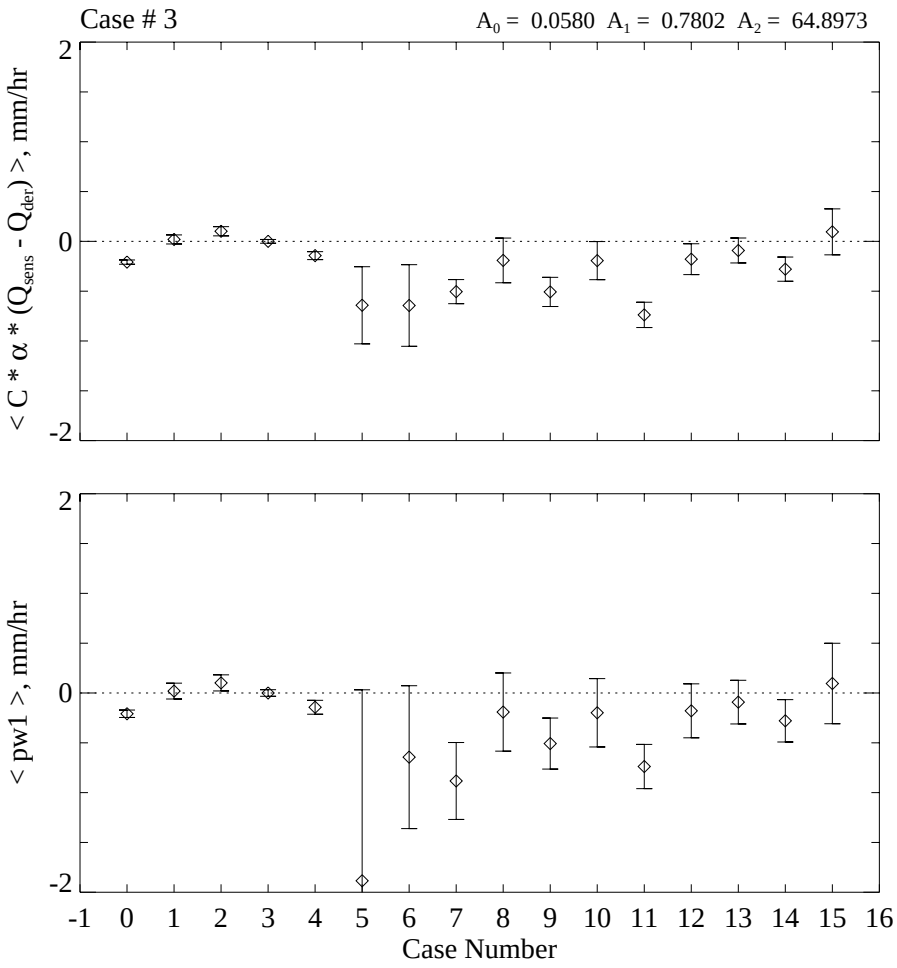

Figure 4 – As in Figure 1, but for the Case #3.

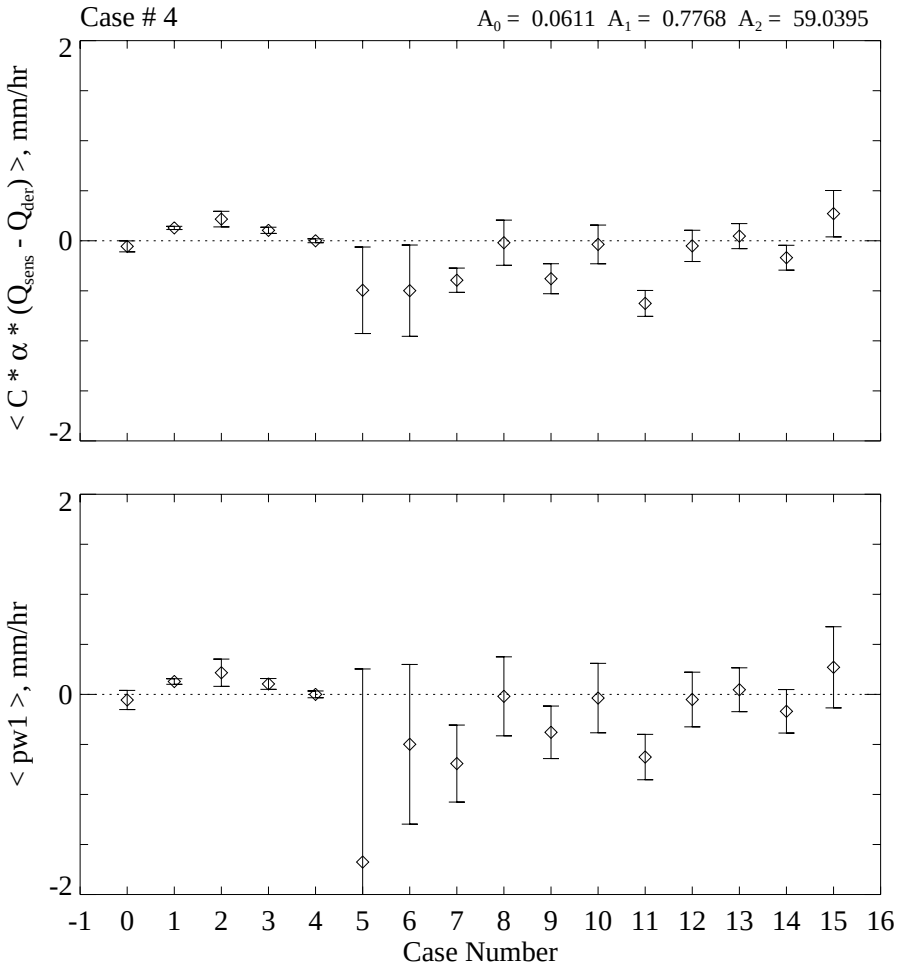

Figure 5 – As in Figure 1, but for the Case #4.

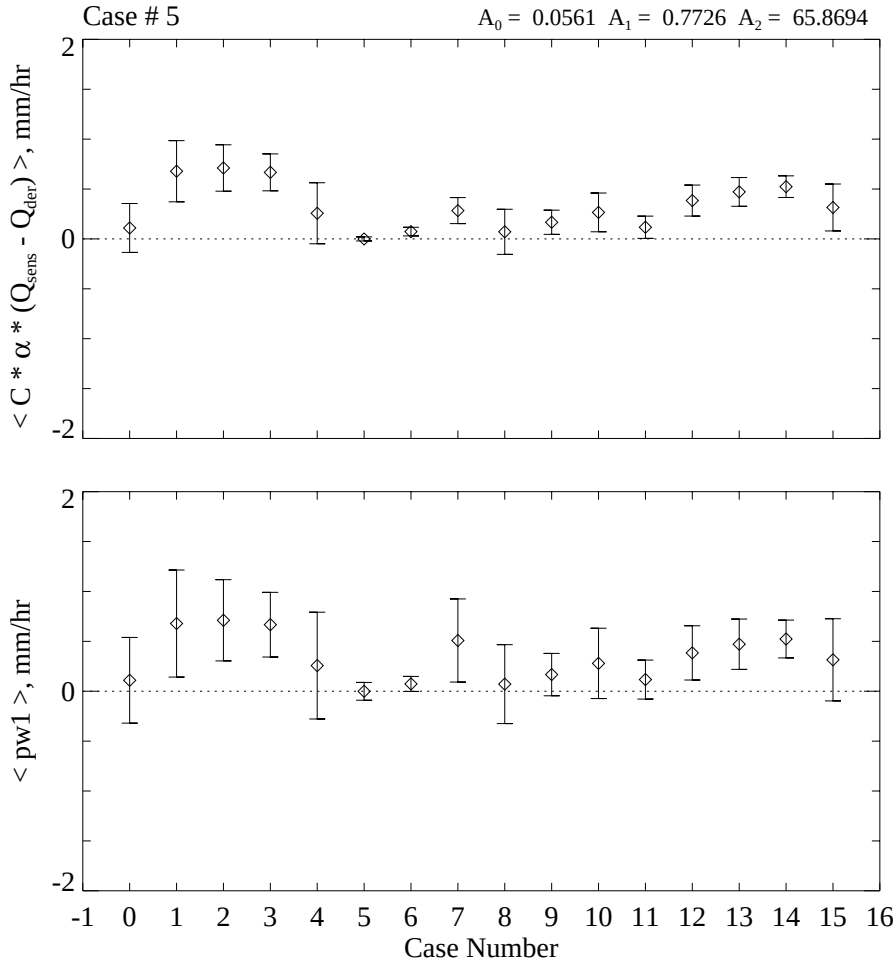

Figure 6 – As in Figure 1, but for the Case #5.

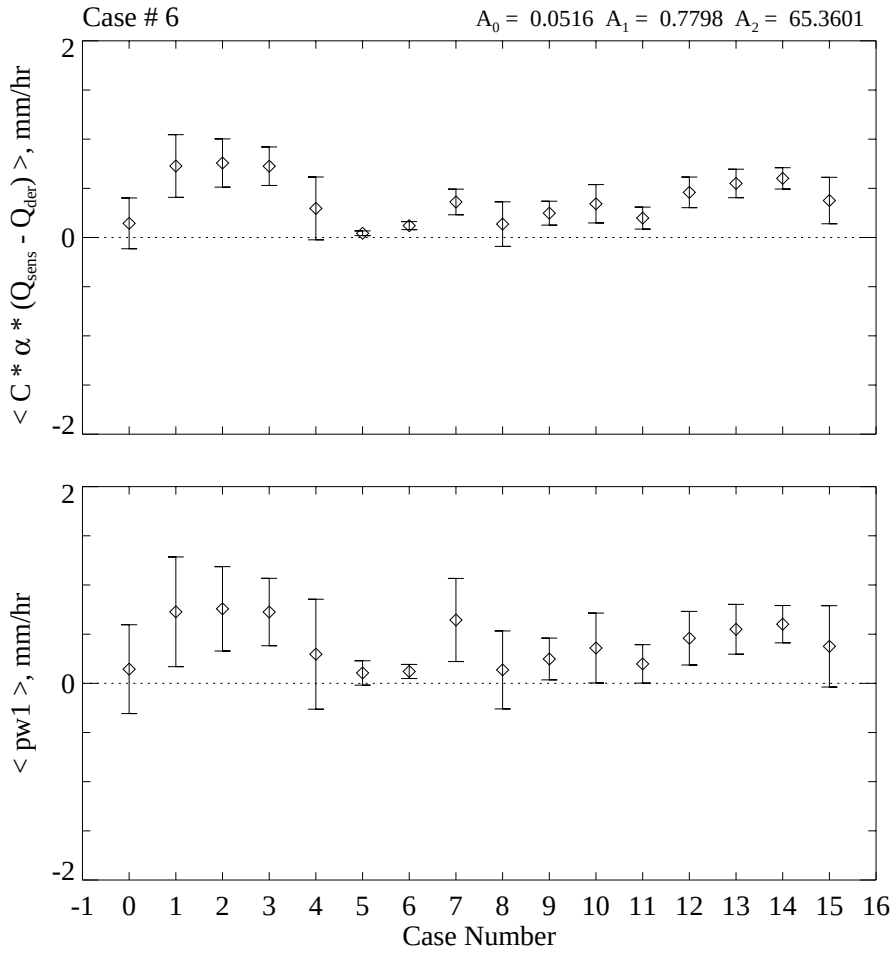

Figure 7 – As in Figure 1, but for the Case #6.

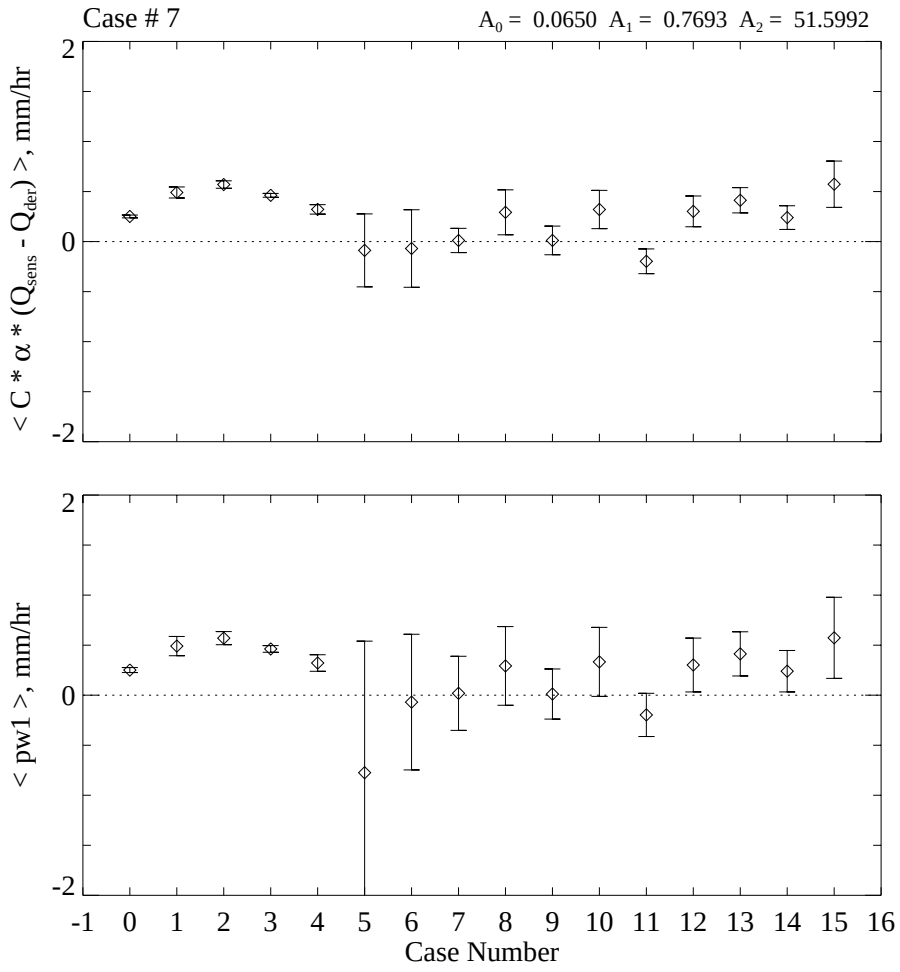

Figure 8 – As in Figure 1, but for the Case #7.

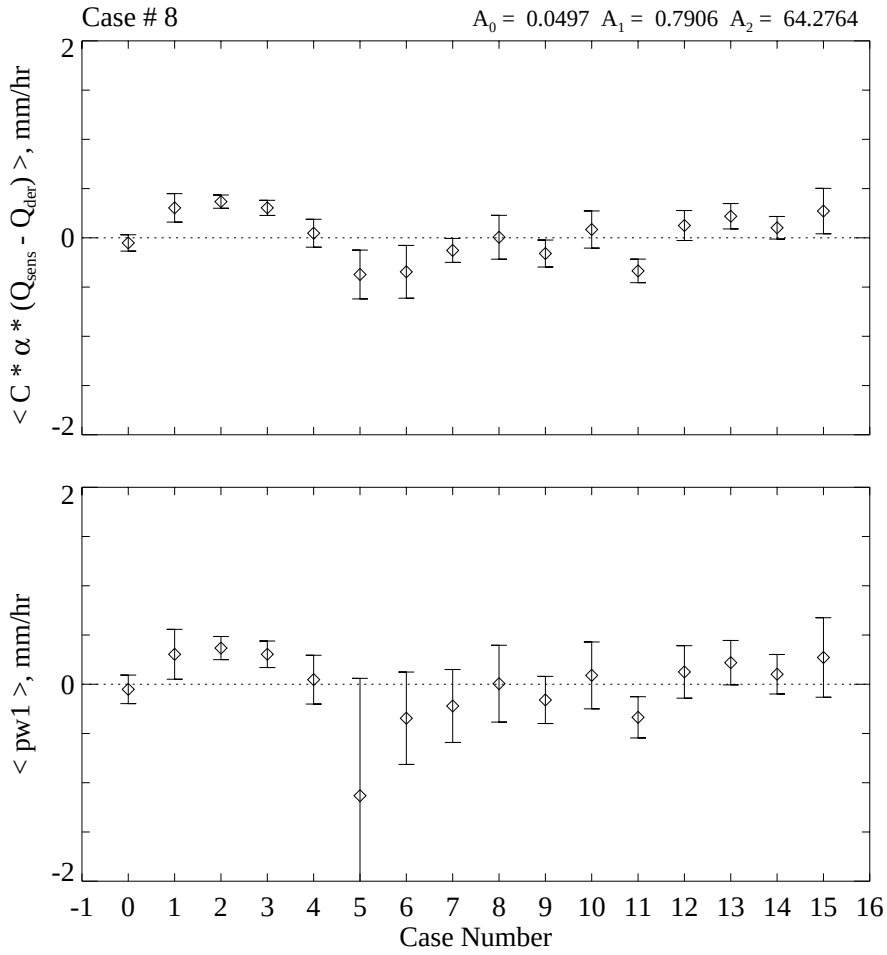

Figure 9 – As in Figure 1, but for the Case #8.

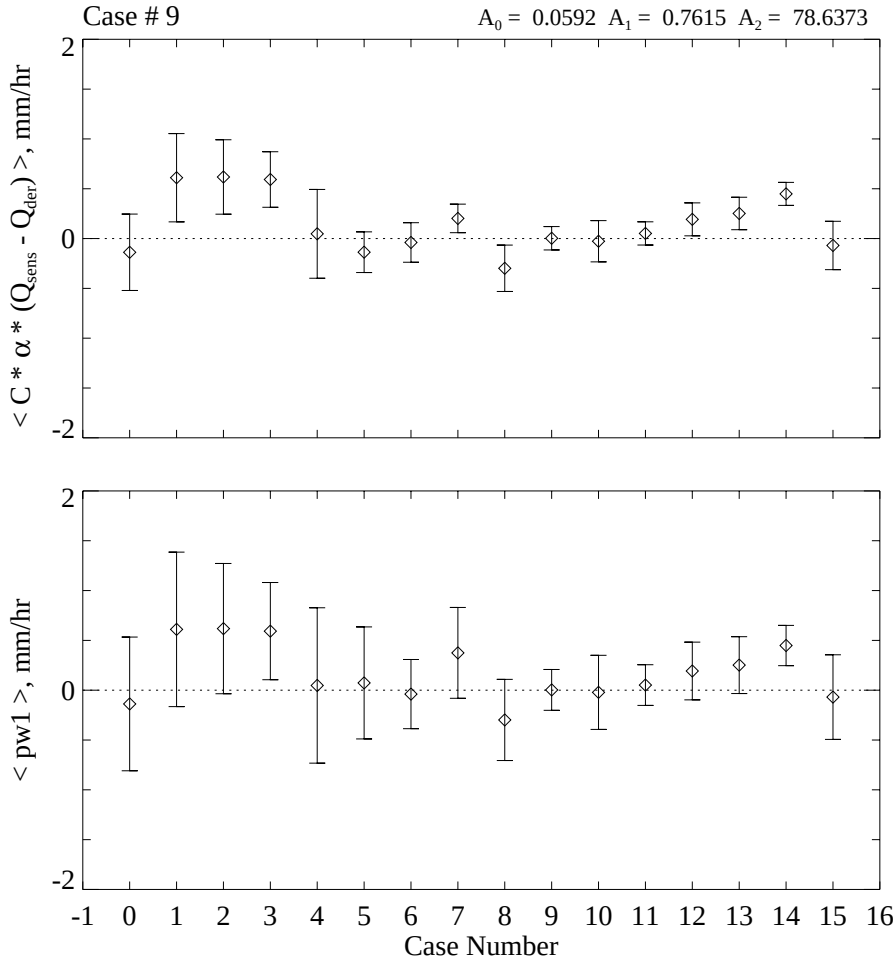

Figure 10 – As in Figure 1, but for the Case #9.

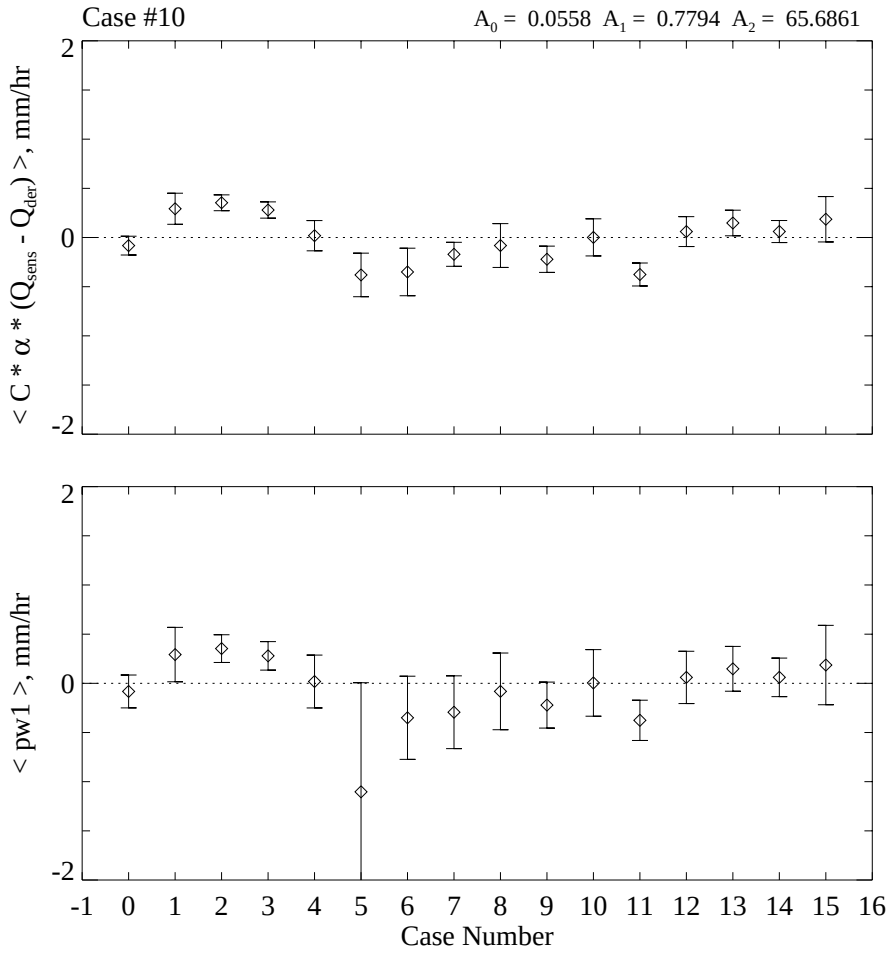

Figure 11 – As in Figure 1, but for the Case #10.

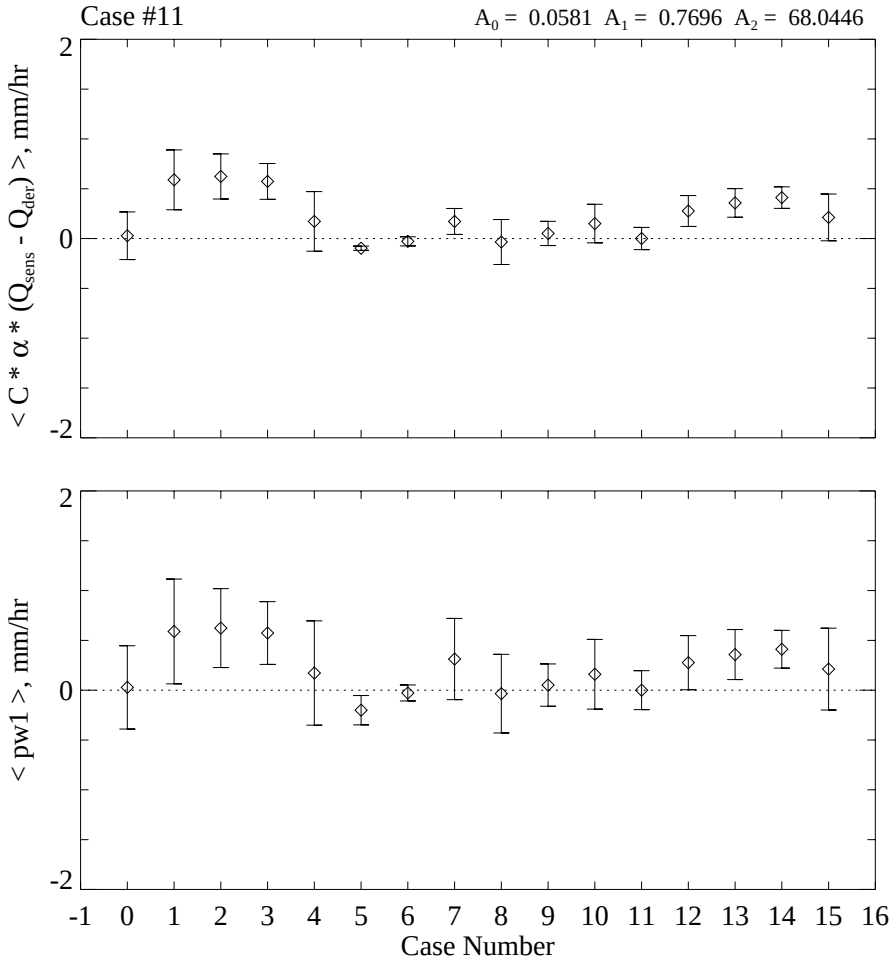

Figure 12 – As in Figure 1, but for the Case #11.

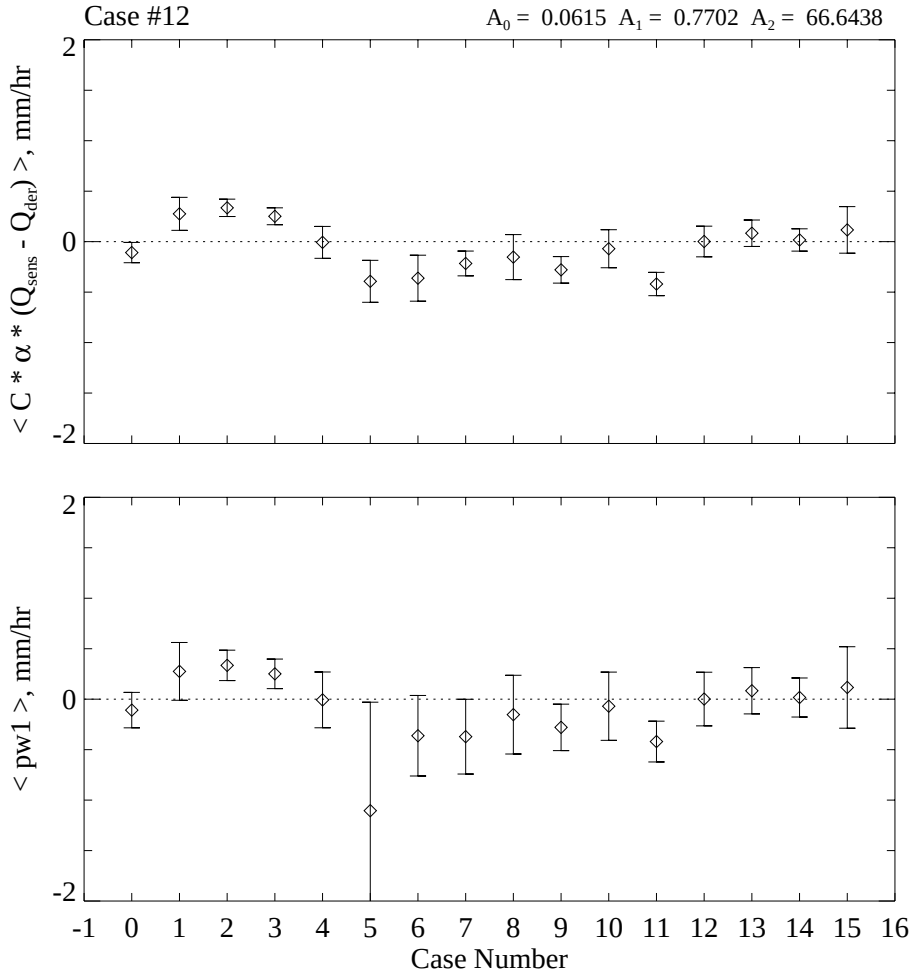

Figure 13 – As in Figure 1, but for the Case #12.

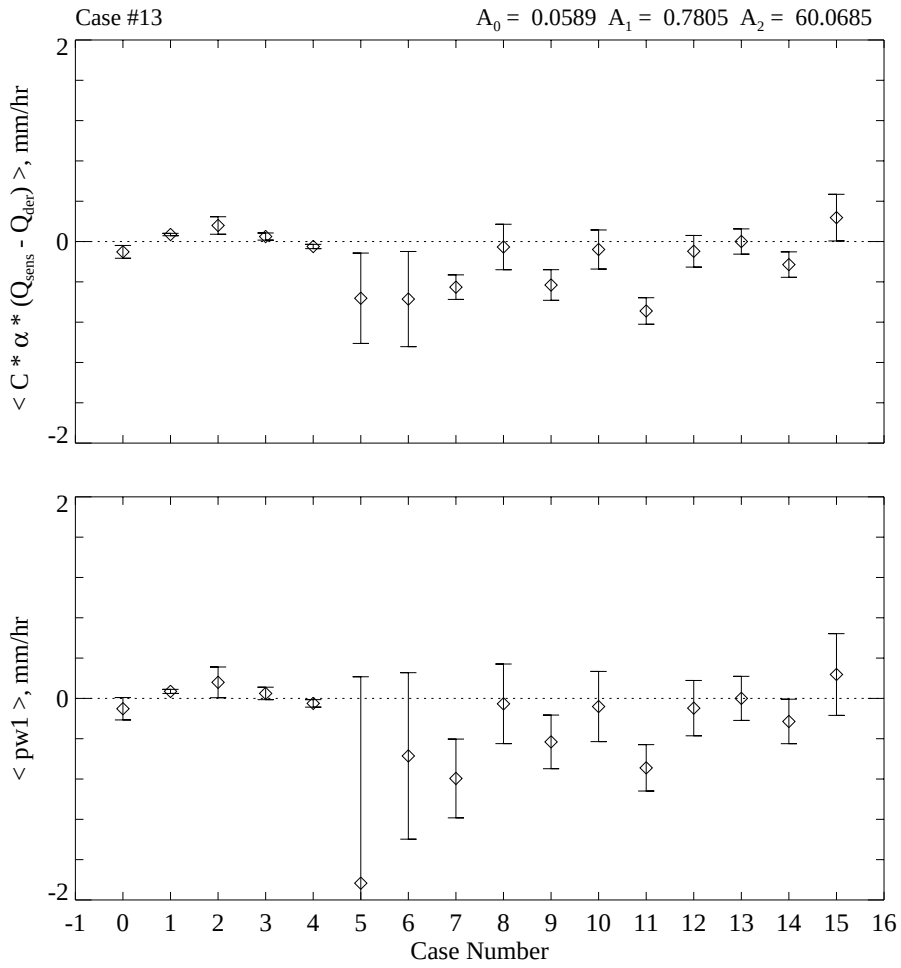

Figure 14 – As in Figure 1, but for the Case #13.

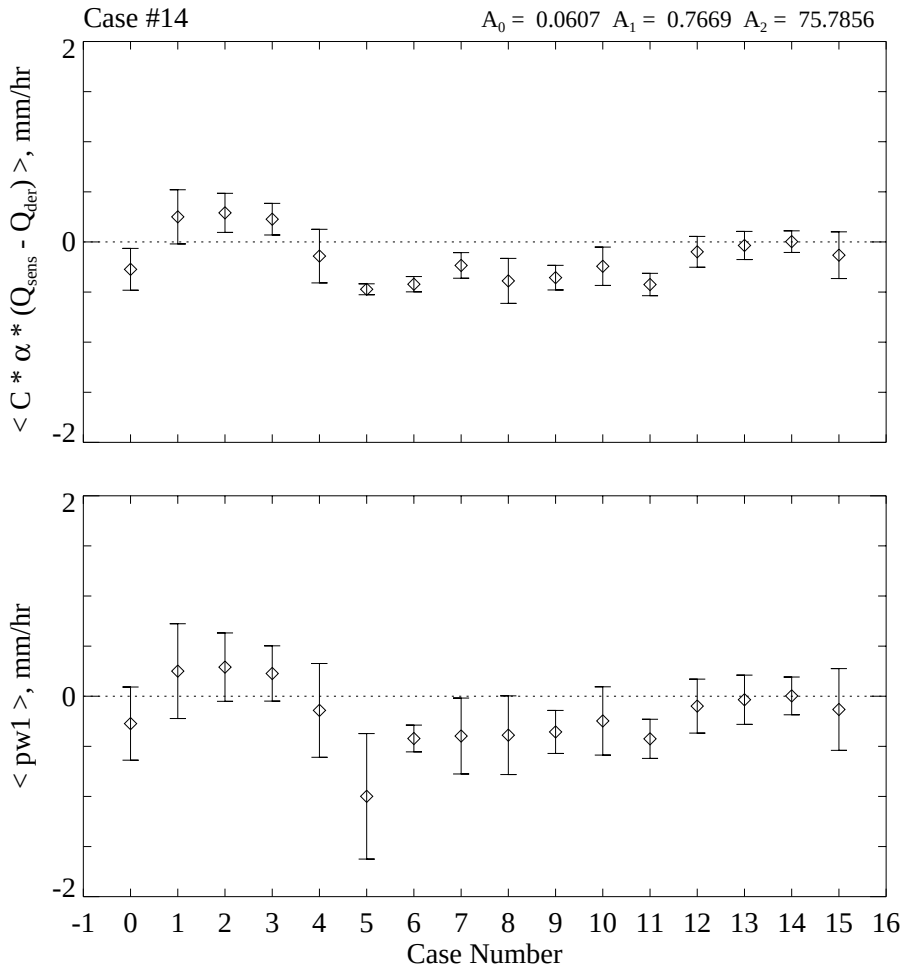

Figure 15 – As in Figure 1, but for the Case #14.

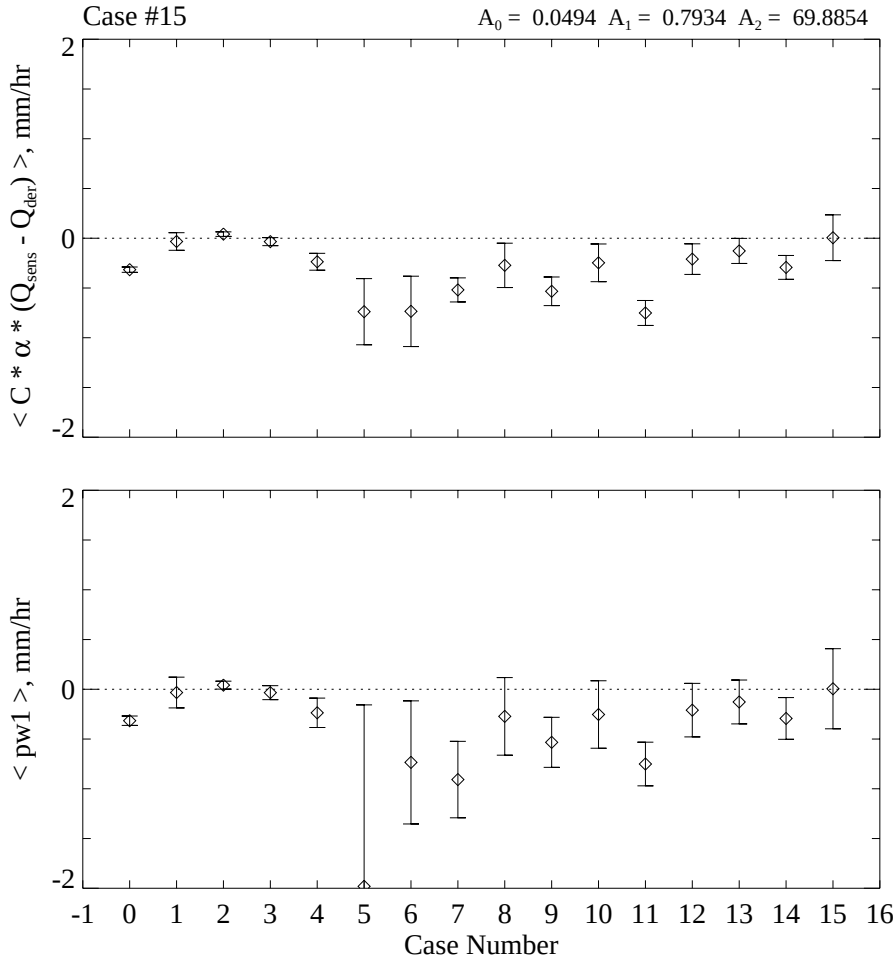

Figure 16 – As in Figure 1, but for the Case #15.

Appendix B: List of Symbols

$f1$	Hotplate proprietary file name
hp	Hotplate standard user's file name
$pf1$	Precipitation rate reported in proprietary file
php	Precipitation rate reported in standard user's file
$pf1\_ave$	300 s running average of $pf1$
$cpf1$	A conditional $pf1$
p_ref	Pump's volumetric output rate (or reference precipitation rate)
$\dot{V}$	Water flow rate
A	Hotplate surface area
L	Diameter of the Hotplate
K	Unit conversion factor
T_I	Inactivity interval
T_A	Activity interval
T_S	Half-input start interval
$pw1$	Precipitation rate derived via Wyoming Hotplate Algorithm
C	Calibration constant
$\dot{Q}_{sens}$	Sensor plate power
$\dot{Q}_{der}$	Heating rate derived from measurements of ambient wind speed and ambient temperature
E	Catch efficiency of the Hotplate
T_∞	Ambient temperature
T_{hp}	Hotplate temperature
T_0	Melting temperature
U	Wind speed
$k(T_\infty)$	Temperature-dependent thermal conductivity of air
υ	Temperature- and pressure dependent viscosity of air
Re	Reynolds number
Nu	Nusselt number
$A_0, A_1 \text{ and } A_2$	Calibration constants obtained from Nu/Re fitting
α	Temperature-dependent unit conversion factor
ρ_w	Density of liquid water
β	Thermodynamic factor
ΔE_1	Energy required to warm up the ice
ΔE_2	Energy required to melt the ice
ΔE_3	Energy required to warm up the liquid

ΔE_4	Energy required to vaporize the liquid
c_i	Specific heat of ice
c_w	Specific heat of liquid water
l_f	Latent heat of fusion
l_v	Latent heat of vaporization

Appendix C: List of Abbreviations

NADP	National Atmospheric Deposition Program
VRG	Vaisala Rain Gauge
SNOTEL	Snow Telemetry
NCAR	National Center for Atmospheric Research
YES	Yankee Environmental System
SWE	Snow Water Equivalent
GLEES	Glacier Lakes Ecosystem Experiments Site
UTC	Universal Coordinated Time
ID	Inner Diameter
LW	Long Wavelength
SW	Short Wavelength